DISSERTATION

EXPLORING NEW APPROACHES TO UNDERSTANDING CHANNEL WIDTH AND EROSION RATES IN BEDROCK RIVERS, PUERTO RICO, USA

Submitted by

Johanna Sophie Eidmann

Department of Geosciences

In partial fulfillment of the requirements

for the Degree of Doctor of Philosophy

Colorado State University

Fort Collins, Colorado

Fall 2022

Doctoral Committee:

Advisor: Sean Gallen

Sara Rathburn
Kenneth Stephen Hughes
Jay Ham

ABSTRACT

EXLORING NEW APPROACHES TO UNDERSTANDING CHANNEL WIDTH AND EROSION RATES IN BEDROCK RIVERS, PUERTO RICO, USA

Earth system dynamics produce constant adjustments to sea level, tectonics, and climate. Bedrock rivers communicate these changes throughout mountains by driving landscape and erosional responses that facilitate topographic change. It follows that an improved understanding of bedrock rivers can help us better model and reconstruct the interplay of changes to base level, uplift, and climate from landscapes. Although bedrock channel width plays a first-order role in river stream power and stream power-based landscape evolution models, because of the physical challenges associated with acquiring these data, channel width is often estimated and introduces uncertainty. In addition, the lack of bedrock channel width data has limited our understanding of what factors control channel width. In this dissertation (Chapter 2), I leverage high-resolution topographic data, Mean Annual Precipitation information, and use the HEC-RAS river modeling software to remotely derive bedrock channel width at desired flow scenarios. The accuracy of modeling results is verified for rivers in Puerto Rico using USGS gauging station field measurements, as well as my own channel width field measurements associated with 1-year recurrence interval discharges. As a next step, (Chapter 3) I implement the bedrock width modeling method derived in Chapter 2 to obtain >4,000 channel width measurements from reaches across Puerto Rico. I then compare these bedrock river width values to various factors (e.g. rock type and rock strength, drainage area, Ecozone, and grain size) that have been identified in the literature to scale with or influence channel width. My analyses indicate that, in Puerto Rico, rock type is a dominant control of bedrock channel width in small (≤6-10 km^2) drainage areas. Contrary to patterns of rock strength and bedrock width documented in the literature (e.g. Montgomery and Gran, 2001), I find that width doesn't appear to correlate with proxies for bedrock channel strength. Strong granodiorites have the widest low-order

channels and the strong volcaniclastics and weak serpentinites have comparably narrow low-order channels. Analysis of limited grain size measurements shows a discernable difference in the coarse grain size distribution between the three rock types, with the volcaniclastic and serpentinite draining rivers having coarser sediment than granodiorite draining streams. These findings suggest that bedrock channel width may be influenced by unmeasured lithological parameters that impact the size of grains delivered to river channels from adjacent hillslopes (i.e. rock fracture density and spacing, as well as weathering). Lastly, (Chapter 4) I spatially analyze in-situ cosmogenic nuclide (^{10}Be in quartz and ^{36}Cl in magnetite) concentrations and find that bedrock erosion rates are higher in the central part of Puerto Rico than toward the east. Analysis of erosion rates compared to other parameters reveals that channel steepness, rather than precipitation or rock type, is positively associated with erosion rates. I further apply these erosion rate data to test the accuracy of four incision models of varying complexity. Model comparisons reveal that drainage area is a better predictor of incision rates in Puerto Rico than a precipitation-weighted drainage area parameter. In addition, whereas an increase in model complexity slightly improves model performance, the model only explains ~35% of the variability in erosion rates. It follows that current incision models are still missing many controlling factors of river incision rates in Puerto Rico.

ACKNOWLEDGEMENTS

Completing this PhD project is a result of a massive team effort. I have worked with and been supported by a community of individuals that have generously and selflessly donated their time and efforts towards helping me complete this project. First, I would like to thank my advisor, Sean Gallen, for helping me throughout this PhD process. Throughout the past four years, Sean has always been a source of guidance that I could rely on, has supported my crazy ideas, helped me brainstorm this project, and knew when to push me out of my comfort zone. I don't think that many advisors can be talked into bushwacking through the dense forests in Puerto Rico during a torrential downpour, subsequently digging ~1 m holes in the ground at a steep incline to install sensors, just to fill the holes back in with soil. Coming into the PhD I told Sean about my interested in becoming a better coder, and Sean has been the most patient and knowledgeable coding teacher throughout my research. I am truly lucky to have had such a positive and supporting advisor.

I further want to thank my committee—Sara Rathburn, Stephen Hughes, and Jay Ham—for generously donating your time towards helping me achieve this degree. I especially want to thank Stephen Hughes for field support, especially during the outbreak of COVID-19 when I could not physically travel to Puerto Rico myself. I thank Jay Ham for supporting my enthusiasm for acquiring Arduino-based field data. Even though these data were never incorporated into this thesis, your support for building low-cost weather stations has provided me (as well as Sean and Stephen) with a skillset that can be applied in exciting ways to future research projects. I also thank Sara for your constant support throughout this process, and for always checking in with me.

In Chapter 4 of this dissertation, I analyze results from in-situ cosmogenic nuclide analysis—a method that I was completely unfamiliar with before my PhD. The learning process required to complete Chapter 4 could not have been completed without the financial support of the Geological Society of America's AGeS 2 program, as well as the UVM cosmogenic laboratory (Lee Corbett and Paul Bierman),

and the Purdue laboratory (Angus Moore and Daryll Granger). I especially appreciate the generosity of Angus Moore, who processed and analyzed the ^{36}Cl samples collected in the field.

A PhD project can be an emotional rollercoaster that has a fair share of ups and downs. I could not have made it throughout this journey without such a supportive group of family and friends. I would like to thank my husband, Chris Johnston, for being a such a great listener, supportive partner, and always putting me first when I need his support. I am further incredibly indebted to Laura Johnston, who has selflessly given up the past two months of her life towards caring for our daughter so that I could finish this project. I would also like to thank my family—Antonia, Josh, Michael, Christine, Katharina, Mark, Fred, Sophie, Champ and Percy—for being a constant source of support throughout this process. I further would like to thank Juli Scamardo, Sarah Hinshaw, Allie Rhea, Paddy Ball, Kristen Cognac, Bri Rick and Miranda Bona, for being my biggest advocates who were there for me to celebrate my accomplishments and support me during the times I struggled.

Last but not least, I would like to thank my dog Charly, who always starts a day with a big grin on his face. I don't think he realizes how much I rely on him for emotional support, and how much I appreciate that he was in the room with me for every word that is written in this thesis. Although it may seem trivial to those who don't know him, Charly has given up many hours of ball playing and has instead patiently sat next to me throughout the analysis and writing, constantly checking in on me throughout the day and never complaining (although the occasional large sigh did come up).

TABLE OF CONTENTS

LIST OF TABLES

LIST OF FIGURES

CHAPTER 1: INTRODUCTION

Visiting Puerto Rico for the first time in 2019, I was surprised by the immense relief found in its mountainous interior. Known for its tropical beaches, I initially expected the topography on the island to be subdued relative to the steep Rocky Mountains that I was most familiar with. Yet as I walked up the trail to the top of Cerro de Punta (the highest point in Puerto Rico), breathing heavily as I sucked in the thick and humid air, I realized that I had underestimated the remarkably steep relief that characterizes its mountains.

Even more humbling is the realization that bedrock rivers are responsible for carving out this steep topography, yet we still have a very limited understanding of how this occurs. Some studies have pointed toward variations in the frequency and magnitude of river discharge for setting the pace of incision (e.g. Baynes et al., 2015; Phillips and Jerolmack, 2016), whereas others have emphasized the significance of the sediment in the rivers that acts as a 'tool' or 'cover' to mediate the rate of incision (e.g. Sklar and Dietrich, 2004, Turowski, 2018). Others have identified even more controlling factors in river incision, including the influence of channel geometry, the climate, rock strength, slope, sediment supply, and the grain size of channel sediments (e.g. Montgomery and Gran, 2001; Lamb and Dietrich, 2009; Pfeiffer et al., 2017; Turowski et al., 2015; Neely and DiBiase, 2020). In this study, I focus on channel width because this is an above-water measurement that can be extracted using remote sensing imagery.

With this dissertation, I provide a pathway toward enhancing our understanding of bedrock rivers and how they carve out the landscape. To achieve this goal, I begin (Chapter 2) by developing a method that enables me to efficiently and remotely extract bedrock channel width measurements of small (areas with channel widths <30 m) catchments from high-resolution Digital Elevation Models. This method is critical for the advancement of understanding bedrock rivers, as current data from bedrock rivers is sparse due to the expensive and logistically challenging nature of collecting field measurements in the steep, remote, and hard-to-access landscapes where bedrock rivers are typically found. Although satellite

imagery has become more available and is often used to remotely extract bedrock channel measurements (Allen et al., 2013; Yamazaki et al., 2019; Lin et al., 2020), the resolution and vegetation coverage in remote imagery often limits this method to large river systems and areas devoid of vegetation. In Chapter 2, I utilize 1 m bare-earth LiDAR to extract a channel network, apply precipitation data to estimate river discharge at a desired location, and implement these data into the HEC-RAS flow modeling software to extract bedrock channel width of small catchments. I chose to perform this analysis and evaluate the method in Puerto Rico, as there exists high-resolution (~1 m) LiDAR across the island, it is located in a tropical landscape that is not impacted by snowfall, it contains a relatively high density of existing USGS gauging stations, and because its mountain rivers are generally sediment supply-limited bedrock rivers. My analysis in Puerto Rico enables me to efficiently glean hundreds of channel width measurements at desired locations along a stream network, across different bedrock types, and at various elevations. I verify this method by comparing modeled results to USGS field measurements at existing gauging stations, as well as field channel measurements. Through developing and validating a streamlined, open-source, and freely available workflow of channel width extraction, I hope this method will be used in future research to improve the quantity of bedrock channel width measurements across the world, which can then be used to improve our understanding of bedrock channels.

In Chapter 3, I apply my new bedrock channel width method to obtain > 4,000 channel width measurements from watersheds across Puerto Rico. Using these measurements, I analyze how river width changes across the landscape. As part of my analysis, I test the hypothesis that bedrock strength is a controlling factor of river width, with stronger bedrock producing narrower channels than weaker bedrock. Analytical results reveal that bedrock only appears to influence channel width at small (< 6-10 km^2) drainage areas, with a rather surprising result that the weaker rock is associated with narrower channels compared to the stronger rock. Interestingly, rock type does not appear to influence channel width at larger drainage areas. Grain size analyses show a lithological difference in bedload sediment size among the different rock types. I find that the narrower channels are associated with the rock types that

produce coarser bedload. This correlation suggests that even though bedrock channel strength does not have a direct influence on river width at larger (>10 km^2) drainage areas, it may still have an indirect impact on channel geometry for lower order channels due to its influence on sediment grain sizes delivered to rivers.

Lastly, Chapter 4 explores spatial differences in denudation rates across Puerto Rico and looks into the ability of simple bedrock incision models to predict these denudation rates. For this analysis, I perform in-situ cosmogenic nuclide analysis (^{10}Be in quartz and ^{36}Cl in magnetite) to derive catchment-average erosion rates from river sands. I combine these results with existing cosmogenic-derived erosion rates to show that the central portion of Puerto Rico is associated with faster erosion rates than the east. I explore potential reasons for these erosional differences, finding that neither rock type nor precipitation appears to control erosion rates, but they may be tied to differences in the topographic steepness of bedrock river channels.

Throughout this chapter, I also explore the importance of understanding bedrock rivers as a means to better predict erosion rates. This effort is important because it provides insight into how tectonic geomorphologists can improve landscape evolution models and better reconstruct past changes in tectonics and climate from topography. A breadth of models of various complexity have been developed to estimate incision rates, but few have been critically evaluated (Whipple, 2022). I thus end my dissertation (Chapter 4) by evaluating how well four existing bedrock incision models of various complexity predict erosion rates. As a culmination of the previous chapters, I calibrate the models by incorporating knowledge of bedrock channel width (derived in Chapter 3, using the method described in Chapter 2) and variations in precipitation. I apply the measured bedrock incision rates (Chapter 4) to the model results to evaluate whether added model complexity enhances prediction of erosion rates.

Throughout the chapters of this dissertation, I explore ways to more efficiently extract bedrock channel width data, evaluate the potential factors that may control bedrock channel width, and evaluate how well models of different complexity and input parameters predict bedrock incision rates. It is my

hope that these developed methods and analyses spark ideas and discussion that will help to improve an understanding of bedrock rivers and enhance the performance of landscape evolution models.

CHAPTER 2: NEW REMOTE METHOD TO SYSTEMATICALLY EXTRACT BEDROCK CHANNEL WIDTH OF SMALL CATCHMENTS ACROSS LARGE SPATIAL SCALES

2.1 Introduction

River channel geometry measurements (e.g., slope and width) are essential in scientific and societal applications. Among other applications, channel geometry measurements are used in hydrologic models (Neal et al., 2015; Yanites, 2018), stream restoration studies (Kondolf et al., 2002; Nelson et al., 2015), and sediment transport models of alluvial rivers (Prosser et al., 2001; Merritt et al., 2003), used to explain bedrock channel sinuosity (Turowski, 2018), and implemented in bedrock-channel incision models to provide insight into the topographic, morphologic, tectonic and climatic history of an area (Finnegan et al., 2005; Allen et al., 2013; Fisher et al., 2012, 2013). Performing bedrock incision rate calculations, especially at a large spatial scale, requires knowledge of how channel geometry changes across the landscape. Whereas channel width is an important metric of channel geometry, many models simplify and account for this variable through a channel roughness parameter, and rather focus on estimating or measuring channel width and slope Analyses frequently assume spatial changes in channel width via scaling relationships between channel width and other more easily or typically measured proxies, such as drainage area or discharge (Knighton, 1998; Whipple and Tucker, 1999; Willett, 1999; DeLong et al., 2007). Although empirical data support such scaling relationships, most measurements are from alluvial river systems, and the data used to derive the scaling relationships data show significant scatter (Whipple et al., 2022).

Because of these limitations, researchers have recently taken advantage of the increasing accessibility to satellite imagery and remote sensing data to derive channel width measurements of large river (typically >30 m channel width) systems and some smaller river systems with minimal vegetation cover across broad spatial scales (e.g. Fisher et al., 2012, 2013; Allen et al., 2013; Allen and Pavelsky, 2018; Yamazaki et al., 2019; Lin et al., 2020). Although valuable, these data sets extract measurements from

one snapshot in time (not necessarily during comparable flow periods), typically use imagery that is limited in resolution (≥30 m), and are restricted to locations where vegetation cover does not impede the view of the river. Therefore, for all other scenarios—small river systems (e.g. areas with channel widths <30 m) and climates that allow for moderate to heavy vegetation growth—researchers largely rely on width measurements from field campaigns that are time-consuming, labor-intensive, often spatially limited in extent, and logistically challenging due to a lack of river access. As a result, field width measurements of bedrock channels, often found in steep, remote, and hard-to-access landscapes, are sparse, forcing researchers to generally embrace the use of scaling relationships derived from alluvial river systems to estimate channel width of bedrock rivers (Whipple et al., 2022). The use of such scaling relationships, however, might be inappropriate for bedrock channels. Bedrock channel width is a function of a multitude of factors beyond discharge (or, by proxy, drainage area), including rock uplift rate, bedrock lithology and rock strength, sediment supply, hydraulic roughness, vegetation, slope, and climate (Duvall et al., 2004; Finnegan et al., 2005, 2007; Whittaker et al., 2007; Walsh et al., 2012; Spotila et al., 2015). Such studies highlight a current incomplete understanding in the literature of controls of bedrock channel width and the need to develop new remote sensing methods capable of measuring bedrock channel width across large spatial scales.

Existing studies highlight the need for more field data on this parameter in bedrock channels, which would enable a better understanding of the factors that control channel width (Finnegan et al., 2005; Whipple et al., 2022). However, even when field channel width measurements exist, these data can be misleading for a number of reasons. As a dynamic stream variable, channel width changes according to the shape of the channel cross-section and the flow magnitude (i.e. discharge). As a result, field measurements of channel width must be acquired or referenced to the same flow magnitude. These flow conditions, however, can change in both space and time across a field campaign, limiting the ability to accurately correlate between the various measurements. Most bedrock channel studies do not know the reference flow conditions at the time of their field campaigns, and therefore turn to measuring “bankfull”

channel width—defined by Wohl and Merritt (2005) as the wetted channel width during "discharge that recurs on average every 1-2 years". Because field data are typically not collected during such discharge conditions or streams are not gauged, and this reference discharge is unknown, the bedrock channel width is often measured using assumed "bankfull" indicators such as changes in bank geometry, a lack of vegetation, scour marks, or stains observed on clasts or bedrock (Wohl and Merritt, 2005; Lague, 2014; Turowski, 2018; Zondervan et al., 2020). However, where these "bankfull" measurements in bedrock channels can often be variable based on the subjective opinion of a particular observer or field personnel and differences in climate and speed of vegetation regrowth, likely leading to inconsistent results across different landscapes. Due to the ambiguities associated with collecting bedrock channel width field measurements, it becomes difficult to fully standardize, compare, and understand field measurements of channel width based on data derived from numerous field campaigns, researchers, and climates. These underlying limitations to the field measurements highlight the need to derive new methods for determining comparable values of bedrock channel width for moderate to small river systems across large spatial scales.

In this research, I overcome these limitations by developing and presenting a new method to determine bedrock channel width that leverages the recent growth and availability of high-resolution bare-earth digital elevation products (e.g. LiDAR) to fill this data gap. I introduce a method for systematic (objective and under similar flow conditions), high-resolution bedrock channel width extraction. Recently, Bernard et al. (2022) implemented a similar method, employing a 2D morpho-hydrodynamic model to systematically extract channel width measurements from an approximately 17 km^2 drainage basin using LiDAR. Although demonstrating promising results, the model output is effective flow width, which is not directly comparable to the reported wetted width of other studies, and the authors noted that results were not evaluated for accuracy nor compared to field measurements.

In my methodology, I employ TopoToolbox in Matlab in concert with a freely available and widely-used hydrology modeling software (HEC-RAS) and a high-resolution Digital Elevation Model (DEM) to

perform this analysis in a way that does not require extensive coding experience from the end-user. To facilitate the application of this method, I present a general workflow of the analysis and a more in-depth user guide in the appendix (see *User Manual*). I validate this method by comparing model results with USGS gauging data and field measurements. Next, I automate this process in a case study of a watershed in Puerto Rico (Figure 2.1b and c). I chose to perform analysis in Puerto Rico due to the availability of high-resolution (~1 m) LiDAR across the island, because it is located in a tropical landscape that is not impacted by snowfall, the relatively high density of existing USGS gauging stations, and because its mountain rivers are generally sediment supply-limited bedrock rivers. My analysis in Puerto Rico enables me to efficiently glean hundreds of channel width measurements at desired locations along a stream network, across different bedrock types, and at various elevations. By validating this method and presenting its effective application, I hope to open avenues for researchers to extract bedrock channel width data more safely and efficiently from the watershed-to-landscape scale, and provide a process that can significantly increase the quantity of bedrock channel width measurements in small (<30 m wide) bedrock rivers. Although I acknowledge that deriving channel geometry from high-resolution DEMs has its limitations, this method provides a path forward to improving data richness and our understanding of bedrock channel width by taking advantage of the ever-increasing accessibility of global LiDAR data.

2.2 Background

2.2.1 Study Area

The Caribbean Island of Puerto Rico is approximately located at 18°N and 66°W (~1,700 km southeast of Miami, Florida) and spans about 180 km from east to west and 60 km from north to south (Figure 2.1a-c). Its subtropical marine climate is relatively consistent year-round, with temperatures typically ranging between 70°F and 90°F (The Southeast Regional Climate Center, 2019). Northeast trade winds that cross the island generally determine precipitation and climate and are modified by tropical depressions, storms, and hurricanes (Ehlmann, 1968; Calvesbert, 1970). Precipitation patterns are orographically controlled, with the high-elevation northern portion of the island typically receiving the

most precipitation (mean annual precipitation of over 4,000 mm), whereas the flatter southwestern portion of the island tends to be the driest (with an average annual precipitation of approximately 732 mm) (Figure 2.1b; NOAA, 2011).

Topography varies dramatically across the island and can be classified into three physiographic regions: the mountainous interior, the coastal lowlands, and the karst area (U.S. Geological Survey, 1998). The mountainous interior is comprised of the Cordillera Central, which is characterized by highly deformed volcanic rocks and less deformed or undeformed plutonic rocks (mainly volcaniclastic and granodiorite, respectively) formed in the Cretaceous to Paleocene and early Eocene (U.S. Geological Survey, 1960) (Figure 2.1c). Towards the north and south of the island, the older volcanic rocks are overlain by younger (Tertiary in age), gently-dipping carbonates, and sedimentary rocks (Schellekens, 1998). Reef Carbonates, deposited in the Oligocene to early Pliocene, which are generally located in the northern portion of the island, form the rugged and distinct karst topography (Moussa et al., 1987). In contrast, the coastal lowlands in the southern portion of the island are composed of Miocene to Quaternary sedimentary rocks that form a gentle topography (Volckmann, 1984).

As noted above, I chose to test my new method in Puerto Rico for a variety of reasons. First, the island contains a high density of USGS monitoring stations (Figure 2.1b and c), with 73 gauging stations that monitor a cumulative drainage area of >7,000 km^2 (equivalent to approximately 80% of the island area). Many of these stations further offer temporally continuous data, with some stations providing >60 years records (Table A1). Second, Puerto Rico's mild, subtropical climate offers an area devoid of snow. This was an important consideration, as snow can alter how precipitation is temporally and spatially received and processed by the landscape (e.g. water storage throughout the winter, and spring snowmelt discharges that are independent of the mean annual precipitation). Although Puerto Rico's climate is characterized by a 'dry' and 'wet' season, the relatively consistent temperature across the year ensures minimal impact of a more extreme seasonality seen across different areas of the world. Finally, the crystalline rock types (the focus of this study) that comprise most of the mountainous topography on the

island are defined by predominantly bedrock channels where sediment transport capacity exceeds sediment supply.

2.2.2 TopoToolbox in Matlab

We used TopoToolbox v2—an open-source MATLAB-based software—to extract field-specific information and manipulate data inputs in preparation for flow simulations and river width measurements through HEC-RAS modeling. More specifically, TopoToolbox v2 (Schwanghart and Scherler, 2014), enables me to easily combine elevation data, geologic maps, and precipitation data into one set of layers, which in turn lets me systematically choose the specified modeling locations based on desired characteristics. Key TopoToolbox components used in Matlab included deriving the stream network from a LiDAR DEM by filling sinks in the DEM, calculating the drainage network at different locations, and calculating the steepness index of channel reaches. Through spatially extracting this information using TopoToolbox, my analysis is more flexible, as I can combine and overlay this data with existing USGS gauging discharge data, to better calculate parameters, such as discharge, that I then implemented into the HEC-RAS model. Lastly, TopoToolbox and Matlab were instrumental in automating our method, providing a base for me to develop a code that automatically created river network and cross-section shapefiles that could then be directly uploaded into HEC-RAS with limited user interference.

2.2.3 HEC-RAS

To efficiently route flows of desired discharges across channel networks derived from a LiDAR DEM of Puerto Rico, I turned towards the freely available HEC-RAS River Analysis System developed by the Hydrologic Engineering Center for the U.S. Army Corps of Engineers, and widely used across academic and professional river modeling fields. Due to minor bugs found in the more current version of HEC-RAS, I used version 5.0.7 (released in March 2019) for this analysis. Within HEC-RAS, I use a 1D Steady Flow hydraulic model rather than more computationally-expensive 2D models because (1) the streams I analyzed had a dominant flow direction with a known general flow path, (2) the streams are mainly characterized as steep bedrock channels with minimal overbank areas, and (3) my analysis lacked

detailed channel bathymetry information since I was using DEMs acquired through near-infrared LiDAR (1064 nm), which cannot penetrate through water. This reasoning and choice of employing a 1D hydraulic model is supported by the HEC-RAS 2D Modeling User Manual (Brunner, 2021). In addition, it is important to note that a 1D hydraulic model is substantially more computationally efficient and typically has fewer unconstrained parameters than the more complicated 2D models, allowing me to perform modeling simulations more efficiently across many locations in a larger landscape. Furthermore, as shown below, the simpler 1D model performs well in predicting observed data, suggesting that the additional computational expense of running a 2D model might not add much value.

The 1D Steady Flow model in HEC-RAS generally uses the Energy equation to compute the energy grade line and water surface elevations across desired locations of interest under a given discharge scenario. Data requirements to run the model include geometric data and flow data. Geometric data are acquired by HEC-RAS through the input of a DEM (e.g. terrain model), river channel shapefiles (providing the river path, flow direction, reach length, river system schematic), and cross-sectional shapefiles (identifying the location and extent of desired cross-sections, drawn perpendicular to the flow lines).

Flow data are entered into the program to establish the flow regime and boundary conditions. Because I am mainly modeling subcritical flow conditions, I define a water surface at the downstream end of the river network, which allows the hydraulic model to proceed with calculations in the upstream direction. When the downstream water surface is unknown—which is the case for my calculations—it is recommended to use an estimated water surface elevation above the channel bed. To avoid the impact of the downstream water surface boundary condition, it is recommended to extend the river network so that the study reach is well upstream (Figure 2.2; USACE, 2016). This allows model results to converge to a consistent answer once the computations reach the upstream study area (USACE, 2016). An additional model flow input includes the Manning's n channel roughness coefficient, for which I used a n=0.05, representative of 'normal' values for mountain streams devoid of in-channel vegetation, characterized by

steep banks, and with channel bottoms comprised of mainly cobbles and large boulders (USACE, 2016). Based on field observations, I found this roughness value to best characterize bedrock channels in Puerto Rico, but also want to highlight the ability to easily modify this value based on variable types of river channels in different environments or locations (see *User Manual*). As a final flow input, I entered a desired water discharge for each river reach, which the 1D Steady flow model assumes remains constant across the length of the reach.

A breadth of output parameters can be extracted from each model run, including channel width, average flow velocity, hydraulic radius, mean flow depth, shear stress, and total stream power. For this analysis, I mainly focused on the wetted channel width across a specific location of the reach, and thus primarily extracted this result (e.g. reach-averaged width) across all cross sections and river reaches.

2.3 Proof of Concept and Application in Puerto Rico

In this paper, I explore a new method of obtaining channel width measurements remotely across a range of drainage areas. To demonstrate the method's utility and accuracy, I first validate the method results by comparing these data with USGS channel measurements acquired at existing USGS gauging stations across different discharge scenarios. To bolster this analysis, I then conduct an island-wide comparison (providing for a large range in drainage areas) of channel width measurements from USGS gauging stations with modeled results under mean annual discharge scenarios. A third way that I validate my method is by comparing model results to my field measurements. Because these field measurements are not acquired near gauging locations, I explore the utility of a simple approach to estimate discharge of a given magnitude based on correlations with upstream mean annual precipitation. Having validated the method, I lastly examine the efficiency of the model by conducting analysis at a catchment scale, and perform first-order exploratory analysis of the results to demonstrate how these channel width measurements fit into the context of existing research of bedrock channels.

2.3.1 Method Validation Using USGS Gauging Stations

To evaluate the accuracy and utility of the derived method, I compared modeled width measurements to USGS field measurements collected at 49 of the 73 gauging stations across Puerto Rico (Figure 2.1b and c). I eliminated stations draining carbonate bedrock to avoid areas potentially impacted by karst hydrology, and stations directly downstream of dams where flow is modulated and the mean annual discharge (MAQ) does not reflect natural changes in precipitation. I chose to use the USGS field measurements of channel width, as they are field data that have undergone a quality control process and are deemed of sufficient quality to be incorporated into the rating curve of the respective gauging station. In addition, these measurements included relevant data—namely channel width measurements—across different discharges.

First, I used the mean daily discharge values across the time of record for each station to determine the MAQ at each gauged location that met my criteria. Next, I analyzed the USGS field width measurements, which provide insight into changes to the channel width at the same location across different discharge scenarios. Performing such verification across a range of discharge scenarios is an important aspect of validating the utility of the model, as width intrinsically varies with discharge; as discharge increases, so too does channel width. This relationship is expressed in the following power-law equation by Leopold and Maddock (1953).

$$w = aQ^b \qquad \text{(Eq. 2.1).}$$

where w denotes channel width, Q is water discharge, and a and b are empirical constants. As a result, discharge has a first-order impact on the resulting modeled channel width.

Because the USGS field measurements were collected both close to the gauge location and from distances of up to >215m from the gauging station, and my field observations at numerous gauging stations and rivers in Puerto Rico indicate that channel width often significantly varies across a ~215 m reach length, I decided to use the median modeled channel width values to compare the accuracy of width measurements between the USGS field measurements and the modeled results. Comparing the field measurements across different discharges and across various gauging station locations reveal that the

model did a reasonable job at predicting river width at different discharges (Figure 2.3a), with results generally mimicking Leopold and Maddock (1953)'s power-law behavior and often falling within one standard deviation of the binned field measurements at a comparable discharge (Figure 2.3b).

To extract representative USGS field data at the MAQ across different stations, I calculated width measurements within ±0.5 m^3/s of the calculated MAQ of each station (Figure 2.3c). From these data sets, I evaluated how well the median width field measurements (bounded by the maximum and minimum values) compared to the HEC-RAS model results (Figure 2.4a). Of the 49 stations that were analyzed, the median modeled channel width results fell within the USGS measurement range at 47 (or 96%) locations. At the two stations where the modeled result overestimated channel width, the modeled measurements were within 1 m of existing USGS channel width field measurements. The comparison of the USGS field measurements with the modeled results (Figure 2.4a and b) indicate that my method works well across different locations, discharges, and drainage areas that span over 3 orders of magnitude (~1 km^2 to ~500 km^2).

2.3.2 Model Validation with Field Measurements

To further validate my method, I sought to compare my model results to field measurements that I collected across the island, largely at ungauged locations. During two field campaigns in March 2020 and January 2022, I obtained 165 channel width measurements at 27 field locations, with an average of 6 measurements at each location (Figure 2.1a and b). In the field, I used a laser rangefinder to measure the approximate bankfull channel width, which I assumed to be marked by a lack of vegetation along the channel banks. Considering the fast vegetation regrowth in Puerto Rico, I presume that my channel width field measurements reflect vegetative stripping and erosion that occurs during a discharge with a 1 to 2-year reoccurrence interval (RI), and less frequently than the MAQ.

Because discharge has a first-order impact on channel width, it is important to consider channel width across a similar reference flow. Deriving this reference flow, however, can be challenging at ungauged locations. Previous studies have used satellite-based measurements of mean annual

precipitation (MAP) as a proxy for calculating discharge at ungauged locations (Rossi et al., 2016; Desormeaux et al., 2022). Comparing MAP—calculated by averaging the mean annual precipitation obtained from the PRISM data set (PRISM Climate Group, 2022) across the respective location's drainage basin—to the MAQ at the known USGS gauging locations reveals that MAP is a good proxy (r^2=0.82) for predicting MAQ in Puerto Rico when assuming a power-law relationship (Figure 2.5, Figure A2). However, this strong positive relationship between the two parameters remains predictive but weakens when MAP is compared to the 1-year and 2-year return interval discharge magnitudes at these locations (Figure A1). As completed by Rossi et al. (2016), precipitation probability can be used with discharge frequency to improve this relationship, yet even in these scenarios, the strength of the relationship appears to degrade with increasing RI (Rossi et al. (2016) found an r^2=0.48 for 2-year RI events). With this in mind, I may expect my 1 to 2-year RI discharge estimates derived from MAP to be underestimates of the true 1 to 2-year RI discharges at the field locations and the modeled channel widths using these estimated discharge data to produce lower channel width values.

For comparison between modeled channel width and my field measurements, I chose to use the average channel width at the point of measurement because (1) field width measurements were collected close to one another (within an approximately 50 m reach, thus limiting large variations of channel width) and (2) measurements were largely normally distributed (Figure A3).

A comparison between modeled (at MAQ, 1-year, and 2-year discharge scenarios) width and field width measurements shows that MAQ-based channel width modeling results are consistently lower than field measurements (Figure 2.6a and d). This supports my presumption that the field measurements reflect 1 to 2-year RI flow conditions rather than MAQ conditions. Although the modeled width measurements only fall within the range of field measurements at 18 of the 27 locations, there appears to be reasonable alignment between the modeled and measured width values when measurement error is considered (Figures 2.6b, c, e, and f).

Comparing modeled channel width with bankfull field measurements highlights the utility of this method in multiple ways. First, it emphasizes the subjectivity of bankfull field measurements, as these measurements can be delineated differently based on the subjective opinions of what bankfull looks like to various field personnel, disparities in the rates of vegetation regrowth, among others. In addition, the recurrence interval associated with these width measurements is largely unknown but is assumed to fall within a 1 to 2-year time frame. The discharge associated with such recurrence intervals is more difficult to predict at ungauged locations. However, analysis of the relationship between precipitation and discharge reveals that MAP can be used as a good predictor for MAQ (r^2=0.82), but it does not predict the discharge of 1 and 2-year RI as well (r^2=0.44 and 0.3, respectively). These results highlight the utility of using MAQ as a better predictor of the spatial pattern of discharge at ungauged stations. However, the comparison with my field measurements shows that the 1 and 2 year RI provides a better match to these data and suggests that my field measurements are consistent with typical bankfull definitions (Figures 2.6b, c, e, and f).

2.3.3 Automating the Method to Enhance the Quantity and Spatial Distribution of Bedrock Width Channel Measurements

In the previous sections, I validated the accuracy of my method's results by comparing modeled channel width measurements with both USGS gauging station data and my field measurements. These results show that my method, within 2 standard deviations of uncertainty, reproduces field-based width measurements at a given reference flow condition for a reasonable range of discharge magnitudes (Figure 2.3a and b, Figure 2.4, and Figure 2.6). As a next step, I aim to use this method to gather channel width measurements remotely and efficiently with the intent of increasing the number of small (≤30 m width) bedrock channel width measurements obtained across the world. The general steps of modeling channel width are outlined in Figure 2.7. A more detailed and in-depth workflow designed to streamline the understanding of the modeling process and promote reproducibility of results is described in a *User Manual* with accompanying code found in supplemental files (Appendix A). The utility of the method to

produce unique analytical results of channel width is briefly explored below through a case study of the Caonillas watershed in central Puerto Rico (Figure 2.1b and c).

Using my workflow (Figure 2.7), I extracted channel width measurements at 431 reaches across the Caonillas watershed (an approximately 125 km^2 area; Figure 2.1a and b). In general, I systematically sample individual stream reaches that are 200 m in length and space out each analyzed reach in 500 m streamwise distance intervals. I eliminated reaches that were close to the Caonillas Reservoir or generated sampling locations that were less than 500 m in distance from one another. Four lithological units are encountered within the Caonillas watershed, including granodiorite (53%), volcaniclastics (36%), contact metamorphic rocks (2%), and sedimentary rocks/alluvial deposits (7%) (Figure 2.8a). The mean annual precipitation in the watershed appears to be closely linked to topography, with the highest precipitation values occurring in the areas of highest elevation (Figure 2.8b and c).

For this analysis, I use MAQ as my reference discharge based on the relationship given in Figure 2.5 and a map of mean annual precipitation, but I also ran similar simulations for the 1 and 2 year RI discharge magnitudes. It is important to note that my modeled width resolution is sensitive to the DEM resolution (~1 m^2). Therefore, I consider width measurements that span twice the DEM resolution (~2 m) as reliable. For my MAQ reference flow condition, this width resolution corresponds to a drainage area of > ~1 km^2, so I only analyzed river reaches ≥1 km^2 after running the automated analysis. However, I note that higher magnitude reference discharges yield resolvable width results at lower upstream drainage areas. After filtering my results based on all of these considerations, 116 stream reaches remained for analysis in the watershed.

Preliminary data analysis reveals interesting channel width trends and other metrics across the watershed. Analyzed channel measurements cover a large range of drainage areas, spanning two orders of magnitude (1 km^2 to 104 km^2). Results show a strong positive relationship between drainage area and channel width, with an increase in drainage area associated with a wider channel (Figure 2.9)—a trend that has consistently been recognized in the literature (e.g. Wohl et al., 2004; Duvall et al., 2004; DiBiase

and Whipple, 2011; Whipple et al., 2022). Interestingly, the exponent of a power law regression through the data, ~0.47, is generally similar for the MAQ, 1 year, and 2 year recurrence interval reference discharges (Figure 2.9).

Of the analyzed reaches, 46 (40%), 22 (19%), 48 (41%) and 0 (0%) locations were underlain by granodiorite, volcaniclastics, sedimentary rocks/alluvial deposits, and metamorphic rocks, respectively. In general, reaches underlain by granodiorite were located at lower elevations (median elevation of 750 m), whereas reaches underlain by volcaniclastics were located at higher elevations (median elevation of 882 m and maximum elevation of nearly 1,100 m) (Figure 2.10a). Despite these elevation differences, reaches underlain by granodiorite and volcaniclastic bedrock had similar average channel width measurements (Figure 2.10b), whereas reaches underlain by sedimentary rocks or alluvial deposits were associated with the highest measurements of channel width (Figure 2.10b). The maximum modeled width at MAQ was 36 m and located in an area underlain by sedimentary rocks, with the average channel width at MAQ discharge scenarios across all the reaches remaining at 6.6 m. Because channel width values have been shown to be correlated to the drainage area (Wohl et al., 2004), I further compare channel width by using the normalized wideness index (k_{wn}), which is calculated by using the equation below:

$$k_{wn} = WA^{-b_{ref}} \quad \text{(Eq.2.2)},$$

where W is the channel width, A is the drainage area, and b_{ref} is the reference wideness exponent (set to 0.47 based on my data) (Allen et al., 2013). Accounting for drainage area through the normalized wideness index shows that channels in this drainage basin that are underlain by granodiorite had, on average, narrower channels than those underlain by volcaniclastics and sedimentary rocks.

Comparing width to basin average elevation reaffirms that volcaniclastics are generally limited to the higher elevations of the watershed, whereas granodiorites and sedimentary rocks can be found in both low- and high-elevation areas (Figure 2.11a and b). Figure 2.11b reveals that the variability of channel

width is larger for rivers underlain by granodiorites and sedimentary rocks, whereas it is mostly confined to channel widths <10 m for areas underlain by volcaniclastics.

Lastly, I can compare the drainage area to the average channel width measurements of the Caonillas watershed to other datasets found in the literature and collected from across the world (Figure 2.12). The Caonillas watershed fit of $w \sim 1.97A^{0.47}$ falls in line with other hydraulic geometry relations in the literature (see Table 1 in Wohl and David (2008)); most notably with Montgomery and Gran (2001) and Tomkin et al. (2003). Comparing my preliminary analysis of the Caonillas watershed to alluvial fits further suggests that, with an increase in drainage area, bedrock channels in Puerto Rico increase in width at a faster rate than both mixed bedrock-alluvial rivers and gravel-bedded rivers (Figure 2.12).

2.4 Discussion

2.4.1 Implications and Outlook

The coupled use of TopoToolbox with HEC-RAS provides a straightforward and relatively simple approach to derive channel width measurements at comparable flow conditions. Although the applications of this method are extensive, it especially offers an opportunity to improve bedrock erosion and incision modeling capabilities. The stream-power model—by far the most commonly used method to model bedrock river incision—expresses river incision as a function of bedrock erodibility, river discharge, and slope (Whipple and Tucker, 1999; DiBiase and Whipple, 2011; Perron and Royden, 2012; Lague, 2014). Despite its widespread use, the typically-used form of the stream-power incision model does not explicitly include channel width—a channel geometry measurement that plays a first-order role in influencing energy dissipation, and thus sets the pace of bedrock incision and channel erosion of bedrock river systems (Lavé and Avouac, 2001; Yanites and Tucker, 2010; Whipple et al., 2013; Lague, 2014; Spotila et al., 2015; Yanites, 2018). Instead, the bedrock incision model relies on a simple drainage area scaling relationship where the drainage area exponent is thought to account for power-law scaling between width and drainage area or discharge. Importantly, the assumed drainage area:width scaling relationship is largely derived from alluvial rivers. Until now, the dearth of bedrock data in the literature

(largely due to physical constraints to gathering field data of bedrock channels) has driven researchers to assume that these scaling relationships are the same in both alluvial and bedrock rivers. At the same time, many have noted that, where bedrock field measurements exist, a more complicated story that is shaped by sediment supply, bedrock, slope, discharge, rock strength, and climate emerges (Finnegan et al., 2005; Wohl and David, 2008; Whipple et al., 2022) and widespread application of this method has the potential to better define and understand these controls that might lead to improvements of bedrock incision models.

Having validated this method across dozens of field locations in Puerto Rico, I find that my workflow provides promise for disentangling these relationships and developing a better understanding of bedrock channel width where high-resolution topographic data are available and sufficient stream gauging data exists to approximate a reference flow condition across the landscape. This method has even greater future potential for research across the continental United States, where the USGS's 3D Elevation Program (3DEP) is working to accumulate freely-available high (1 m) resolution airborne LiDAR data across the country (Stoker, 2022). As of the end of the 2021 fiscal year, the 3DEP program has acquired 86% LiDAR coverage across the continental United States, and is on track to complete its data acquisition of the entire United States by the end of the 2026 fiscal year (Stoker, 2022).

An additional advantage is the affordability and simplicity of data acquisition—requiring remotely sensed data, rather than expensive, risky, and time-consuming field campaigns. Gathering these data, therefore, becomes much more accessible for researchers with a limited budget. At a minimum, an increased number of bedrock channel width measurements can improve incision modeling results by either tailoring the simple scaling relationships specifically to bedrock rivers, or directly incorporating channel width into an incision model. On a broader scale, the ability to compare channel width measurement across an array of parameters can produce a better overall understanding of what impacts channel width, and, therefore, bedrock river geometry.

2.4.2 Method Limitations

In light of the promising data results, I recognize that my presented method has a number of intrinsic limitations. Most importantly, my method relies on a bare-earth high-resolution DEM derived from LiDAR to measure the properties of river geometry. The near-infrared wavelengths are most frequently used for topographic LiDAR DEM applications, however, they generally cannot penetrate through water and produce accurate measurements of the channel bottom (McKean et al., 2011). As a result, my method routes a given flow over the water surface of the river at the time that LiDAR was conducted. With this in mind, I need to (1) assume that LiDAR was not collected during high flows, (2) limit the analysis and interpretation of water depth in my modeling calculations, and (3) recognize that channel width measurements likely become less accurate for larger rivers, where bed roughness is much less than water depth at the time of acquisition. Although this method can still predict a reference channel width above the discharge during LiDAR acquisition, I cannot use it to accurately determine rating curves (such as shown in Figure 2.3) for these larger rivers. In addition, I recognize that the LiDAR DEM I used for my method has a resolution of ~1 m. As a result, I only considered modeled river width measurements of ≥2 m, limiting my ability to capture width measurements of narrower, low drainage-area (ca. 1 km^2) bedrock channels that may have width measurements close to this resolution. Although my preliminary analysis suggests that the method does a reasonable job at these small drainage areas (Figures 2.4 and 2.6), selecting for only channels ≥2 m wide may bias the channel width measurements of small (≲1 km^2) drainage areas. However, with higher resolution DEMs and higher magnitude reference flow conditions, this method can extend to lower drainage areas, thereby reducing this bias. Lastly, I applied the MAP to estimate discharge for ungauged areas, but realize that data results can be improved by using field discharge measurement methods (i.e. installing dataloggers to establish a stage-discharge rating curve, utilizing current meters, or employing artificial tracers) (Tazioli, 2011) or implementing water routing algorithms (Perumal et al., 2007; Corato et al., 2011).

2.5 Conclusions

Through validating this workflow against both USGS gauging station data and field data, I have demonstrated the possibility of efficiently acquiring comparable bedrock channel width measurements across a large area without the need for expensive, often dangerous, and time-consuming field campaigns. By the implementation of similar flow conditions (at Mean Annual Discharge) across an area of interest, I show that this method further offers a way to reduce the subjectivity of field measurements and produce comparable results across different reaches and locations. As a result, I present an avenue for researchers to efficiently garner landscape- and watershed-scale bedrock channel width measurements that allow for comparisons among locations across the world that span a breadth of climates, vegetation abundance, river types, and flow regimes. My preliminary analysis of the Caonillas Watershed demonstrates the breadth of data that can remotely be acquired and analyzed through this process. By presenting a simple workflow and user guide in light of the increasing availability of high-resolution LiDAR data, I hope that this method can be used in the future to push forward the understanding in the literature of bedrock channel width, as well as improve the modeling capabilities of models, such as the bedrock incision model, that rely on channel width to produce reliable results.

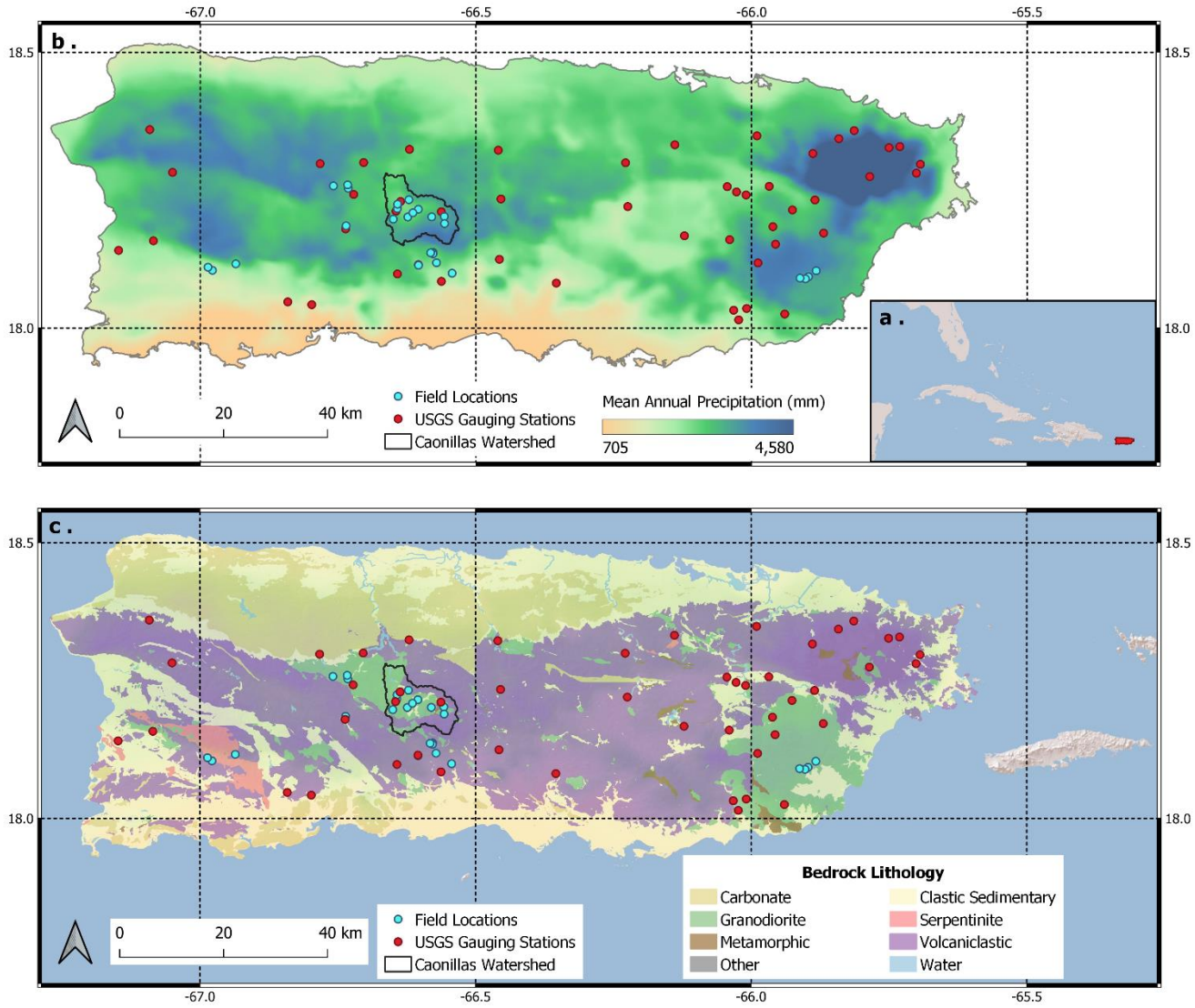

Figure 2.1. (a) The location of Puerto Rico in relation to Florida and Cuba. (b) A map of Puerto Rico showing changes in the Mean Annual Precipitation across the island (PRISM Climate Group, 2022). The locations of USGS gauging data and field observations used to verify this method are further illustrated, as well as the extent of the Caonillas watershed (analyzed in Part 3). (c) A simplified geologic map of Puerto Rico, showing changes in bedrock lithology across the island.

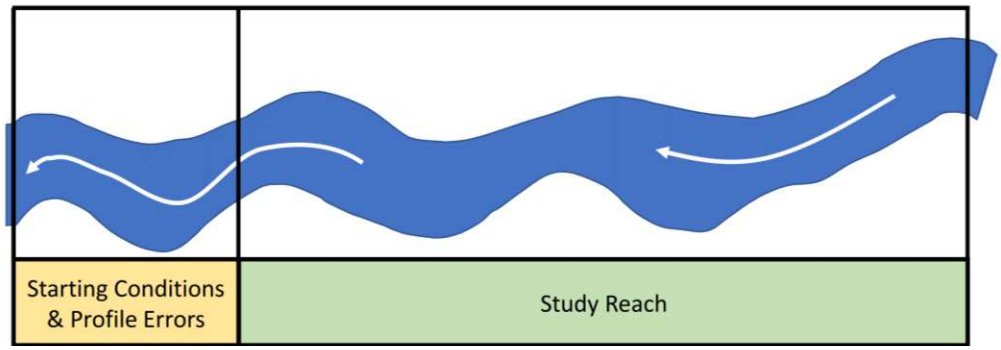

Figure 2.2. A cartoon based off of Figure 3-1 in the HEC-RAS Hydraulic Reference Manual, showing the placement of the study reach location (e.g. data values used) upstream of the starting boundary conditions, thereby limiting the effect that initial boundary conditions (such as an incorrect water surface elevation estimate) can have on the used data values (USACE, 2016).

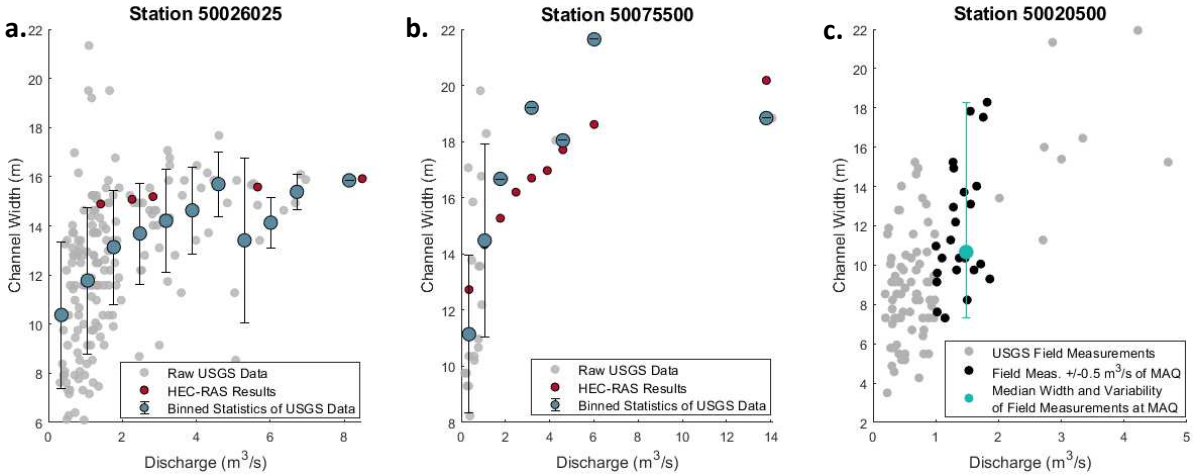

Figure 2.3. :(a) and (b) show raw USGS field measurements indicating changes in river width at Stations 50026025 and 50075500, respectively, across different discharges. HEC-RAS channel width measurements generally produce measurements comparable to the USGS data. (c) Shows the raw USGS field measurements at Station 50020500. Gray points indicate all field measurements, whereas the black points are the measurements collected within 0.5 m^3/s of the MAQ at the station (1.48 m^3/s), and the green point and associated error bars reflect the median width measurements, as well as minimum and maximum measurement.

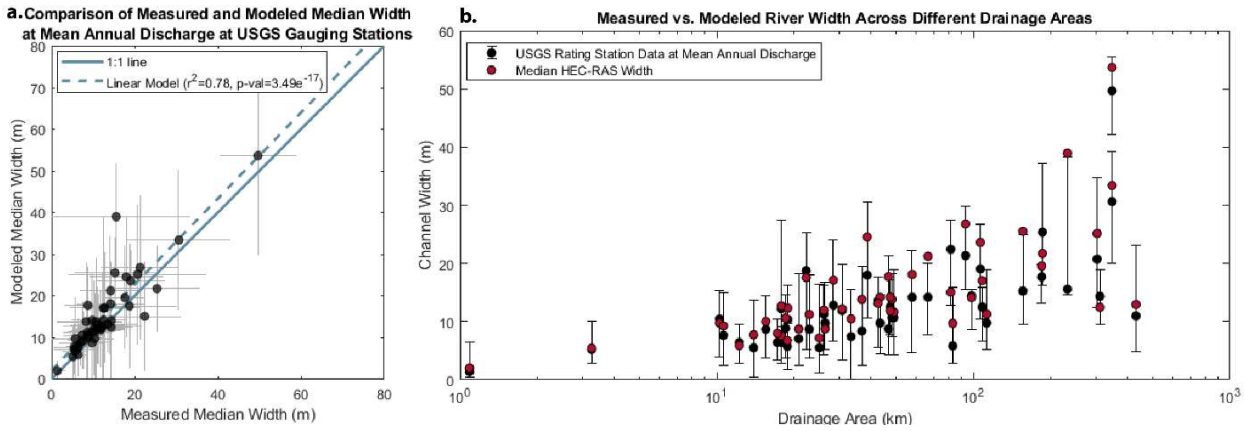

Figure 2.4. (a) A comparison of modeled HEC-RAS width values in relation to USGS field measurements collected at comparable discharge values (MAQ). Error bars indicate 2 standard deviations of error. Most HEC-RAS width measurements (including error) fall on the 1:1 line, indicating that the model generally does a good job at predicting channel width measurements across different locations at the MAQ. (b) A comparison of modeled HEC-RAS width values in relation to USGS field measurements collected at comparable discharge values (MAQ), shown in relation to drainage area. Error bars indicate the maximum and minimum USGS field measurement values at each station. Most HEC-RAS width measurements fall within the variability in USGS field measurements collected at a comparable discharge across a wide span of drainage areas.

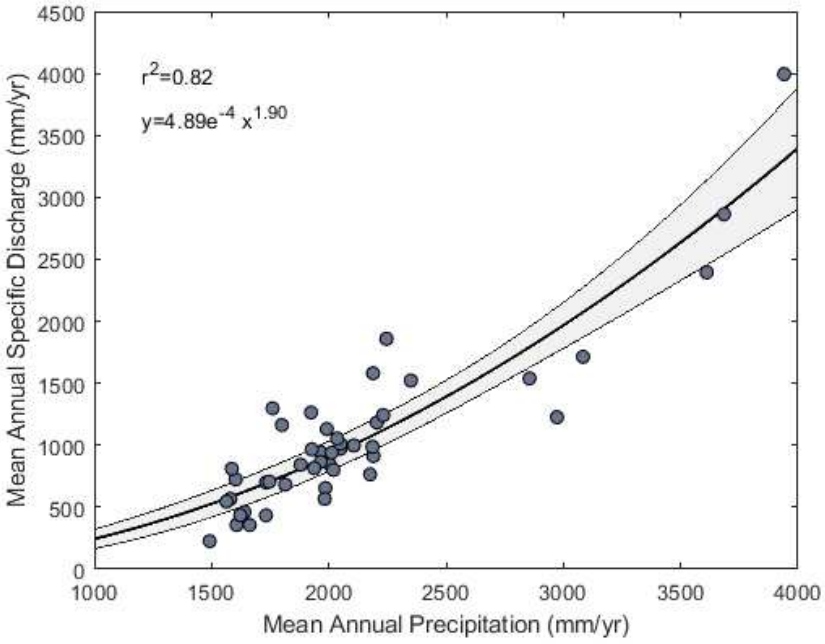

Figure 2.5. A comparison of the Mean Annual Precipitation in relation to the Average Specific Discharge across the 49 gauging stations in Puerto Rico. The shaded area represents the 95% confidence interval. 1-year and 2-year RI discharges are associated with a reduction in R-Squared value (Figure A1).

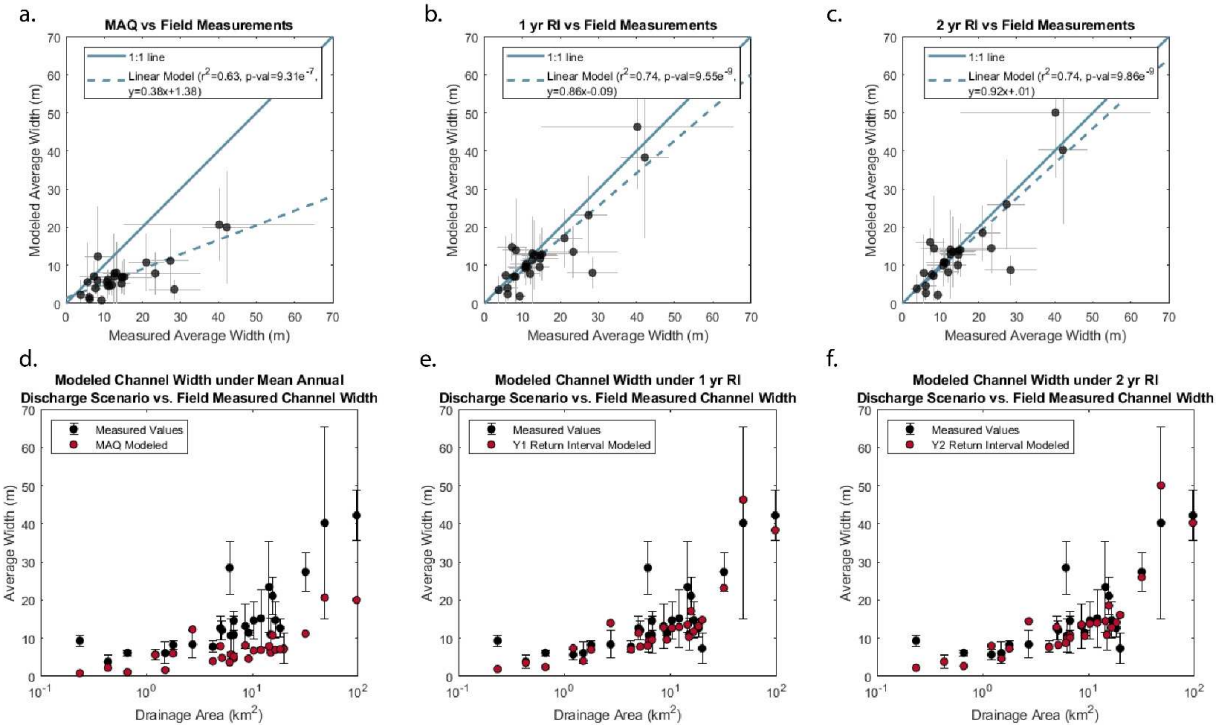

Figure 2.6. (a-c) A comparison of modeled average width and measured average width under a MAQ, 1- and 2-year discharge scenario. Error bars represent two standard deviation uncertainty. Measurements that fall on the 1:1 line indicate good agreement between field measurements and modeled width measurements. (d-f) Modeled channel width compared to field measured values, shown across different drainage areas. These results indicate a systematic underestimation of channel width at MAQ discharges, and support the use of 1- or 2-year RI discharge estimates for bankfull channel width measurements.

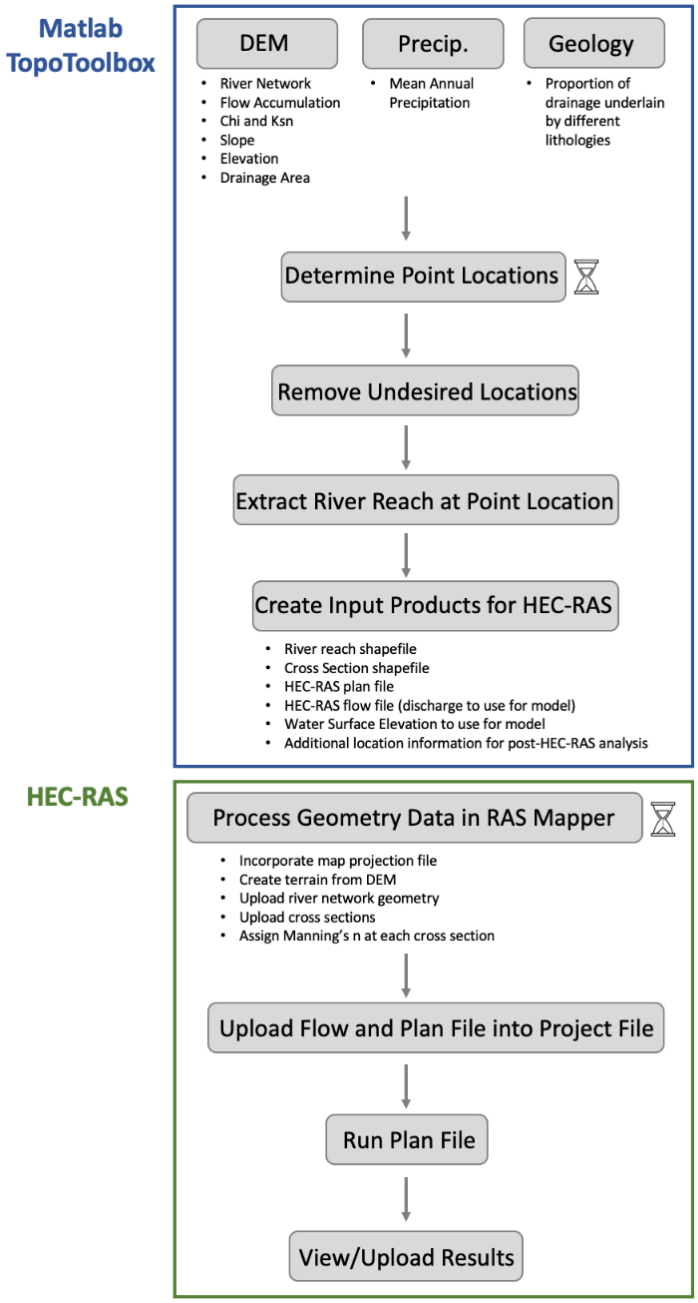

Figure 2.7. A general overview of the steps required to model channel width measurements. Bullet points outline relevant data products obtained from different inputs, or outline the general steps within a larger process. The hourglass symbols indicate the steps that take significantly more time (on the order of 1-3 hours) to process.

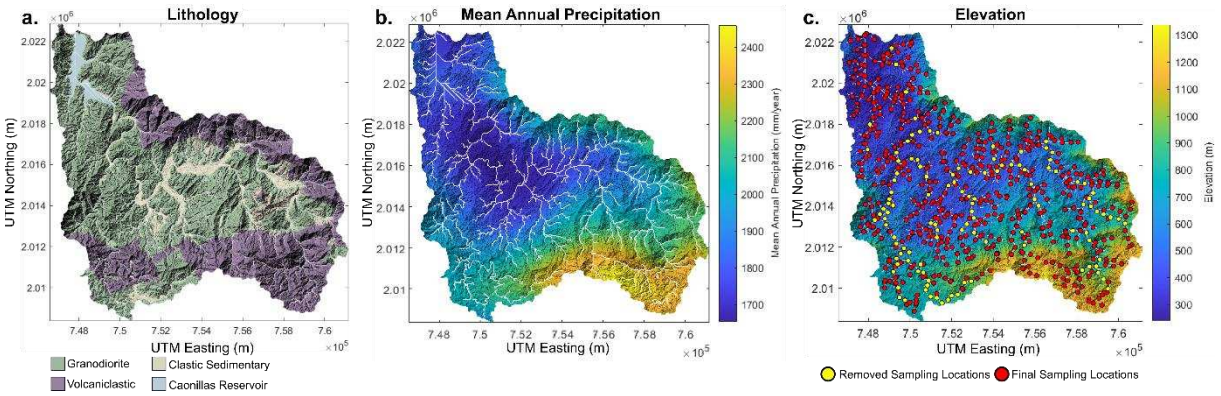

Figure 2.8. (a) An image displaying the extent of the Caonillas watershed, with the landscape hillshade overlain by the geologic map. Changes in color indicate different lithological units. (b) A map of the variability in the Mean Annual Precipitation across the Caonillas watershed, as well as a (c) digital elevation model indicating changes in elevation across the drainage area. Red points indicate locations removed in the 'filtering' process, and yellow points show the final sampling locations.

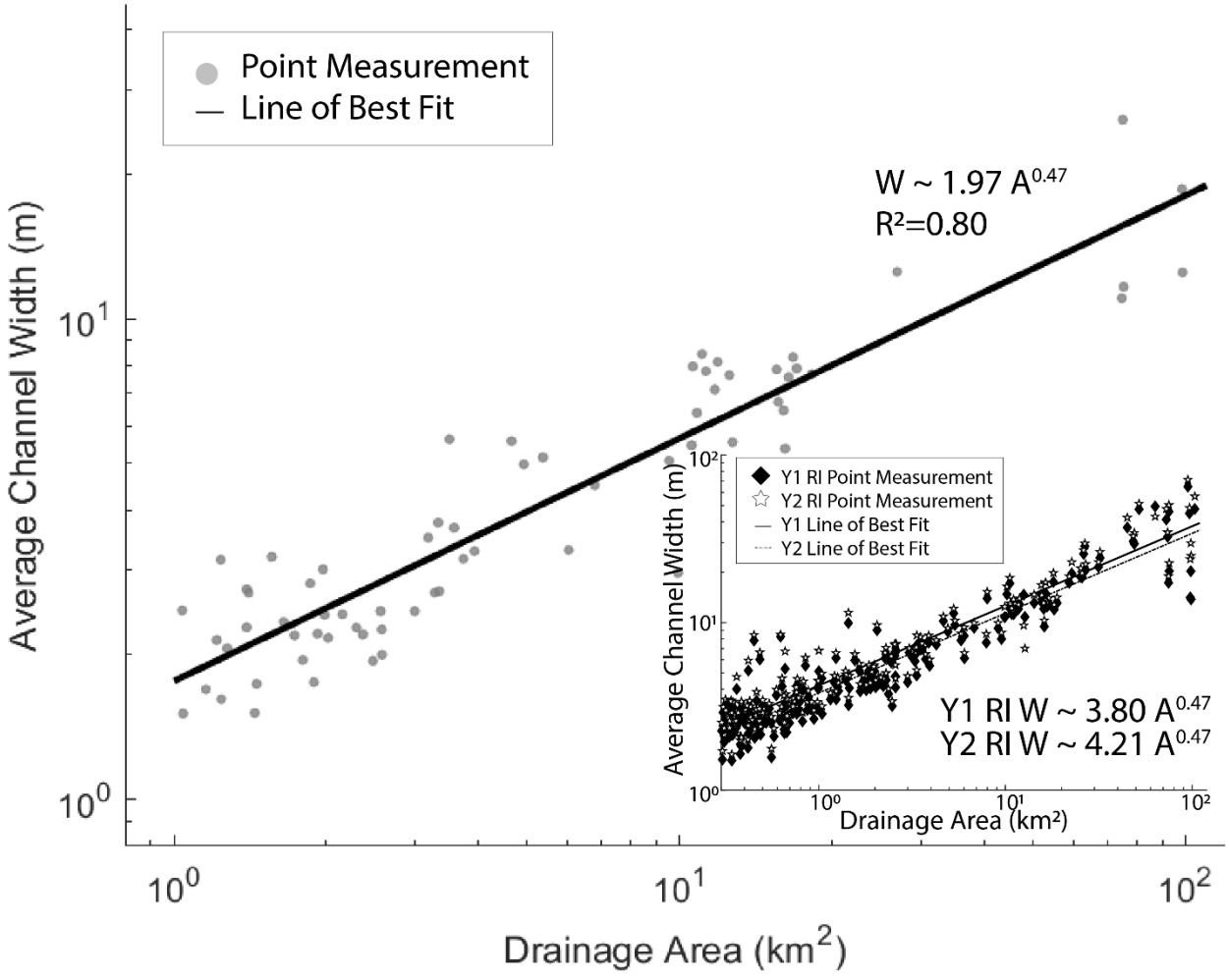

Figure 2.9. Average channel width of crystalline bedrock (n=116) compared to the drainage area of reaches found in the Caonillas Watershed. There appears to be a strong relationship (r^2=0.80) between drainage area and average channel width.

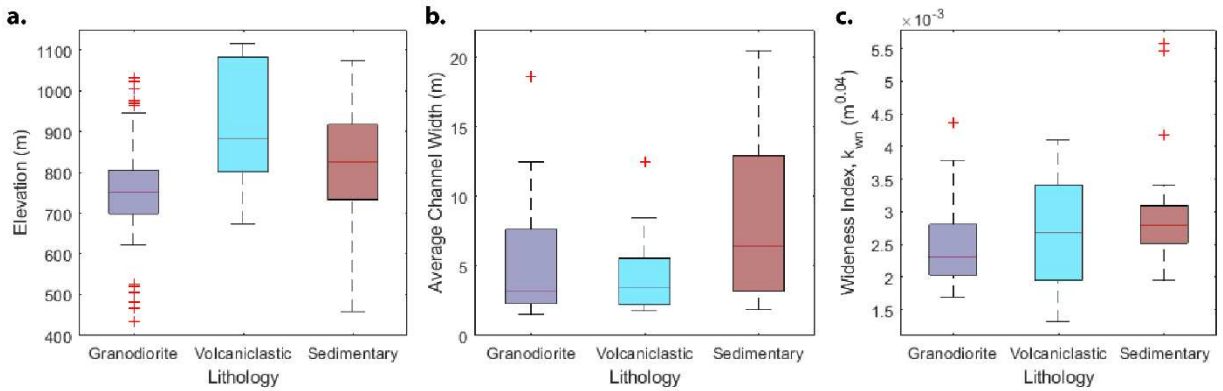

Figure 2.10. A comparison of the distribution of (a) analyzed reach elevation, (b) average channel width, and (c) the wideness index according to bedrock lithology in the Caonillas watershed.

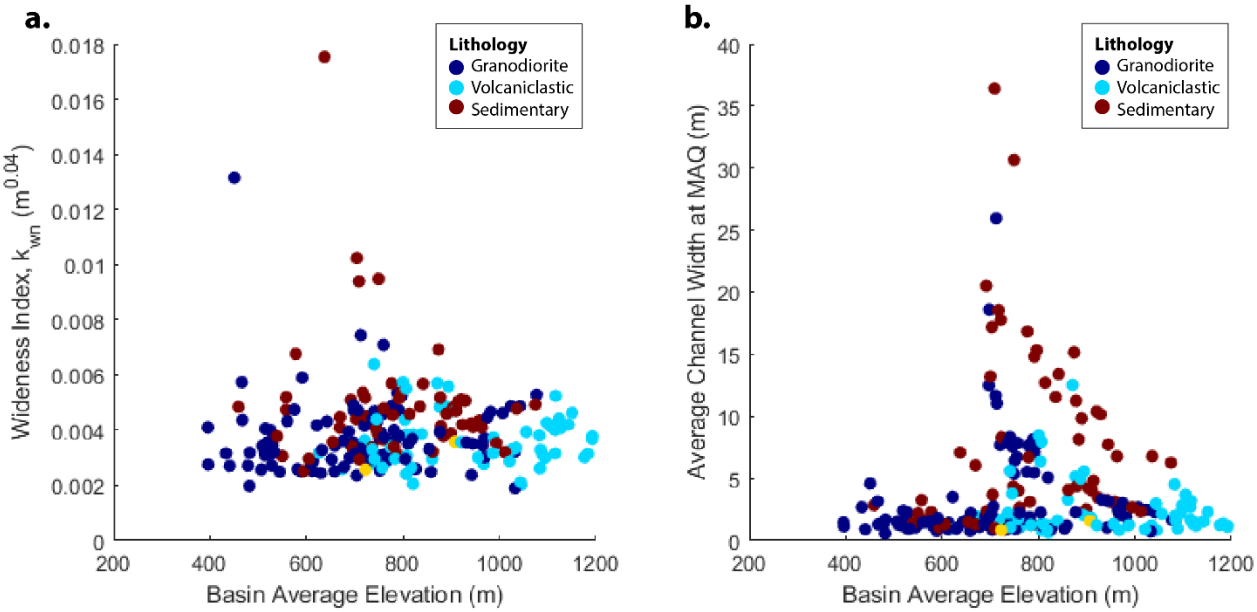

Figure 2.11. A preview of parameters that can be analyzed from this method. Here, we compare changes in basin average elevation to (a) the wideness index, and (b) the average channel width.

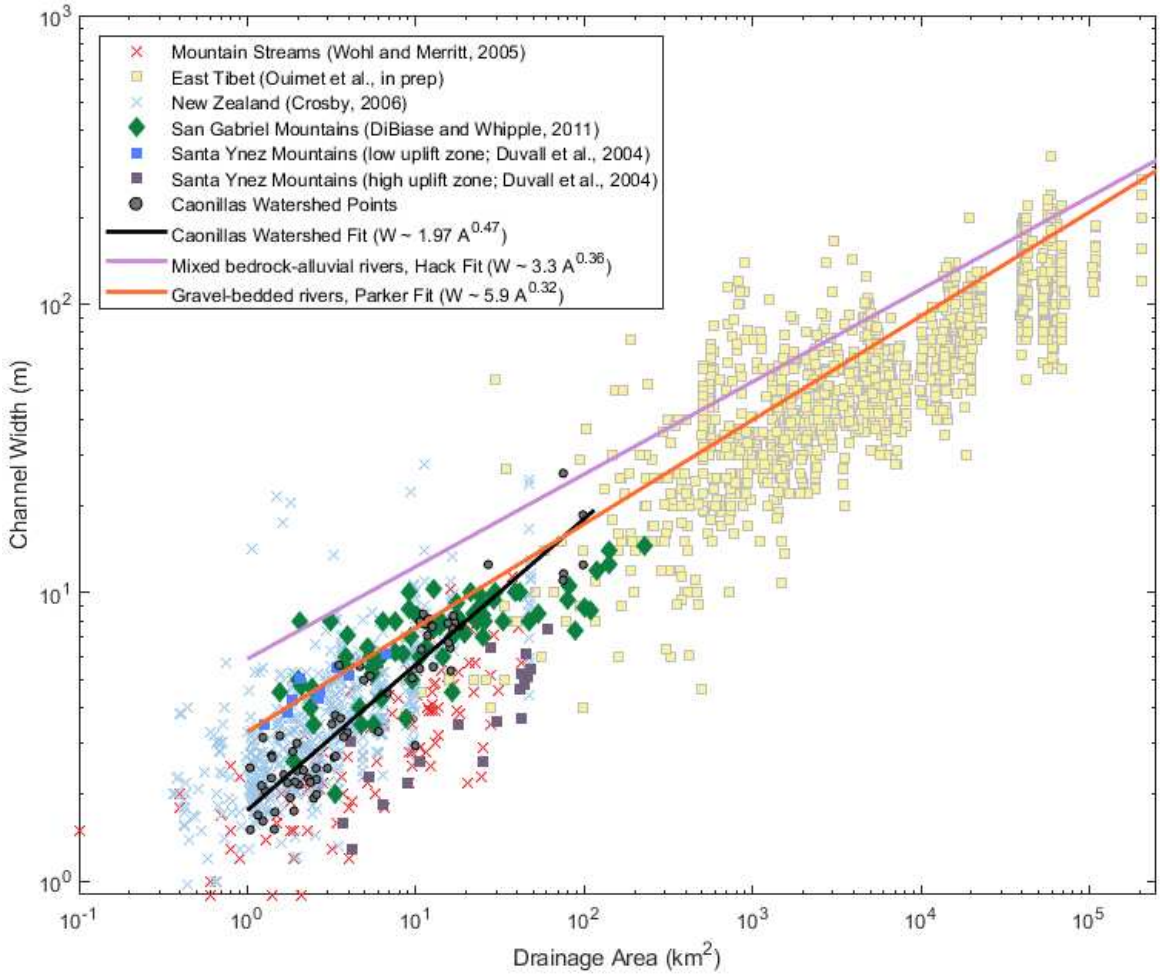

Figure 2.12. A modified figure from Whipple et al. (2022), overlain by data from the Caonillas watershed. These results suggest that channel width of bedrock rivers in the Caonillas watershed increase with drainage area at a slightly faster rate than alluvial rivers and other mountain stream measurements collected across the world.

CHAPTER 3: VARIATIONS AND CONTROLS ON CHANNEL WIDTH IN TROPICAL BEDROCK RIVERS, PUERTO RICO, USA

3.1 Introduction

Bedrock channel width is a critical measure of channel hydraulics, as it affects the magnitude of shear stress imparted by a flow on the channel bed and plays a first-order role in determining bedrock incision rates (e.g. Finnegan et al., 2005; Whittaker et al., 2007; Turowski et al., 2009; Yanites and Tucker, 2010). It is also relevant to understanding the long-term evolution of mountains because bedrock rivers form the "backbone" of these landscapes, encompassing ~80-90% of mountain relief, and they set the lower boundary condition on adjacent hillslopes (Whipple et al., 2022). Despite its importance to various fields, bedrock channel width is rarely measured because bedrock rivers are often found in rugged topography that is physically challenging to access. Although satellite imagery has become more available and has expanded remote access to visual channel width extraction of rivers worldwide (Lavé and Avouac, 2001; Fisher et al., 2012, 2013; Allen et al., 2013; Yamazaki et al., 2019; Lin et al., 2020), data obtained through imagery is often either limited in resolution (typically ≥30m) or affected by physical obstructions (e.g. cloud cover or vegetation cover). In part due to these data limitations, researchers often estimate the bedrock channel width throughout a river network based on a drainage area-width or discharge-width scaling relationship, typically defined by a global compilation of data from mainly alluvial rivers (e.g. Finnegan et al., 2005; Whipple et al., 2022). Despite the utility of these scaling relationships, the main factor that determines bedrock channel width is still debated, again stemming from the scarcity of measurements.

A variety of factors have been shown to influence channel width, but some of the most commonly invoked are bedrock lithology and rock strength, spatial or temporal variation in rock uplift, sediment supply, rainfall and associated discharge, and sediment grain size distributions. Montgomery and Gran (2001) analyzed surveys of bedrock channels in Oregon and Washington and found that rock material

strength played an important role in determining channel width. Their data, as well as that of other field studies, have found that more erosion-resistant material produces narrower channels (Wohl and Ikeda, 1998; Montgomery and Gran, 2001). Others have found that width is further influenced by temporal or spatial variation in rock uplift rates (Finnegan et al., 2005; Whittaker et al., 2007; Amos and Burbank, 2007). Sklar and Dietrich (2004) introduced the concept of sediment clasts as 'tools' or 'cover' that increase or inhibit channel incision, respectively. More specifically, transported sediment can act to increase bedrock channel incision through abrasion and plucking of exposed bedrock, or can act as cover to inhibit vertical incision and promote channel widening (Turowski, 2018; Baynes et al., 2020). Turowski and Hodge (2017) highlighted the temporal importance of this sediment supply, finding that when the sediment supply is variable, the recent supply history has a primary control on the balance of the 'tools' and 'cover' in channels.

In addition to the volume of sediment in the river, others have emphasized the role of sediment grain size in bedrock channel erosion. Studying gravel-cobble streams, Eaton et al. (2020) found that the coarse tail of the bed sediment distribution (D_{90}) was a better predictor of controls on channel geometry relative to finer fractions (i.e. D_{50}). Nativ et al. (2022) also highlighted the importance that larger clasts have on bedrock river incision, with field data from Taiwan pointing to an association between a higher concentration of rarely-mobile boulders and a widening of bedrock streams.

Previous research on bedrock channel width has based their findings on limited (on the order of 10s to 100s of river reaches) field and flume analyses. With the development of a new and remotely based bedrock channel width extraction method that combines high-resolution Digital Elevation Models (DEMs) with stream hydrology modeling software, I now have the opportunity to acquire a large number of bedrock channel width measurements across broad spatial scales (Chapter 2). Here I use this approach to extract bedrock channel width measurements across the tropical island of Puerto Rico to explore hypotheses regarding controls on bedrock channel width. Specifically, I seek to test the hypothesis that bedrock material strength plays a first-order role in determining bedrock channel width. In line with

Montgomery and Gran (2001)'s findings, I predict that in crystalline bedrock the stronger and more resistant rock type is associated with narrower channels, whereas the weaker and less resistant rock type is associated with wider channels.

To test my hypothesis, I extract 4,184 individual bedrock channel width measurements from streams incising crystalline bedrock (predominately granodiorite, intermediate-to-mafic volcaniclastic, and ultramafic serpentinite units) using the method of Chapter 2. I then evaluate measured and normalized bedrock channel width across different physical parameters (i.e. by rock type, proxies for rock strength through Schmidt hammer measurements, drainage area, and sediment grain size) to explore whether lithology plays an important role in channel width, and to test the relationships between other properties identified as factors that can affect bedrock channel width. My analyses reveal that bedrock lithology appears to play a role in river width of small (<10 km^2) drainage areas. At these small watersheds, the weaker rock is associated with narrower channels than the more resistant rock types.

3.2 Setting

In this study, I analyze channel width of crystalline bedrock rivers in Puerto Rico. Located in the Caribbean (18°N and 66°W; Figure 3.1a), Puerto Rico's subtropical marine climate is defined by year-round warm temperatures (typically ranging between 70°F and 90°F), ensures that precipitation is limited to rainfall (The Southeast Regional Climate Center, 2019)—thereby simplifying the potential influence of more extreme seasonal impacts of rain and snow. Puerto Rico is characterized by a dramatic variation in topography, with the crystalline bedrock forming the most rugged topography on the island (e.g. the central Cordillera Central mountain chain and the northeastern Luquillo Mountains), whereas sedimentary bedrock creates low-gradient topography toward the south, and carbonates form karst topography toward the north (Figure 3.1b and c). The steep and variable mountainous terrain associated with the crystalline bedrock makes Puerto Rico an ideal landscape for analyzing river width changes according to drainage area and channel slope. Lastly, Puerto Rico's climate is characterized by highly variable precipitation that ranges from approximately 732 mm to over 4,000 mm of rain per year (Figure 3.1d; NOAA, 2011). The

volume of rainfall across the island is spatially modulated by an orographic effect of the mountains and temporally influenced by tropical depressions, storms, and hurricanes (Ehlmann, 1968; Calvesbert, 1970). With the mountains experiencing remarkable annual rates of rainfall, analyzing the crystalline bedrock rivers in this terrain provides an opportunity to test the influence of rainfall and discharge (identified as important factors in the literature) on channel width. Combining the topography, climate, and precipitation found on the island, the different parts of Puerto Rico can be simplified into 5 general classes of micro-climates or Ecozones (Figure 3.1e).

3.3 Methods

3.3.1. Channel Width Modeling

The general method of modeling channel width for this analysis is detailed in Chapter 2. This approach uses high-resolution topography (preferably a LiDAR-derived DEM with ≤1 m resolution) and a one-dimensional backflow water equation solved in HEC-RAS (USACE, 2016). In this approach, one determines a stream reach of a given length (in this analysis, I used a length of approximately 200 m) and uses HEC-RAS to route flow through the stream segment at a given user-defined discharge and channel roughness. The stream reach is long enough to avoid edge effects associated with the downstream boundary conditions, and once the flow is modeled, channel width measurements (defined by the contact of the water surface and the channel walls) are extracted from the cross sections drawn along the stream segment. Cross-sectional channel width measurements located within approximately 50 m of the location of interest (typically 9-10 measurements, spaced 10 m apart) are combined to produce a mean or median channel width for each stream reach location.

In this analysis, I model small (≥ two pixels wide) channels in Puerto Rico using a ~1m DEM derived from 2018 LiDAR campaigns (OCM Partners, 2022). Due to the large spatial extent (the island of Puerto Rico covers an area of ~9,000 km^2) of this analysis, paired with the high-resolution DEM, I divided the study area into smaller, more computationally digestible areas. Because I conducted my analysis using a stream-based approach, I decided to delineate the island based on the twelve-digit

hydrologic unit watersheds defined by the Watershed Boundary Dataset (U.S. Geological Survey, 2016). My emphasis is to compare bedrock channel width in crystalline bedrock, so I avoided estuaries and coastal rivers by imposing a 3 km buffer from the coastline. In addition, I also avoided carbonate bedrock that generally forms the karst topography on the island. Lastly, I did not analyze the watershed near the City of San Juan, as many rivers in this watershed appeared to be modified by urban development and would not be representative of unaltered bedrock rivers.

We used a geologic map provided and digitized by the USGS (U.S. Geological Survey, 1998), as well as a raster data set of the modeled mean annual precipitation between 1963 and 1995 (PRISM Climate Group, 2022). To incorporate bedrock geology and isolate channels flowing over crystalline units, I used the unit descriptions to simplify lithology into 8 categories: carbonate, granodiorite, metamorphic, clastic sedimentary units, serpentinite, volcaniclastic, water, and other. Each of these datasets was aligned and resampled to the same resolution.

In this analysis, I sought to analyze river width across a breadth of drainage areas. To balance my goal of including rivers with small (~1 km^2) drainage areas with my DEM-based resolution limit of channels at least 2 m wide, I applied an estimated 1-year Recurrence Interval (RI) discharge to the model based on the results of Chapter 2. To estimate the 1-year RI at ungauged locations throughout Puerto Rico, I used (Chapter 2) an analysis of 47 USGS gauging stations in Puerto Rico with records spanning up to 60 years to define 1-yr RIs (Figure 3.2). They show that upstream average MAP at these stations is a reasonable proxy for the 1-yr RI (Figure 3.2). While simple, this scaling relationship between mean upstream MAP and 1-yr RI allows me to reasonably predict MAP at ungauged stations. See Chapter 2 for a detailed description of this approach.

Once channel width was modeled and derived for each point, I conducted a series of post-processing steps to filter out unwanted channels. First, I visually inspected the channels and channel networks in relation to satellite imagery and removed segments that appeared to be anthropogenically altered by development (for example, segments with 90-degree bends or straight segments bounded by

housing developments). Next, I only selected channel reaches that were located on crystalline bedrock (granodiorite, volcaniclastic, and serpentinite). I further only analyzed channels that received precipitation within the range of the USGS gauging stations that were used to calibrate the model—in my case, this limited me to areas that experience at least 1,500 mm precipitation per year. Due to the resolution constraints of the DEM, I chose to only analyze streams greater than 2 m in width at 1-year RI flow conditions. Because I did not want to directly modify the response variable, a preliminary analysis of channel width by drainage area allowed me to designate a minimum of 0.5 km^2 drainage area for my data analysis where modeled channel widths are ≥2 m.

Channel width systematically increases with upstream contributing drainage area (e.g. Wohl and David, 2008). To avoid this drainage area (or discharge) dependence and allow for comparison of channel width across different drainage areas (or discharge magnitudes), I calculate the normalized wideness index (k_{wn}):

$$k_{wn} = WA^{-b_{ref}} \quad \text{(Eq. 3.1)}$$

where W is the channel width, A is the drainage area, and b_{ref} is the reference wideness exponent (Allen et al., 2013; Lague, 2014).

3.3.2. Field Methods

We conducted pebble counts (Wolman, 1954) at 30 locations (12 granodiorite,13 volcaniclastic, and 5 serpentinite) to characterize grain size distributions (Table B1). From each pebble count, I counted a minimum of 100 pebbles at each site, and from these data, I extracted the clast size representative of the 50^{th} and 84^{th} percentile, noted the bedrock lithology and calculated the predominate upstream rock type at each surveyed location. To estimate and compare the relative rock strength in the field, I used a Schmidt hammer—a small device that measures the approximate uniaxial compressive strength of bedrock (Goudie, 2006; Niedzielski et al., 2009; Zondervan et al., 2020). Using the Schmidt hammer rebound measurements as a proxy for rock hardness and erodibility, I collected relative rock hardness

measurements across 22 locations (7 granodiorite, 10 volcaniclastic, and 5 serpentinite) in unweathered bedrock channel outcrops (Table B1). Sites were selected to encompass a diversity of rock types, and at each site I took ~100 Schmidt hammer measurements to account for local variability of outcrops. I performed a total of 904 measurements of granodiorite bedrock, 821 measurements of volcaniclastic bedrock, and 473 measurements of serpentinite bedrock.

Estimated biotic bankfull channel width measurements were collected in the field using a laser range finder. The channel width associated with 1-year RI discharges was estimated using field clues, including a lack of vegetation regrowth—an assumption that was validated through modeling channel width (see Chapter 2). For this analysis, all Schmidt hammer measurements were used to evaluate differences in rock strength based on lithology. Grain size distribution was only compared to channel width at field locations where these two methods overlapped (18 locations; Table B1).

3.4 Results and Discussion

3.4.1. Bedrock Strength, Erodibility, and Incision Process

In this analysis, I evaluate whether bedrock channel width is primarily a result of lithological differences in rock strength. More specifically, I assess whether bedrock streams in Puerto Rico follow the trend found by Montgomery and Gran (2001)—where channels incised in more resistant bedrock were narrower than those in less resistant bedrock. In Puerto Rico, I focus on three primary types of crystalline bedrock: granodiorite, volcaniclastic, and serpentinite (Figure 3.1c).

Median Schmidt hammer rebound values of 71 and 72 for granodiorites and volcaniclastics, respectively, suggest that the rock strength is not significantly different between the two rock types (Figure 3.3a). A much lower median rebound value of 25 in the serpentinite bedrock indicates that serpentinite is much weaker than both volcaniclastics and granodiorite (Figure 3.3a). While fracture density is not quantified in the field, the Schmidt hammer results are consistent with qualitative observations of fracture density, size and spacing among the three rock types (Figure 3.3b-d). Fracture characteristics are generally similar in bedrock channels in the granodiorites and volcaniclastics, although

there are more variable fracture patterns in the latter due to variations in bedding within these units (Figure 3.3b and c). The serpentinite units show much more pervasive fracturing than the granodiorites and volcanic clastic units (Figure 3.3b-d). In the field, I further observed that bedforms in the granodiorites and volcaniclastics largely consist of flutes and potholes, indicating a prevalence of abrasion as the dominant bedrock incision process relative to plucking (Figure 3.3b and c) (e.g. Whipple et al., 2000; Whipple, 2004). The serpentines exhibit many of these same bedrock bedforms (indicating the dominance of abrasion), but also show more evidence of plucking in some locations (Figure 3.3d). Collectively, these measurements and observations suggest that the granodiorites and volcaniclastics have comparable bedrock strength and erodibility, whereas the serpentinites are weaker and more erodible. Furthermore, my observations suggest that the dominant incision process across all rock units is abrasion.

3.4.2. Bedrock and Channel Width

We compared modeled channel width by lithology across a range of drainage areas (0.5 km^2 to >100 km^2). The scaling for each bedrock unit shows that channel width changes differently with increasing drainage area across the units, where serpentinites and volcaniclastics show similar and higher sensitivity to drainage area, and granodiorite channel width is comparatively less sensitive to drainage area (Figure 4b-d). In addition, at small drainage areas <6-10 km^2, reaches underlain by serpentinite are consistently narrower than those underlain by granodiorite and volcaniclastics (Figure 3.4a). These findings contradict my hypothesis that weaker lithological units would create wider channels.

Because measured channel width can be correlated to drainage area, I further compared drainage area-normalized channel width by bedrock and found similar trends to the total channel width (Figure 3.5a). These results can be statistically evaluated through a comparison of sample means. Analysis of variance (ANOVA) of channel width of drainage areas less than 10 km^2 found that reaches underlain by granodiorites (n= 806) were significantly ($p<0.001$) wider than those underlain by volcaniclastics (n=2,603) and serpentinites (n= 124). The difference of means between reaches underlain by

volcaniclastics and serpentinites, however, was not significantly different. For drainage areas greater than 10 km^2, there did not appear to be a significant difference in average channel width across the population means (n=115 for granodiorites, n=530 for volcaniclastics, and n=6 for serpentinites). These results suggest that bedrock is an important factor in determining channel width at smaller (≤10 km^2) drainage areas.

Interestingly, my results show that in Puerto Rico, weaker bedrock is associated with the lowest normalized channel width index for rivers draining <10 km^2, indicating that the weaker bedrock produces narrower channels. These results, therefore, contrast the findings of previous studies (e.g. Wohl and Ikeda, 1998; Montgomery and Gran, 2001). While the sample size is smaller for drainage areas >10 km^2, the impact of rock type on the normalized wideness index is not clear, hinting at the potential of other controlling factors.

3.4.3. Channel Width Across Ecozones

Numerous studies have criticized the notion that bedrock channel width scales directly with one parameter, and suggest that width is rather the result of an interplay of multiple factors (for example sediment supply, hydraulic roughness, vegetation, slope, and climate) (e.g. Lague, 2014; Yanites, 2018). To account for covariation of rock type, topography, soil properties and vegetation—which can all impact geomorphic and hydrologic processes—we take a more generalized look at potential rock type controls on bedrock channel width by evaluating changes across microclimates or Ecozones (e.g. Holdridge Ecological Lifezones; (Holdridge, 1967; Ewel and Whitmore, 1973). The microclimates found in Puerto Rico encapsulate 5 Ecozones: dry forest, moist forest, subtropical wet forest, lower montane wet forest, and rain forest (Figure 3.1f). These Ecozones not only account for differences in precipitation (Table B2), but also differences in humidity and evapotranspiration (Figure B1), with the rain forest classification associated with areas of high rainfall and humidity, whereas the dry forest areas define sub-humid areas.

A comparison of normalized channel width across different Ecozones and lithologies shows a similar trend to the aggregate dataset for small (<10 km^2) drainage areas (Figure 3.6), where reaches

underlain by granodiorite are consistently significantly wider than those underlain by volcaniclastics and serpentinites. These results suggest that the lithological differences I identified previously persist across differences in precipitation and humidity, as well as elevation. The only Ecozone where there are no significant differences between granodiorite and the volcaniclastic and serpentinite lithologies is in the rain forest, which may suggest a precipitation and/or discharge threshold for defining the influence of lithology on channel width. However, limited data of channels within the rainforest limits conclusive analysis of a precipitation threshold influence on channel width. A comparison across the Ecozones further shows that, despite differences in measured rock strength, channels underlain by volcaniclastic bedrock are not significantly different than those underlain by serpentinites. Volcaniclastics and serpentinites, however, appear to generally be associated with significantly narrower channels than those underlain by granodiorite.

3.4.4. Trends in Channel Width and Grain Size

Above, I show that bedrock lithology influences channel width, and that the influence of lithology on this channel geometry measurement is the most pronounced for rivers draining ≤6-10 km^2. In contrast to previous studies, however, I find that the weakest rock unit has the narrowest channels for a given drainage area, which generally persists across various Ecozones. Furthermore, the weaker serpentines and the stronger volcaniclastic bedrock show similar width characteristics, while the granodiorites with comparable strength to the volcaniclastic units have the widest channels for a given drainage area below ~10 km^2. As a result, bedrock channel rock strength alone does not appear to explain differences in channel width. Here, I explore other lithology-related factors that might influence bedrock channel width, namely the sediment grain size distribution.

Other studies have noted that the grain size distribution of a river's transported sediment can play an important role in bedrock channel incision and the resulting channel geometry (Turowski et al., 2015; Nativ et al., 2022). Although the explicit impact of grain size on channel width has not been resolved (Whipple, 2022), Nativ et al. (2022)'s analysis suggests that a larger proportion of large sediments (e.g.

boulders) may promote channel steepening and widening. To evaluate the possible role of grain size, I compared the median measured channel width to the grain size distributions at 18 locations throughout Puerto Rico, where both channel width measurements and pebble counts were conducted (Figure 3.1a, Table B1).

Initial results that compare the median grain size diameter (D_{50}) to channel width indicate a lack of correlation among both variables, as well as a lack of pattern between lithology and grain size (Figure B2). When comparing D_{84} grain size to the median channel width, the lack of correlation persists, yet a lithological pattern in grain size is revealed, reaches underlain by granodiorite have smaller grain sizes than reaches underlain by volcaniclastic and serpentinites (Figure 3.7c). The D_{84} grain size measurements clearly separate based on lithology, with volcaniclastics being associated with the largest grain sizes, whereas granodiorites are associated with the smallest grain sizes (Figure 3.7a). These results mirror the conclusions Pike (2008) discovered from their grain size analyses as well.

Because results from my grain size analysis are based on a small sample size (n=18), I acknowledge that the results and interpretations that stem from them are preliminary and do not provide conclusive evidence. However, assuming the differences in grain size persist among the rock types and assuming that these grain size distributions impact sediment transport and channel incision thresholds, they may help explain the differences in channel width that I observed. Recognizing that my results are preliminary, I begin to consider how bedrock lithology indirectly impacts channel width by influencing the sediment grain size.

Pulling from the concept of self-forming channels of alluvial rivers where channel hydraulics adjust to accommodate bed material entrainment, I might expect bedrock channel width to reflect the bedload grains that are transported by the river. Studying alluvial reaches, Brummer and Montgomery (2003) found that rivers with coarser sediment were associated with narrower and steeper channels. If bedrock rivers behave similar to alluvial rivers and all else (e.g. slope and discharge) is equal, it follows

that the coarser bedload in the volcaniclastic and serpentinite units would result in narrower channels than those carved out of the granodiorite units and associated with a finer grain size distributions. The basic idea is that the bedrock channels adjust their geometry to generate shear stress high enough to mobilize the bedload during typical flood conditions, albeit over longer timescales than alluvial rivers. Although more data is needed, these findings suggest that grain size properties may affect channel width.

3.4.5. Other Possible Impacts on Bedrock Channel Width

Although my dataset is limited, my preliminary results suggest that there is a rock type control on grain size that is unrelated to intact rock strength (measured with a Schmidt hammer). This finding suggests that differences in grain size based on lithology may be a consequence of other physical (e.g. fracture density and spacing) or chemical (e.g. weathering) parameters that I did not measure in this study. Previous research has found that differences and variability in fracture density and orientation may be responsible for controlling differences in the initial grain size of sediment that is added to the river by hillslope processes (Sklar et al., 2017; DiBiase et al., 2018), as well as the overall speed of erosion rates (Whipple, 2004; Molnar et al., 2007). As a result, a higher density of fractures is assumed to produce a faster-eroding rock (Becker et al., 2014; Scott and Wohl, 2019), which might also affect channel width. Our field observations found that the serpentinite units were more highly fractured than the granodiorite and volcaniclastic units, which would lead to faster eroding and wider rivers within the serpentinite units. However, our results reveal the opposite trend, with rivers underlain by serpentinites being narrower than the less fractured granodiorites, and not being significantly different than the less fractured volcaniclastics. Although this result suggests that fracture density may not play a first-order role in channel width in Puerto Rico, we recognize that we did not quantify fracture density in this analysis, and that more detailed observations are required to fully explore the impact of fracture density on channel width.

In addition, future research should further investigate the feedback between fracture density, sediment grain size, and channel width. Previous research has found that fracture density directly controls

sediment grain size, with a higher fracture density associated with enhanced vertical channel incision (Lamb and Dietrich, 2009; Neely and DiBiase, 2020). Pfeiffer et al. (2017) moreover emphasized not just the sediment distribution of the transported sediment but also the importance of linking hydraulic geometry and grain size to sediment supply. Whereas my analyses point to a lithological control on grain size, which in turn may affect channel width, more measurements are required to prove this association and improve our understanding of the nuances of how lithology affects river width.

Although many studies highlight the role that bedrock lithology and sediment grain size play in directly determining bedrock channel incision and width, others have emphasized the importance of the magnitude and frequency of the water that moves the sediment. Baynes et al. (2015) studied the exposure ages of a canyon in northeastern Iceland, which tied high-magnitude and low-frequency floods to significant bedrock incision in the canyon. Phillips and Jerolmack (2016), however, argued that moderate transport events—rather than floods—produce the most bedrock incision. Despite their contrasting conclusions, both studies emphasize how streamflow might play an important role in the timing and frequency of the 'tools' that act on the channel as to modify channel width. Although limited analysis of the recession curves of discharge records from stream gauges in Puerto Rico suggests a difference in the hydrograph (e.g. water discharge) based on rock type (Eidmann and Gallen, 2020), insight into the impact that water discharge has on bedrock channel width has yet to be explored in future analyses.

One notable component of my results is the limited impact of lithology on larger (>6-10 km^2) drainage areas. Studying five watersheds within the Luquillo Experimental Forest, Pike et al. (2010) found a similar trend at larger drainage areas. In their analysis, they attributed the lack of lithologic control at larger drainage areas to a transition to strong fluvial forces that they argued overrode boundary resistance and produced broader, basin-scale patterns (Pike et al., 2010). Another possible reason for the transition from rock-type dependent channel width to a less prominent lithological impact may be a change in proximity to landslides. Lower order streams will be more heavily affected by landsliding and the coarse grain sizes they carry with them. Studying debris flows in the tropical mountains of Brazil,

Lopes et al. (2016) found that river sediment was directly influenced by debris flows in drainage areas up to 6 km^2 in size. Considering that landslides are the primary sediment delivery mechanism to rivers in Puerto Rico (Simon et al., 1990; Larsen and Parks, 1997; Larsen and Santiago-Roman, 2001), it follows that the grains they deliver will impact lower drainage area channels (i.e. hillslope dominated regimes) more so than those at higher drainage areas (i.e. fluvial dominated regimes) (see Figure 1 of Brummer and Montgomery, 2003).

3.5 Conclusions

In my analysis, I find that bedrock plays a first-order role in dictating channel width in small (≤6 km^2) drainage areas. In contrast to conventional thinking about the influence of rock strength on channel width, I find that the narrowest channels are associated with the weakest rocks (e.g. lowest Schmidt hammer rebound measurements), and the widest channels are found in the reaches underlain by the stronger granodiorite bedrock. Although the granodiorite and volcaniclastic bedrock had similar measurements of rock strength, there appears to be a significant difference in channel width across the reaches underlain by these rock types that prevails across different Ecozones.

Although I find that the direct influence of lithology on bedrock channel width appears to become weaker as drainage area increases, grain size analyses indicate that lithology does influence the grain size distribution of sediment found in the rivers. Considering the role that sediment grain size and water discharge may have in creating self-formed bedrock channels, my analysis suggests a more nuanced influence of lithology on bedrock geometry at larger drainage areas. Future grain size analyses at both smaller and larger watersheds across different bedrock types may provide insight into the relationship between grain size, bedrock lithology, and channel width.

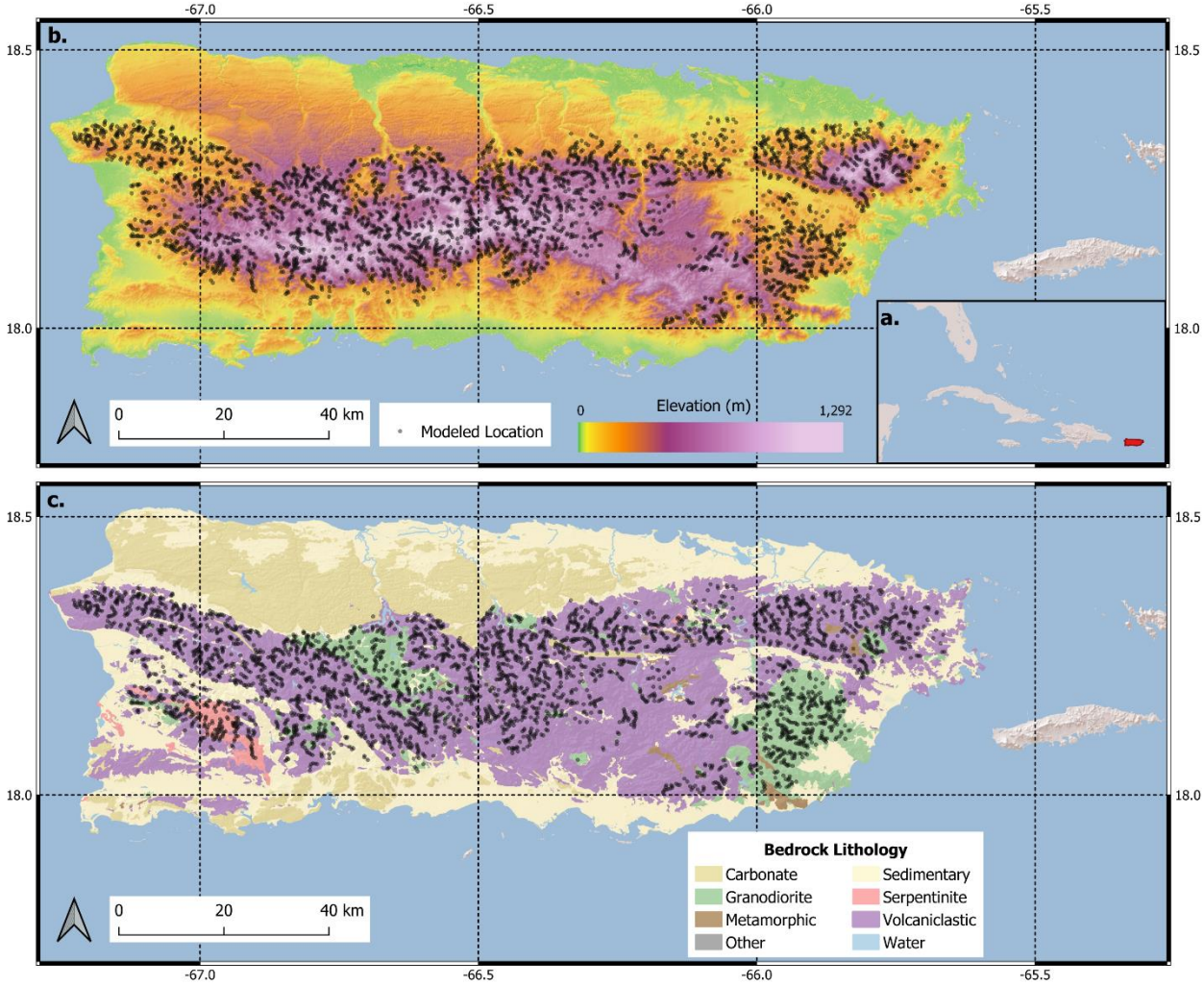

Figure 3.1. (a) a map of the Caribbean Islands and Florida, indicating in red the relative location of Puerto Rico. (b) A digital elevation model of the island shows that the topography of Puerto Rico is characterized by generally low-gradient terrain near the coast, and rugged mountainous terrain near the center. (c) The more mountainous terrain is largely comprised of Granodiorites, Volcaniclastics, and Serpentinites, whereas the low-gradient terrain is generally made up of carbonates and sedimentary bedrock. Black dots in each figure indicates the locations of modeled channel widths.

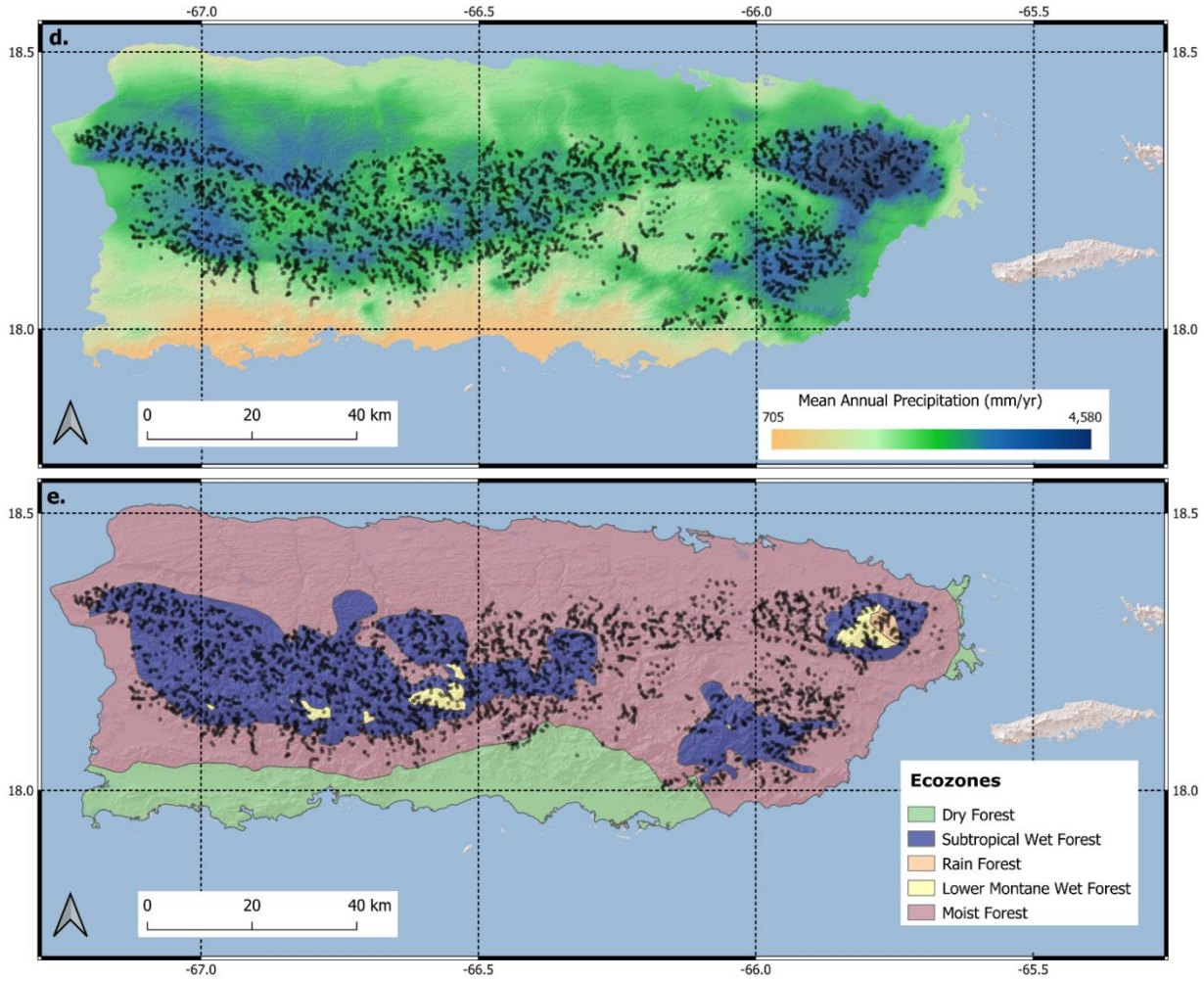

Figure 3.1(continued) (d) Precipitation across the island varies significantly, with the mountainous interior experiencing the highest rates of precipitation, whereas the southern part of the island is characterized by the driest areas. (e) Using the Mean Annual Precipitation values and gauging records from USGS gauges, we can derive the Average Specific Discharge associated with a 1-year Recurrence Interval (RI). These values can be multiplied by the upstream drainage area to estimate the 1-year RI discharge at a given location. (f) The Holdridge Ecological Lifezones (e.g. Ecozones) that make up the micro-climates found in Puerto Rico (Ewel and Whitmore, 1973). Black dots in each figure indicates the locations of modeled channel widths.

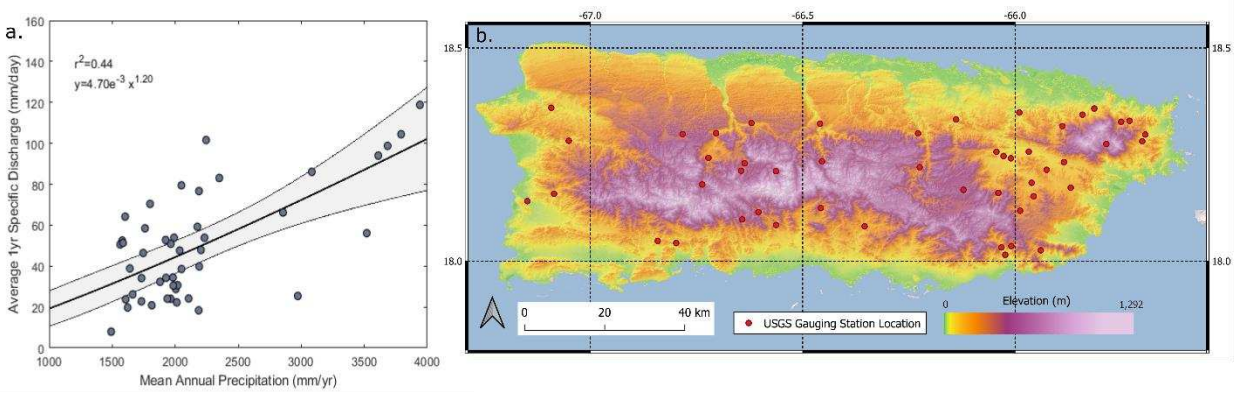

Figure 3.2. (a) Using the Mean Annual Precipitation values and gauging records from USGS gauges, we can derive the Average Specific Discharge associated with a 1-year Recurrence Interval (RI). These values can be multiplied by the upstream drainage area to estimate the 1-year RI discharge at a given location.(b) A map of the locations of USGS gauging stations used to estimate of the discharge associated with a 1-year Recurrence Interval.

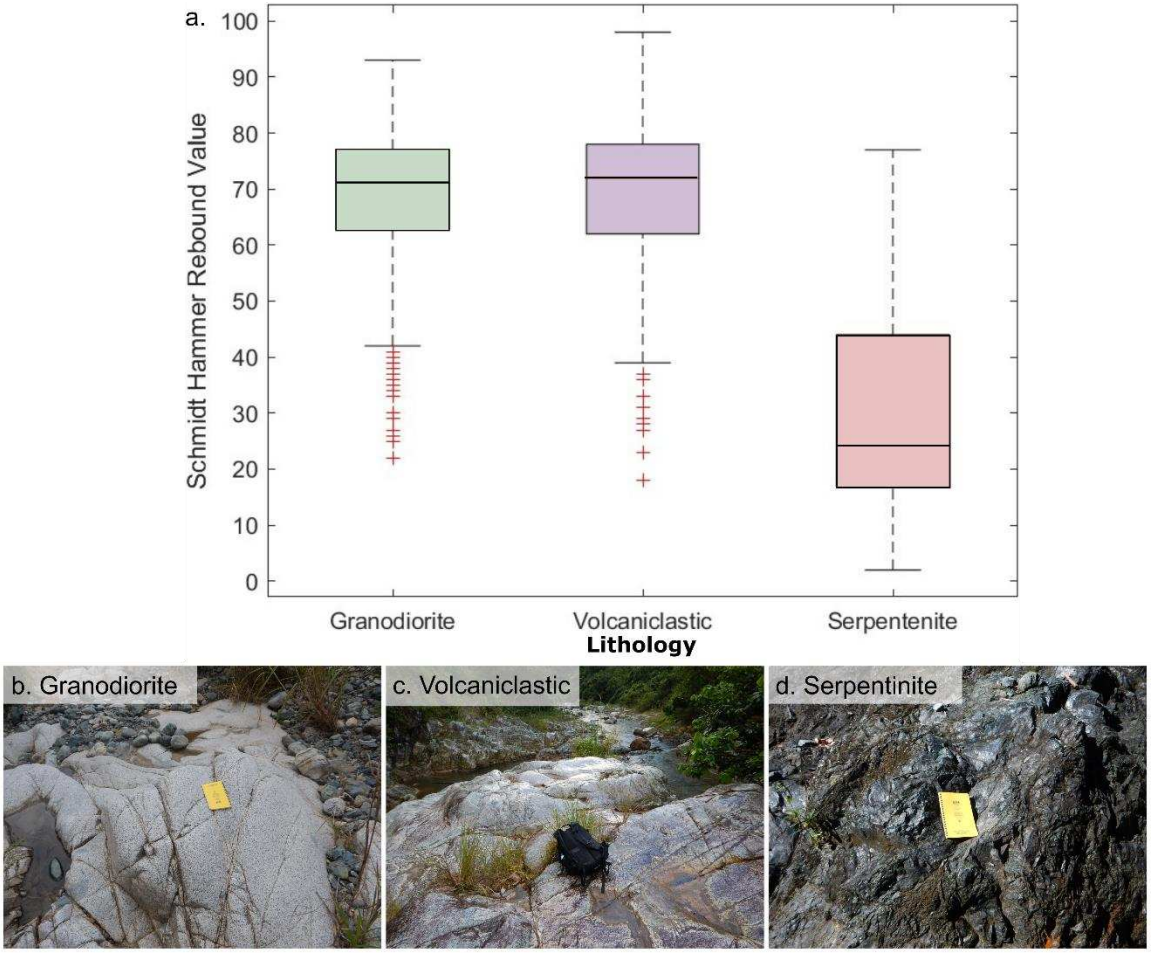

Figure 3.3 (a) A boxplot comparing the distribution of Schmidt hammer rebound values for the crystalline bedrock found in Puerto Rico. Field measurements indicate that Serpentinite is significantly weaker than Granodiorite and Volcaniclastics, whereas the similar rebound values of Granodiorites and Volcaniclastics suggest that these two rock types have a similar rock strength. (b-d) Images of the three main types of crystalline rocks analyzed in this study. (b) Granodiorites were generally light in color and often rounded through abrasion. (c) Volcaniclastics appear darker than the granodiorites, with an uneven surface, as well as many observable flutes and potholes. (d) Serpentinites are medium gray in color and show evidence of fracturing as well as rounding through abrasion.

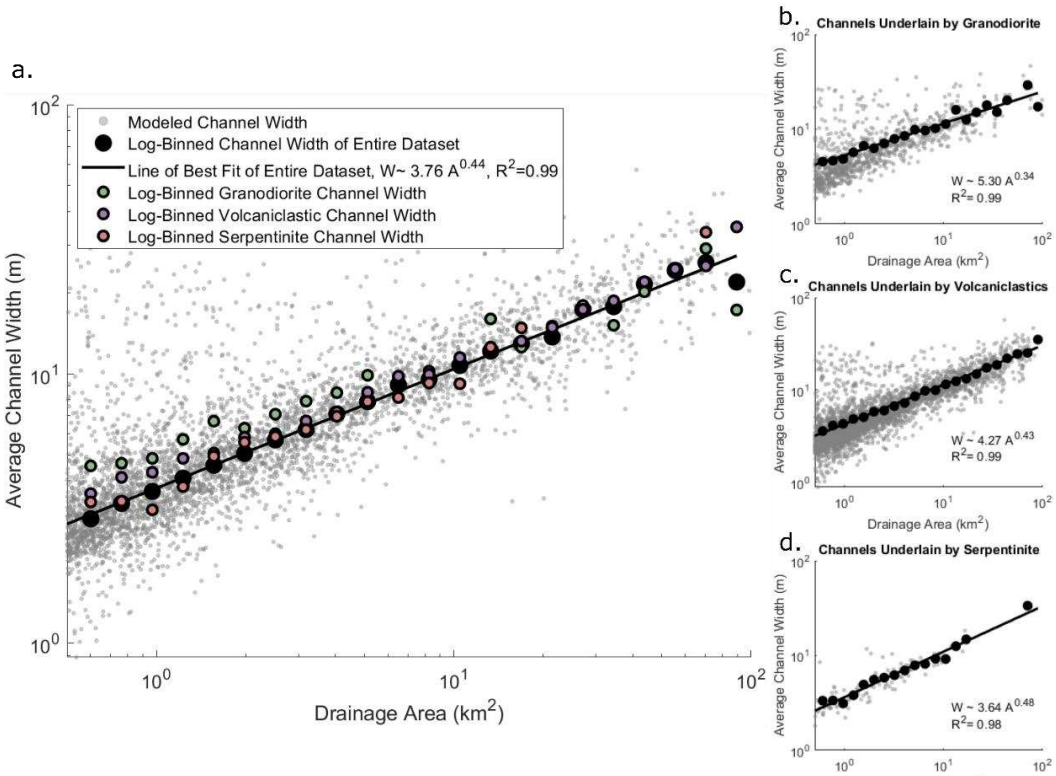

Figure 3.4. (a) A comparison of trends in channel width with drainage area. At drainage areas below 6 km^2, channels underlain by Granodiorite are systematically wider than those underlain by Volcaniclastics and Serpentinite. (b-d) A comparison of channel width to drainage area, distinguished by bedrock type. R^2 values of 0.99 reflect a high fit between the log-binned data points and the linear trendline.

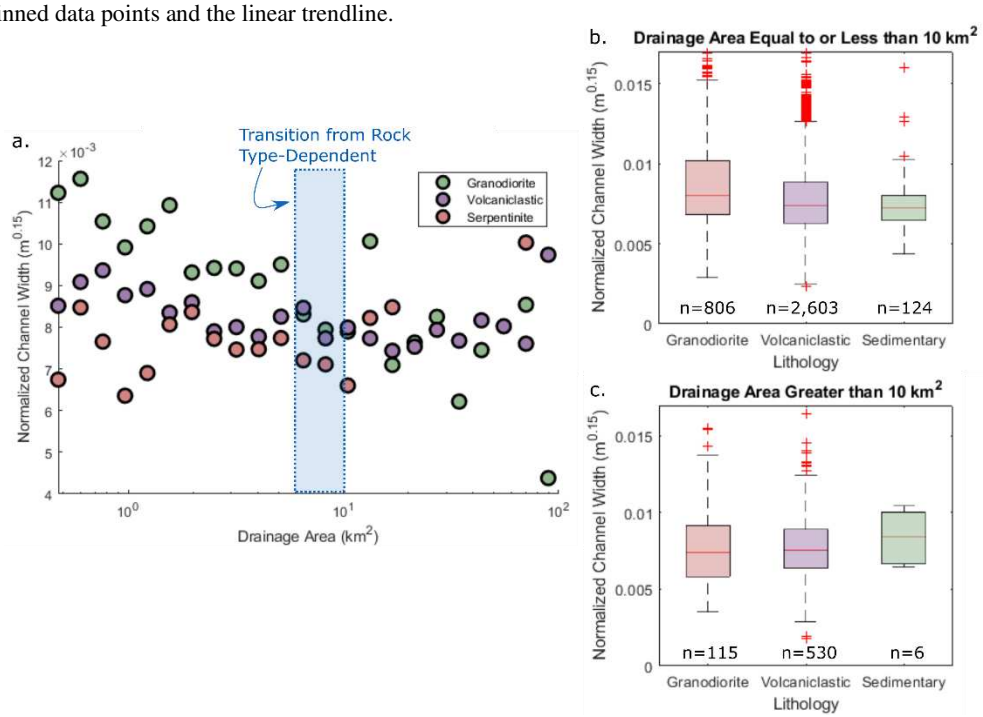

Figure 3.5. (a) A comparison between the drainage-area normalized channel width and drainage area. When channel width is normalized, channels underlain by granodiorite are still consistently wider than those underlain by serpentinites at drainage areas less than ~6-10 km^2. The normalized channel width is further compared across (b) drainage areas equal to or less than 10 km^2 and (c) drainage areas greater than 10 km^2. There does not appear to be a significant difference in normalized channel width within a lithological unit across different sizes of drainage area.

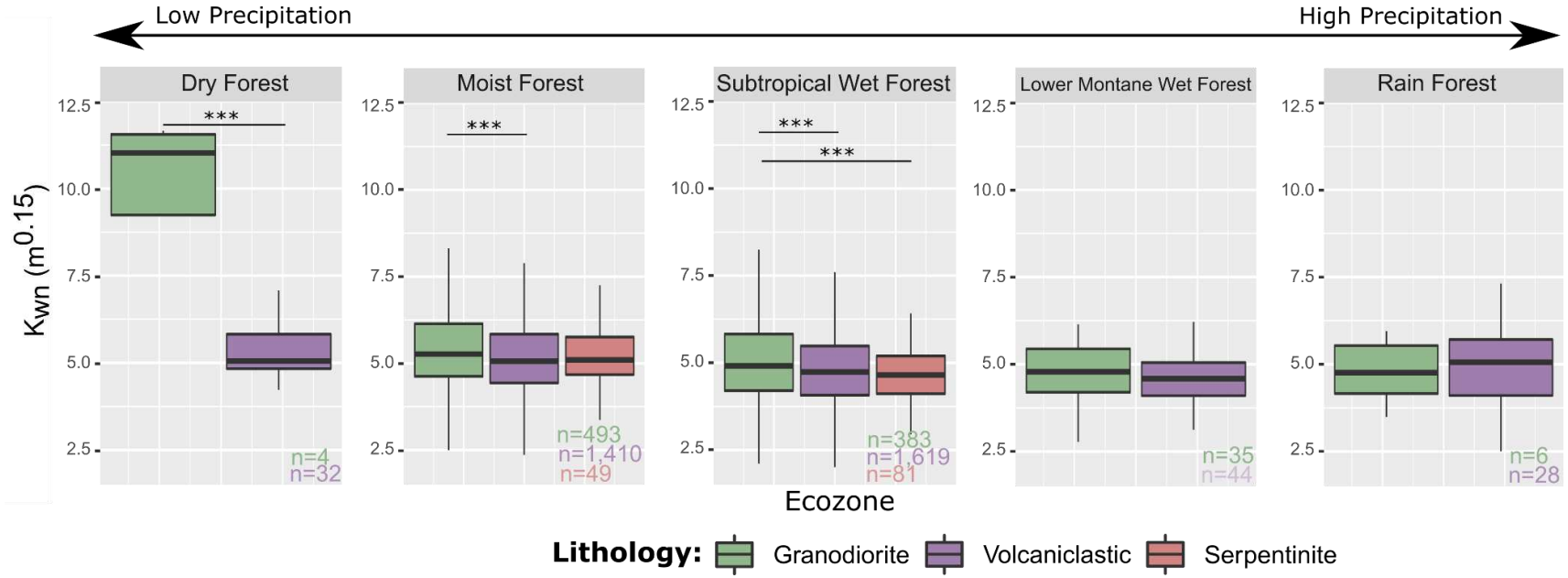

Figure 3.6. A comparison of drainage area-normalized channel width measurements across the different Ecozones in Puerto Rico. Asterisks indicate levels of significance between the population means, with * indicating a significance level of <0.05, and *** indicating a significance level of <0.001. Volcaniclastics and granodiorites appear to have significantly different channel widths across all Ecozones apart from the Rain Forest.

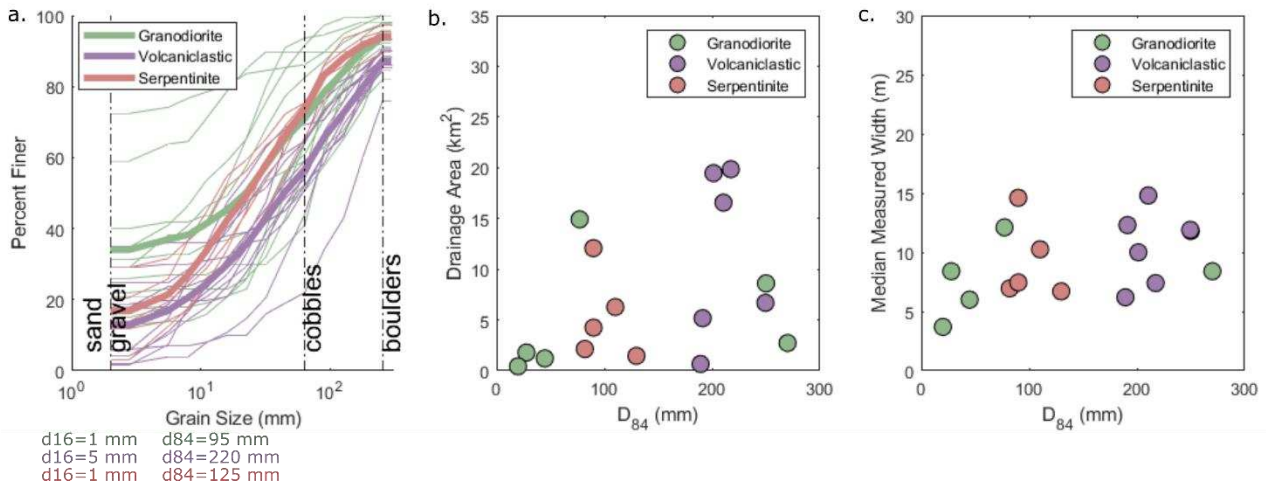

Figure 3.7. (a) A compilation of the grain size distribution according to bedrock, where thin lines represent individual sampling locations and thick lines include the entire data set for each rock type. Volcaniclastics appear to have the highest distribution of larger rocks, whereas channels that incise into granodiorite and serpentinite appear to have similar proportions of large grains. There appears to be a lack of association between grain size and both (b) drainage area and (c) measured channel width. Nevertheless, there appears to be a distinct difference between the clast sizes of the 84th percentile grain size distribution.

CHAPTER 4: NEW INSIGHTS INTO SPATIAL DIFFERENCES IN EROSION RATES AND PREDICTIVE INCISION MODELS IN PUERTO RICO, USA

4.1 Introduction

Changes in tectonic and climate conditions drive adjustments in landscape topography by changing erosion rates in space and time. In mountainous landscapes, these modifications are imposed by bedrock rivers, which process changes in uplift rates and base level elevation and transmit the signal of these changing boundary conditions throughout the landscape (Whipple and Tucker, 1999; Wobus et al., 2006). Understanding the factors that affect erosion rates governed by bedrock rivers in mountainous settings and testing existing models that predict these erosion rates is a fundamental goal of many landscape evolution studies. One technique that has been used to determine centennial-to-millennial scale erosion rates in mountainous landscapes is through dating in-situ cosmogenic nuclides of sediments found in bedrock rivers.

The application of in-situ cosmogenic nuclides to determine erosion rates is built on the premise that cosmic rays from the sun bombard the Earth's surface, which interact with particles in the atmosphere and surface materials to produce cosmogenic nuclides. With knowledge of the production rate (modulated by latitude and erosion), attenuation length scales in earth materials and half-life of a given nuclide, I can use the concentration of a nuclide to derive the exposure age or the denudation rate of a given sample; the surface concentration being inversely proportional to the erosion rate (Granger et al., 2014; von Blanckenburg and Willenbring, 2014; Schaefer et al., 2022). In river systems with minimal storage and geologically rapid sediment transport times, such as in mountainous settings, and assuming a well-mixed sample that evenly reflects hillslope denudation of the upstream catchment, analysis of nuclide concentrations in river sediments can thus provide insight into the catchment-average erosion rate of a watershed (Bierman and Steig, 1996; Granger et al., 1996).

In this study, I compile existing- and generate new in-situ cosmogenic nuclide-derived basin average erosion rate in the subtropical island of Puerto Rico in fluvially-dominated bedrock catchments to explore spatial patterns of erosion and lithologic, climatic and topographic controls on erosion and test the ability of several commonly used river incision models to predict these erosion rates. Located at the boundary between the North American and Caribbean plates, Puerto Rico is tectonically active and has a diverse suite of basement rock types and climates. Several studies using cosmogenic nuclides have been published in Puerto Rico (Brown et al., 1995; Riebe et al., 2003; Brocard et al., 2015). Although these analyses have produced several erosion rates (n=16 samples), most of the samples are spatially limited to the El Yunque National Forest of the Luquillo Mountains (Figure 4.1). In addition, these studies all use ^{10}Be in-situ cosmogenic nuclide to derive catchment-average erosion rates, which limits sampling locations to areas underlain by quartz-rich granodiorites and prohibits analysis of areas with lithologies devoid of sufficient concentrations of quartz. It follows that spatial variations in erosion rates across Puerto Rico remain largely unknown, and that data is limited to erosion rates of only the granodiorites found on the island. With these limitations, an understanding of what controls erosion rates in Puerto Rico remains largely unknown.

Bedrock river incision models are often used to better understand and reconstruct topographic change and relate them to tectonic and climate signals. Although several mathematical river incision models exist, the detachment-limited stream-power incision model is the most frequently used method to approximate river incision (Whipple and Tucker, 1999; DiBiase and Whipple, 2011; Perron and Royden, 2012; Lague, 2014). This model calculates incision, I, as:

$$I = KA^m S^n \qquad \text{(Eq. 4.1)},$$

where K is erodibility, A is upstream contributing drainage area (a proxy for river discharge, Q), S is the slope, and m and n are empirically-derived exponents where m/n falls near 0.5 ($0.35 \leq m/n \leq 0.60$) (Howard and Kerby, 1983; Whipple and Tucker, 1999).

The detachment-limited stream-power incision model is widely used across landscape evolution analyses, as it is grounded on simplicity—requiring three input parameters (*K, m,* and *n*)—and incorporates simple geometric constraints (e.g. drainage area and slope) that are easily obtained from Digital Elevation Models (DEMs). Whereas the simplicity of the model is a quality that led to its widespread application, this aspect of the model also becomes its largest weakness. A breadth of studies have shown that incision rates are determined by an interplay of multiple dynamic processes, and is sensitive to variations in factors such as channel geometry, sediment supply, grain size, sediment flux, threshold effects, and discharge dynamics (Lavé and Avouac, 2001; Finnegan et al., 2007; Turowski et al., 2008; Lague, 2014). These factors, moreover, can vary both in time (e.g. stochasticity of floods and mass wasting events across thousands of years) and space (e.g. differences in river roughness and lithology). Because it is difficult to capture this variability through two geometric constraints (drainage area and slope), two empirical exponents (*m* and *n*), and one erodibility value (*K*), the predictive capabilities of this model are not necessarily universally suited for analysis across all fluvially-dominated bedrock landscapes (Lague, 2014). As a result, many have suggested the use of more complex versions of the detachment-limited stream-power incision model that include many of the dynamics named above (e.g. grain size, sediment supply, channel geometry, weathering, stochasticity of extreme floods) (Benda and Dune, 1997; Whittaker et al., 2007; Attal et al., 2011; DiBiase and Whipple, 2011; Lague, 2014). From this discussion stems the questions: is the basic stream power incision model too simple; does added complexity improve incision rate predictions at a landscape scale, or does it unnecessarily overparameterize the relationship between channel attributes and catchment incision rates?

In this paper, I conduct analysis of in-situ terrestrial cosmogenic nuclides (^{10}Be in quartz and ^{36}Cl in magnetite) from Puerto Rico to expand spatial coverage of basin average erosion rates in fluvially-dominated bedrock catchments on the island. With these data I (1) evaluate spatial patterns of potential controls (e.g. lithology, precipitation, and topography) on erosion to better understand what drives erosion in Puerto Rico, and (2) test four versions of varying degrees of complexity of the stream power incision

model to explore whether more complex models produce better estimates of incision rates. Although I compare model results to cosmogenic nuclide concentrations, it should be noted that these results are similar but can be fundamentally different, as the model predicts bedrock incision, whereas the cosmogenic concentrations measure hillslope denudation rates. In this analysis, we, therefore, assume that bedrock incision is directly coupled with hillslope erosion.

4.2. Setting

I chose to perform this analysis in Puerto Rico—an island ~9,000 km^2 in area that is located in the Caribbean, approximately 1,700 km southeast of Miami, Florida (Figure 4.1a). Puerto Rico is characterized by a notable variety in landscape topography; its northern landscape is composed of carbonates (Oligocene to early Pliocene in age) that form a karst topography (Moussa et al., 1987; Schellekens, 1998), whereas both deformed and undeformed plutonic rocks (mainly volcaniclastic and granodiorite rocks Cretaceous to Paleocene and early Eocene in age) make up the steep mountains found in the central and northeastern parts of the island (U.S. Geological Survey, 1960) (Figure 4.1). Sedimentary rocks (Miocene to Quaternary in age) comprise the low-relief and low-elevation southern areas of the island (Volckmann, 1984). In addition, due to its location along the North American and Caribbean plate boundary, Puerto Rico has a tectonically active geologic history. Most recently, it is thought that Puerto Rico experienced a pulse of uplift ~4-5 million years ago (Brocard et al., 2015). As a result, the landscape reflects a state of dynamic equilibrium, with areas of low-relief relict surfaces (incised prior to the latest pulse of uplift) and areas that have been actively incised within the past 4-5 million years (Brocard et al., 2015).

The mild, subtropical climate in Puerto Rico is defined by annual ‘dry’ and ‘wet’ seasons that occur from December to March and April to November, respectively (Murphy et al., 2017). In addition, precipitation across the island is closely tied to topography: the high-elevation mountainous regions generally receive the highest annual rates of precipitation (up to over 4,000 mm/year), whereas the low-lying southern portion of the island tends to be driest (NOAA, 2011). Despite these topographic

differences in precipitation, northeast trade winds, tropical depressions, storms, and hurricanes determine the overall precipitation patterns at a larger, island-wide scale (Ehlmann, 1968; Calvesbert, 1970).

4.2.1. Existing Cosmogenic Nuclide Catchment Average Erosion Rate Studies

In this paper, I use cosmogenic nuclides to estimate catchment average erosion rates. Prior to my study, numerous other research efforts (e.g. Brown et al., 1995; Riebe et al., 2003; Brocard et al., 2015) provided ^{10}Be concentrations from catchments mostly located in the El Yunque National Forest of the Luquillo Mountains (Figure 4.1). In their analyses, Brown et al. (1995) highlighted differences in cosmogenic nuclide concentrations associated with different grain sizes, finding that results from large (>2 mm) grain sizes reflected erosion rates from landslide material, whereas results from the fine (<2mm) sediment fractions expressed long-term erosion rates (further supported through work by Belmont et al., 2007). With this in mind, I compiled 16 existing ^{10}Be cosmogenic nuclide concentrations derived from the sand-size fraction (<2 mm grain size diameter) of fluvial sand samples and recalculated basin average erosion rates to standardize calculations across these studies (see detailed methods below) (Brown et al., 1995; Riebe et al., 2003; Brocard et al., 2015). Because these existing samples are largely spatially limited to the northeastern mountainous portion of the island that is underlain by granodiorite bedrock (rich in ^{10}Be-bearing quartz), in this analysis, I seek to expand our understanding of erosion rates both spatially and lithologically. To achieve this goal, I analyzed 23 additional samples (at a grain size of 250-710 μm) obtained in both the central and western portions of Puerto Rico and collected from both granodiorite- and volcaniclastic-draining river catchments. Although the quartz-rich samples obtained from granodiorite catchments enabled me to perform ^{10}Be analysis on most (n=21) samples, I turned towards ^{36}Cl analysis of magnetite to derive catchment average erosion rates of samples (n=2) predominantly draining volcaniclastic bedrock (Bierman and Steig, 1996; Moore and Granger, 2019).

4.3 Methods

4.3.1 Empirically Calibrating the Model

4.3.1.1. An Evaluation of Detachment-limited Bedrock Incision Rate Models of Various Complexities

In this analysis, I seek to compare and evaluate the effectiveness of four stream-power bedrock incision models—each of which presents a variation in the detail and complexity of the basic model (Eq. 4.1). The first model (*Model 1*) incorporates Flint's Law (Flint, 1974), which states that local channel slope scales with drainage area:

$$S = k_{sn}A^{-\theta} \qquad \text{(Eq. 4.2)},$$

where k_{sn} is the channel steepness index, A is the upstream contributing drainage area, and Θ is the channel concavity index (equivalent to m/n in Eq. 4.1). Rearranging Eq. 4.2 to solve for k_{sn} as a function of slope and area and assuming the concavity index equals the ratio of m to n, my first model uses channel steepness and erodibility to estimate incision:

$$I = K\ {k_{sn}}^{n} \qquad \text{(Eq. 4.3; } \textit{Model 1}\text{)}$$

Whereas the channel steepness index (k_{sn}) is typically derived by normalizing slope by the drainage area (Eq. 4.2), channel steepness can also be expressed as a function of stream discharge, often assumed to be approximated by upstream drainage area weighted by the distribution of mean annual precipitation (e.g. Pederson and Tressler, 2012; Yang et al., 2015; Adams et al., 2020). *Model 2* is a variant of *Model 1*, but uses a discharge-normalized steepness index (k_{snq}) rather than the traditional drainage area-normalized version of this metric given by Eq. 4.2.

In *Model 1,* the shear stress imposed on the bed is estimated through the channel steepness index, k_{sn}. As a result, the simplified model assumes that channel steepness and shear stress are both directly proportional to the incision rate. Others (e.g. Tomkin et al., 2003; Lague et al., 2005; Gallen and Fernandez-Blanco, 2021; Turowski, 2021), however, have noted that the shear stress imposed on the bed is better parametrized by directly including measurements of channel geometry and basin characteristics. Chaplin (2005) found that discharge scaled with drainage area, and (Whipple et al., 2013) demonstrated

that drainage area also scales with river width. As a result, an alternate method of estimating incision would be to include drainage area rather than discharge:

$$I = K_w\left(\left(\frac{A}{w}\right)^{\frac{\alpha}{\beta}} S\right)^{n_w} \qquad \text{(Eq. 4.4; } \textit{Model 3}\text{)}.$$

Lague et al. (2005) suggested a similar model, but included characteristics of river discharge—rather than drainage area—into the landscape evolution model:

$$I = K_w\left(\left(\frac{Q}{w}\right)^{\frac{\alpha}{\beta}} S\right)^{n_w} \qquad \text{(Eq. 4.5; } \textit{Model 4}\text{)},$$

where K_w is the long-term efficiency coefficient, Q is discharge, w is channel flow width, α and β are hydraulic friction law parameters, and n_w is the slope exponent (typically estimated to be about 0.7) (Lague et al., 2005). Assuming a Darcy-Weisbach relation α and β are both 2/3, and the ratio of these two parameters is typically assumed to be ~1 (Howard et al., 1994; DiBiase and Whipple, 2011).

4.3.1.2. Discharge Estimation

Because discharge measurements are not available in the areas of interest, I use the Mean Annual Precipitation (MAP) (PRISM Climate Group, 2022) as a proxy for estimating discharge in the models (Allen et al., 2013, Chapter 2). Previous analysis in Puerto Rico that compares the MAP-based estimates of mean annual discharge (MAQ) to that of existing USGS gauging stations reveals a power-law scaling relationship between precipitation and measured discharge values. The high r^2 value (r^2=0.82) of this relationship demonstrates that such MAP-based estimates are a good proxy for mean annual discharge at ungauged locations (Figure 4.2).

4.3.1.3. Channel Width Measurements

Although all models may produce theoretically valid approximations of incision rates, Whipple et al. (2022) highlighted a need for such models to be tested through new data and observations. In addition,

model performance can be altered not only by the addition or omission of specific variables, but is also dependent on the quality of the data that is incorporated into the variables. In this analysis, I use a channel width estimate of W ~3.76$A^{0.44}$—a model width estimate based on an analysis of 4,184 modeled channel widths (Chapter 3) derived from a new automated approach (Chapter 2). Once this data is incorporated, I test how well these four models predict erosion rates by comparing the model outputs to measured basin-average erosion rates (derived from cosmogenic ^{10}Be and ^{36}Cl concentrations in river sediments) in Puerto Rico.

4.3.1.4. Calculating Model Parameters

Parameters included in the tested models include an erodibility constant (*K*), the channel steepness index (k_{sn}), and *n*. To perform model calculations, I first evaluated the concavity index (*m/n*) by minimizing the variance of elevation values (acquired from the DEM) along the stream network. Through this method I achieved a concavity index (or *m/n* value) of 0.46, which is close to the typically used value of 0.45 (Wobus et al., 2006; Kirby and Whipple, 2012), which I use in all subsequent analyses. Using this value, I calculated χ, which integrates the inverse of drainage area over a stream-wise distance:

$$\chi = \int_{x_b}^{x'} \left(\frac{A_o}{A(x)}\right)^{-m/n} dx \qquad \text{(Eq. 4.6)},$$

where x_b and x' are distance at an arbitrary based level and at the channel head, respectively, A_o is the reference drainage area, here taken as 1 m^2, $A(x)$ is the drainage area at a given stream position, and *m* and *n* are the same exponents as in Eq. 4.1. Through transforming the stream distance by calculating χ, I am then able to obtain channel steepness index values by regression of elevation versus χ data from the river network (Perron and Royden, 2012). Similarly, I can calculate k_{snq} by calculating χ_q, which is similar to above but done by integrating the inverse of my discharge proxy rather than drainage area.

In *Model 1*, I calculated k_{sn} by first deriving elevation and χ values within a given window size (in my case a window size of 500 m), and performing a linear regression of these data. The *Model 2* k_{snq} was calculated similar to k_{sn} for *Model 1,* but instead of using the drainage area, I used a precipitation-

weighted drainage area (obtained from the MAP raster) (PRISM Climate Group, 2022). In *Model 3*, $\left(\frac{A}{w}\right)^{\frac{\alpha}{\beta}} S$ represents a width-normalized channel steepness value. To calculate this value, I extracted upstream drainage area and the smoothed river elevations using a 500 m moving window average before calculating local slope. I calculated width using the method detailed above (see Section 4.2.3). For *Model 4*, I performed the same width-normalized steepness calculations used in *Model 3*, but replaced drainage area with the precipitation-weighted drainage area discharge proxy, Q. Once these parameters were obtained for each method, I performed a power-law regression between the channel steepness value and measured erosion rates to obtain values for erodibility (K) and n values associated with each model.

4.3.2. Measuring Cosmogenic Nuclide Catchment Average Erosion Rates

For this analysis, I sought to expand upon the existing cosmogenic nuclide data set to obtain a better understanding of how erosion rates change both spatially across the island and across differences in lithology. Because the in-situ cosmogenic nuclides are derived from quartz grains, existing measurements are lithologically confined to the granodiorite bedrock that covers only ~10% of the island (Figure 4.1). In this analysis, re-analyze existing ^{10}Be concentrations from the literature along with 23 new samples presented in this study. I obtain additional erosion rates using two methods, 1) through the ^{10}Be cosmogenic nuclides found in the quartz grains of the granodiorite bedrock, and 2) through the ^{36}Cl concentrations found in the magnetite minerals of the volcaniclastic units (Moore and Granger, 2019). By using both dating methods, I am able to extend our understanding of erosion rates both spatially across the island, and also to the volcaniclastic rocks that comprise a significant (~40%) portion of Puerto Rico's land area (Figure 4.1).

To obtain samples for cosmogenic nuclide analysis, I sieved (250-710 micron grain size) and collected approximately 0.5 kg of sand at each sampling location (Figure 4.1). For this research, 8 samples (KSH-01 to KSH-08) were collected by K. Stephen Hughes, and both processed and analyzed by the Purdue Rare Isotope Measurement (PRIME) laboratory, 12 samples (PR-05, PR-14, PR-16, PR-18,

PR-19, PR-23, PR-25, PR-27, PR-29, PR30, PR-37, and PR-39) were processed at CSU and the University of Vermont (UVM) and analyzed at PRIME, and 5 samples (PR-21, PR-23, PR-31, PR-39, and PR-42) were processed at the PRIME laboratory for ^{36}Cl. All samples were first dried in the oven, and a Frantz Isodynamic Laboratory Separator was used to split magnetic grains from non-magnetic grains. For samples analyzed for ^{36}Cl, the magnetic grains were then sent to the Purdue cosmogenic lab for processing and analysis. For samples analyzed for ^{10}Be, the non-magnetic grains were used.

Sample preparation of the magnetic grains to be analyzed for ^{36}Cl followed the process outlined by Moore and Granger (2019). Magnetite is extracted from the aggregate sand using a magnet. A known mass of ^{35}Cl is initially added to the magnetite separate for each sample, which is then dissolved in oxalic acid. As a next step, HNO_3 and $AgNO_3$ are added to the solution to form a precipitate of AgCl. Once centrifuged and separated, AgCl is dried, placed into a cathode, and measured by the Accelerator Mass Spectrometer (AMS) at the Purdue Rare Isotope Measurement Laboratory (PRIME).

The non-magnetic samples to be analyzed for Be^{10} underwent a series of purification steps to incrementally separate quartz grains from other lithologies. To remove any non-quartz grains from the samples, each sample underwent two rounds of 6N HCl etches, three rounds of HF/HNO_3 etches, and a final cleansing etch of HF/HNO_3 (see Kohl and Nishiizumi (1992) for more details on the sample preparation process). Following the purification process, samples were sent to the University of Vermont Cosmogenic Laboratory to extract ^{10}Be.

Once samples were designated to have sufficient pure quartz grains for analysis, each sample underwent a series of procedures at the University of Vermont Comogenic Laboratory to extract Be and Al from purified quartz. In this process, the initial sample mass was measured, and a known mass of Be^9 was added to each sample. Next, the samples were digested into a liquid over four days using HF, and then divided into two aliquots—one (termed *Subsample 1*) that would be processed to verify that the samples are not contaminated (i.e. that the quartz samples don't contain more Be^9 than was originally added, which is a verification needed to quantify the accuracy of the Be^{10}/Be^9 ratio), and another (termed

Subsample 2) used to measure the concentration of Be^{10}. H_2SO_4 was added to *Subsample 1* to avoid drying off the sample, then spiked with Ga/Y, and analyzed in the Inductively coupled plasma mass spectrometer (ICP-MS). *Subsample 2* underwent four perchloric treatments and three $HClO_4$ treatments to eliminate fluoride compounds. As a next step, a series of hydrochloric acid treatments followed by a centrifuging to redissolve the sample, off-gas hydrogen, and remove titanium from the sample. Samples then were processed in column tubes to remove iron from the solution, and chemically separate the samples into titanium, beryllium, and aluminum concentrations. To purify the remaining beryllium, the tubes containing beryllium concentrations were then further processed in a series of precipitation and dissolution steps, and finally turned into a gel substance. This gel was then processed into a pellet, which was converted to BeO using an air gas flame mixed with Nb, which was then further packed into cathodes that were sent to PRIME for beryllium analysis measured by the AMS.

AMS measurements of ^{10}Be were normalized to Nishiizumi et al. (2007) standard ratio of $^{10}Be/^{9}Be$, whereas measurements of ^{36}Cl were normalized against Sharma et al. (1990) standard ratio of ^{36}Cl/Total Cl. These normalized measurements were used to calculate erosion rates based on equations from Brown et al. (1995). To calculate local ^{10}Be production, the sea level high-latitude (SLHL) ^{10}Be production of nucleons and slow and fast muons were scaled based on Stone (2000). I use the nucleonic SLHL production rate of 3.9 ± 0.1 at g^{-1} yr^{-1} from Balco et al. (2009), and I use Braucher et al. (2011)'s production rates for the slow and fast muonic components. As part of this analysis, I assumed a rock density of 2.7 g/cm^3 and attenuation lengths for neutrons and slow and fast muons from Braucher et al. (2011). No topographic shielding correction was calculated for the basin average erosion rates following DiBiase (2018). From this analysis, I derived catchment average erosion rates (mm/yr) at each sampling location.

4.4. Results

4.4.1. Measured Bedrock Erosion Rates Across Puerto Rico

Existing ^{10}Be measurements in Puerto Rico are largely spatially limited to the Luquillo Mountains located in the northeastern portion of the island, with a few measurements in a granodiorite pluton to the south of the Luquillo Mountains (Figure 4.1; Brown et al., 1995; Riebe et al., 2003; Brocard et al., 2015). My new measurements expand this spatial coverage westward (Figure 4.1). An assessment of the existing and new data in the sand size fraction shows that erosion rates vary by nearly an order of magnitude, ranging from a rate of 8.5 m/My to 97.1 m/My (Figure 4.3; Table 4.1). When analyzed spatially, the results generally show that erosion rates on the central-western portion of the island are faster than those in the east (Figure 4.3).

In Chapter 3, I used a Schmidt hammer to obtain rebound measurements—a proxy for rock strength—in the field. From these data, I found that granodiorite bedrock and volcaniclastic bedrock were not significantly different in rock strength (Figure 4.4a). Cosmogenic erosion rate results, however, show a significant difference between erosion rates across bedrock lithology, with areas draining granodiorite watersheds associated with a much lower erosion rate than those draining volcaniclastic watersheds (Figure 4.4b). Similarly, I find that k_{sn} values systematically differ across rock types, with locations sampled within watersheds underlain by granodiorite being significantly shallower (median k_{sn} value of 19) than those underlain by volcaniclasitcs (median k_{sn} value of 58). These results suggest that, even though erosion rates may initially appear to be associated with differences in lithology, when differences in topography (e.g. channel steepness) are considered, the control of rock type on erosion rate becomes less clear. In other words, it appears that differences in landscape steepness correlate with lithology and might be able to explain the variations in erosion rate alone.

Lastly, I compare trends in erosion based on both rock type and precipitation (Figure 4.5). Results indicate a lack of correlation between precipitation, with both high and low erosion rates found in areas of relatively high and low precipitation (Figure 4.5). This lack of correlation is further shown by the very low R^2 values when samples are subset by rock type—granodiorite and volcaniclastic samples are associated with an R^2 value of 0.08 and 0.06, respectively.

4.4.2. Models of Bedrock Erosion Rates

Through a power-law fit of my erosion rate results and topographic derivatives (i.e. k_{sn}, k_{snq}, $(A/w)^{\alpha/\beta}S$, and $(Q/w)^{\alpha/\beta}S$), I empirically derived model parameter values (e.g., K and n) (see Figure 4.6 for the regressions and model parameter values). The data were relatively scattered, producing weak-to-moderate model fits to the data. The R^2 values range between 0.15 and 0.35 (Figure 4.6).

Applying the empirically-derived parameter values for each model with channel and basin geometry measurements (e.g. channel width, estimated discharge, slope, and drainage basin area), I then calculated modeled erosion rates using Eq. 4.3-4.5. As a final step, I compared modeled erosion rates to measured erosion rates (Figure 4.7). Results indicate that measured and modeled erosion rates show a positive trend, but the strength of the correlation, however, is relatively weak to moderate (with R^2 values between 0.16 and 0.35). From this analysis, I determined that *Model 3* (the more complex model that utilizes drainage area and width) was associated with the best fit (R^2=0.35) and lowest residual error of 0.0290, followed closely by *Model 1* (the simpler model that utilizes drainage area) that had the same fit value and a slightly higher residual error of 0.0292. Whereas *Models 1* and *3* differ in complexity, the nearly equivalent residual error (a difference of 0.0002 in residual error, corresponding to a difference of 0.2 m/My incision rate estimate) shows that model complexity does not appear to have a significant difference in the modeled incision rates.

4.5. Discussion

4.5.1. Measured Bedrock Erosion Rates Across Puerto Rico

A spatial analysis of variations in erosion rates shows that granodiorites in the central part of the island generally have much higher erosion rates than that of granodiorites towards the east. Whereas initial analysis may suggest a lithological control on erosion rates (Figure 4.4b), I find that higher erosion rates are also associated with steeper channels, and that the volcaniclastics sampled in this analysis were generally characterized by steeper watersheds (Figure 4.4c). As a result, the impacts of lithology versus channel steepness on erosion becomes difficult to disentangle due to the covariation with topography for the sampled drainage basins. Previous research has found a positive correlation between erosion rates and

k_{sn} (Safran et al., 2005; Wobus et al., 2006; Ouimet et al., 2009), suggesting that erosion rates are likely dependent on topography rather than rock type. To verify this conclusion, however, I would need to compare samples from different lithologies but comparable values of channel steepness.

Climatic differences, namely in precipitation, are another possible reason for differences in erosion rate. Studying the San Gabriel Mountains, DiBiase and Whipple (2011), found that the discharge distribution played a large role in the relationship between channel steepness and the erosion rate. It follows that differences in precipitation—and the resulting discharges in Puerto Rico, may thereby influence this relationship and the resulting erosion rates, and explain the observed spatial changes in erosion (Figure 4.3). To test this idea, I compared erosion rates by precipitation (Figure 4.5). In this comparison, I found that nearly the entire range of erosion rates measured was found in basins that were characterized by both high and lower levels of precipitation (Figure 4.5). Moreover, I find no lithological differences across both discharge and erosion rates. These findings suggest that rock type and precipitation don't correlate well with incision, and that the influence of topography—namely channel steepness—may be a dominant factor in determining erosion rates. To disentangle the impact of precipitation and rock type further, more samples that differ by rock type but have similar topographic characteristics (i.e. steepness) need to be collected and compared, highlighting future data needs. In addition, repeat sampling at more locations can further improve measurement uncertainties (e.g. bias due to proximity to a recent landslide or due to an uneven distribution of sediment that represents only a portion, rather than an average, of the catchment area (Grande et al., 2021).

In Luquillo, spatial variations in erosion rates have been attributed to active landscape adjustment to a change in tectonic rock uplift rate that occurred ~4-5 Myr ago that is still affecting parts of the Puerto Rican landscape today (Brocard et al., 2015). Brocard et al. (2015) found that erosion rates above fluvial knickpoints thought to have been formed as a result of this pulse of uplift are lower than erosion rates below them. The spatial pattern of the existing and new erosion rates and the channel steepness – erosion rate trends presented here support this conclusion (Figures 4.3 and 4.6a). Temporal variations in erosion

rate have been documented in the landscape above knickpoints that are associated with local landslides (Grande et al., 2021); however, this variation only affects low drainage areas (<6 km^2), and the system recovers to a stable background concentration within a year after a landslide event. Therefore, I do not think that intermittent landsliding can explain the variations seen in my data.

Lastly, my analysis extends a spatial understanding of changes in erosion rates across the island. Previous analyses have largely only covered areas within the Luquillo National Forest, in addition to one sample from the dryer southeastern portion of the island underlain by granodiorite (Brown et al., 1995). From these analyses, I find that erosion rates in the central part of the islands are much higher than those previously published towards the eastern part of Puerto Rico. This result suggests that there are differences in the local base level lowering rate among these different locations, perhaps related to different rates of tectonically-driven rock uplift.

4.5.2. Models of Bedrock Erosion Rates

In this research, I compare incision rates derived from four detachment-limited stream power equations that vary in both complexity and modeling parameters. In *Models 1* and *3, I* apply drainage area as a proxy for shear stress or stream power, whereas in *Models 2* and *4 I* apply a precipitation-based discharge value as a proxy for shear stress or stream power. By comparing modeled results with laboratory-measured erosion rates results, I find that *Models 1* and *3* better predict actual erosion rates better than *Models 2* and *4* (Figure 4.7). These results suggest that in Puerto Rico, drainage area appears to be a better predictor of incision rates than the weighted discharge proxy (Figures 4.6 and 4.7). As discussed in *Section 4.4.1*, there appears to be minimal association between erosion rates and precipitation (Figure 4.5) it follows that adding a precipitation-weighted drainage area parameter does not improve model performance—something that is shown in the erosion models as well.

In addition, I find that an increase in model complexity only slightly improves model performance (e.g. *Model 3* had a residual error only 0.002 mm/yr lower than *Model 1*). One of the largest differences between these two models is the incorporation of channel width. In the model, however,

channel width is largely compared as a ratio to drainage area—a much larger value. It follows that whereas incorporating channel width does appear to improve model performance, the relatively low impact of comparing drainage area (a large number) to channel width (a small number typically <10 m in Puerto Rico, as found by modeled channel measurements in Chapter 3) only has a minimal effect on model performance. With this in mind, I conclude that when modeling landscape erosion in Puerto Rico, only using DEM-derived input parameters is sufficient to produce a rough estimate of catchment-area erosion rates, but that there is still a great deal of scatter in the modeled and predicted estimates (e.g. *Model 1*) (Figure 4.7).

The finding that the simplest model does a reasonable job fitting the data, and that none of the models fit the data very well is an important finding in its own right. The reasonably good performance of *Model 1* suggests that erosion rates in Puerto Rico are largely controlled by variations in topography (i.e., steepness), which perhaps isn't too surprising. While my limited dataset did not clearly indicate that lithology, precipitation, and channel width are not first-order factors controlling erosion patterns in Puerto Rico, they may play an important role in explaining the scatter in the data. For example, my treatment of all of these variables is quite simple; I look for correlations among the variables and erosion. Lithology might play a role by impacting grain size distributions and thus incision thresholds in ways that spatially vary in ways unaccounted for here (e.g. Neely and DiBiase, 2020). Precipitation alone does not affect river incision, but it is how it gets translated into floods, and the frequency and magnitude of flood distributions are ultimately what controls bedrock river incision rates (e.g. Lague, 2014). My treatment of channel width here is based on a simple scaling relationship, but incorporating measured spatial variations in this hydraulic parameter might result in an improved fit to the data. Finally, it is possible that the scatter in the data is the result of comparing basin average erosion rates to models that predict basin average incision rates. In circumstances where the channels and hillslopes are not fully coupled, there can be discrepancies between erosion and incision rates. Regardless, the moderate positive trends of *Models 1* and *3* give confidence that these simple models yield some predictive behavior of the system albeit

imprefectly. I note that assessing all of these possibilities for model fit quality is beyond the scope of this particular study, but they highlight clear and likely fruitful future research directions.

4.6. Conclusions

In this study, I analyzed 23 cosmogenic nuclide samples, substantially increasing the spatial understanding of erosion rates across Puerto Rico. My analyses indicate spatial differences in erosion rates, with the dryer southeastern portion of Puerto Rico generally having slower erosion rates than the wetter mountainous central-western portion of the island. In addition, samples located in the very wet mountainous region of the Luquillo National Forest had variable erosion rates, which are a result of samples collected above- and below- the relict landscape topography (Brocard et al., 2015). Analysis of cosmogenic ^{36}Cl in magnetite in addition to ^{10}Be analysis in quartz, allows me to compare erosion rates across the granodiorite and voclaniclastic bedrock lithologies that comprise the mountainous interior of Puerto Rico. Although initial analyses appear to suggest that rock type plays a role in determining erosion rates, sampled granodiorite basins have systematically gentler topography than volcaniclastics making it difficult to isolate a lithologic control if one exists. When controlling for differences in steepness, the influence of rock type becomes less clear. Additional analysis of samples derived from different rock types but similar topography is required to disentangle this relationship.

Our research indicates that the simple stream-power incision model generally predicts trends in incision rates across Puerto Rico. Residual errors from the models demonstrate that drainage area appears to be a better predictor of incision rates than discharge (expressed through a precipitation-weighted drainage area parameter). *Models 1* and *3* varied in model complexity—with Model 3 incorporating channel geometry measurements such as channel width—but had very similar residual errors. This indicates that in Puerto Rico, an increasing model complexity has minimal impact on model performance and variables derived from DEMs are adequate for predicting landscape incision rates. Although *Models 1* and *3* performed best, a moderate R^2 value of 0.35 indicates that I am not fully explaining trends in erosion rates, and are likely missing other important variables in the model. Characteristics that may

improve model performance may be an incorporation of rock type, an improvement of an incorporation of channel width into the model, and/or a parameterization that takes into account channel and hillslope coupling relationships.

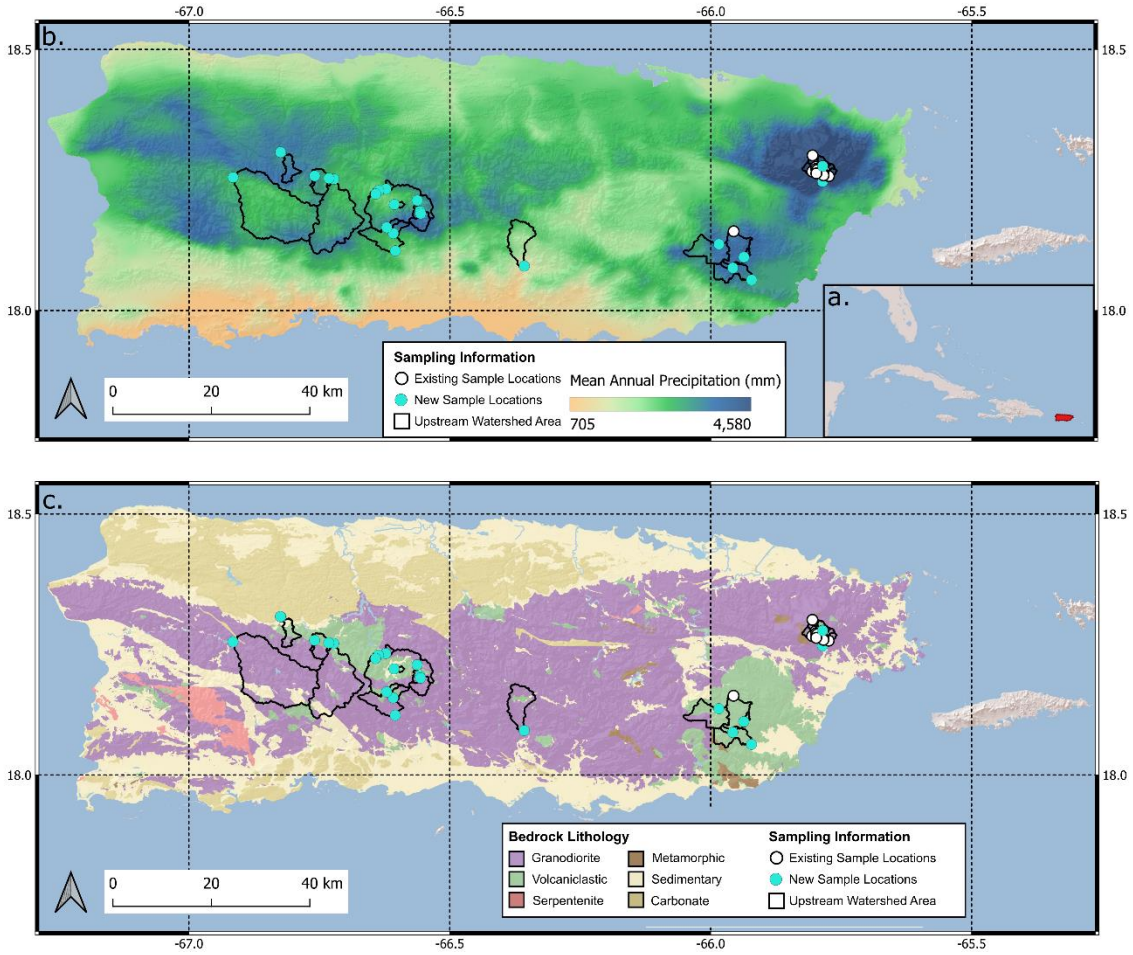

Figure 4.1. A map of Puerto Rico showing (a) its location relative to other islands in the Caribbean. The locations of existing and new samples in relation to (b) precipitation and (c) bedrock lithology. The new sampling locations significantly enhance the spatial coverage of erosion rates across the island.

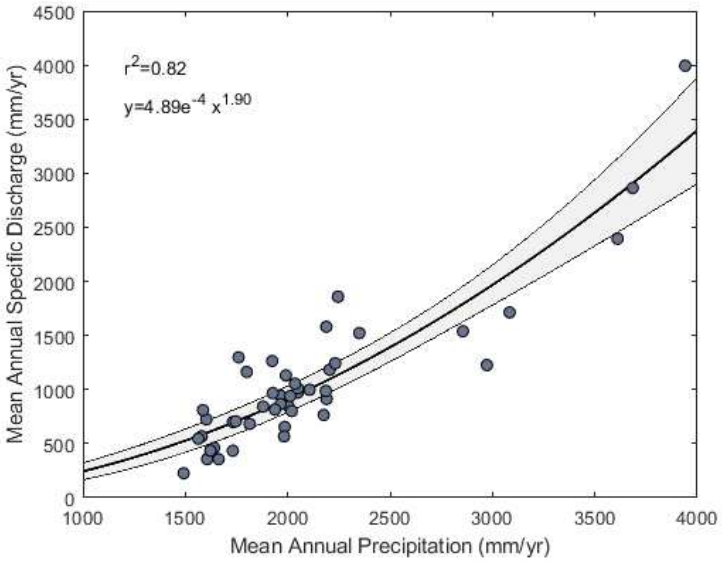

Figure 4.2. A comparison of the Mean Annual Precipitation in relation to the Average Specific Discharge across the 49 gauging stations in Puerto Rico. The shaded area represents the 95% confidence interval.

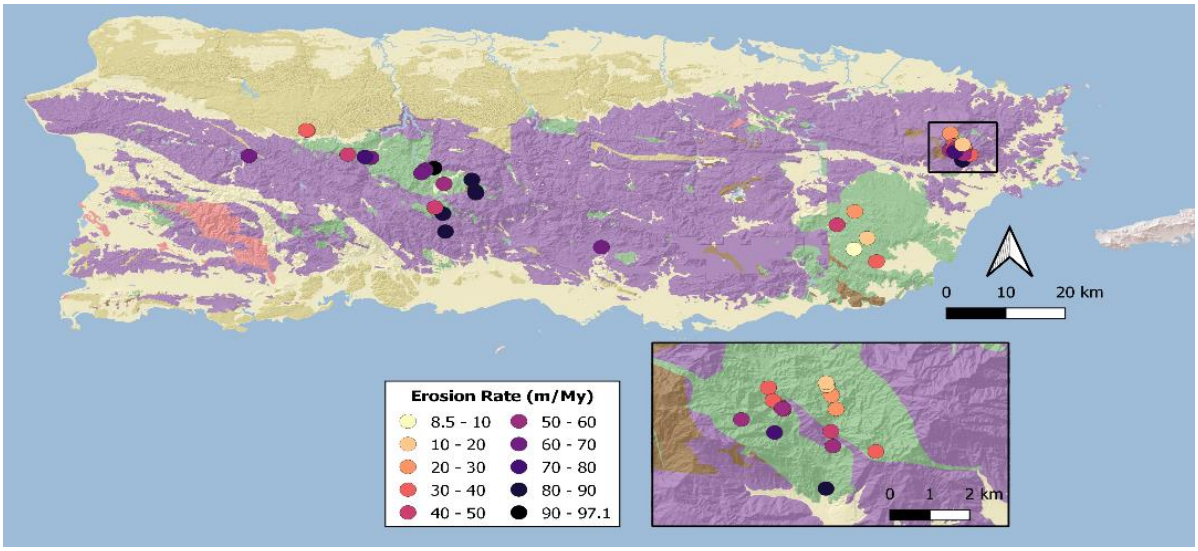

Figure 4.3. A geologic map of Puerto Rico overlain by the cosmogenic nuclide sample locations. Colors at each sample locations reflect the measured erosion rates at each location.

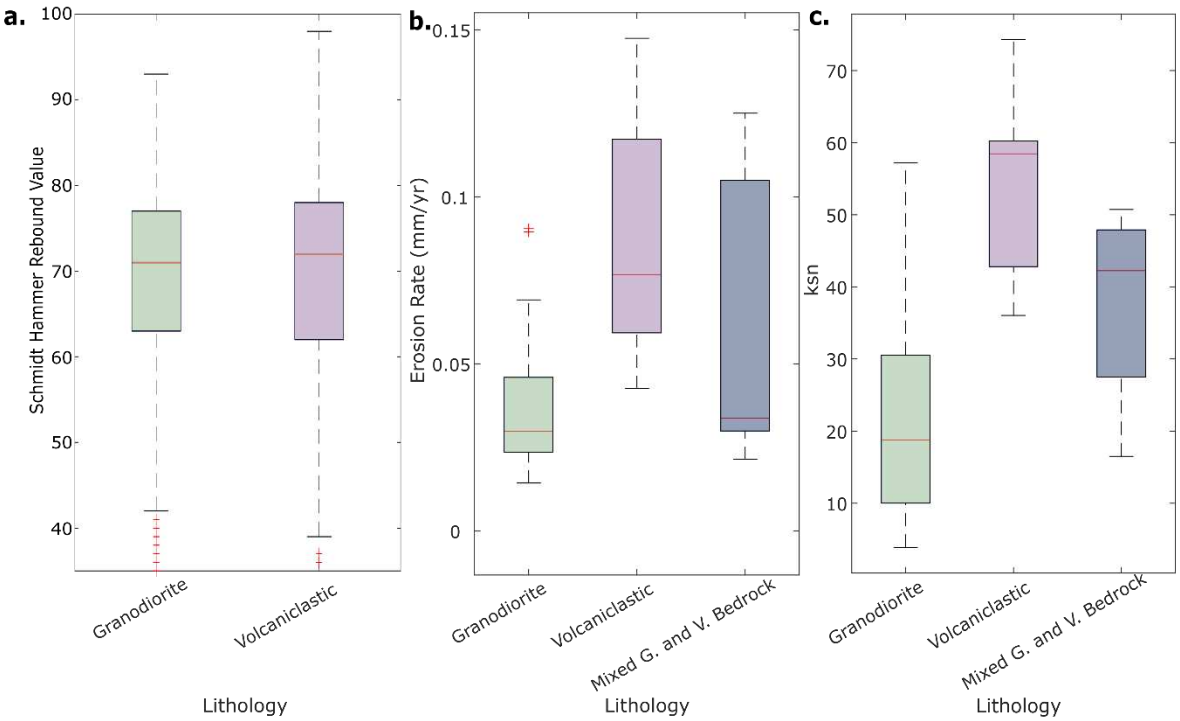

Figure 4.4. (a) A comparison of Schmidt Hammer Rebound values, which reflect the rock strength of both Granodiorite and Volcaniclastic lithological units. Results show comparable rock strength values across both bedrock types. (b) Cosmogenic nuclide erosion rate values indicate that areas draining Granodiorite bedrock are associated with a lower basin-average erosion rates than areas draining Volcaniclastic bedrock. (c) Channel steepness index values (k_{sn}) according to lithology show that sample locations of granodiorites are located in shallower topography than volcaniclastics.

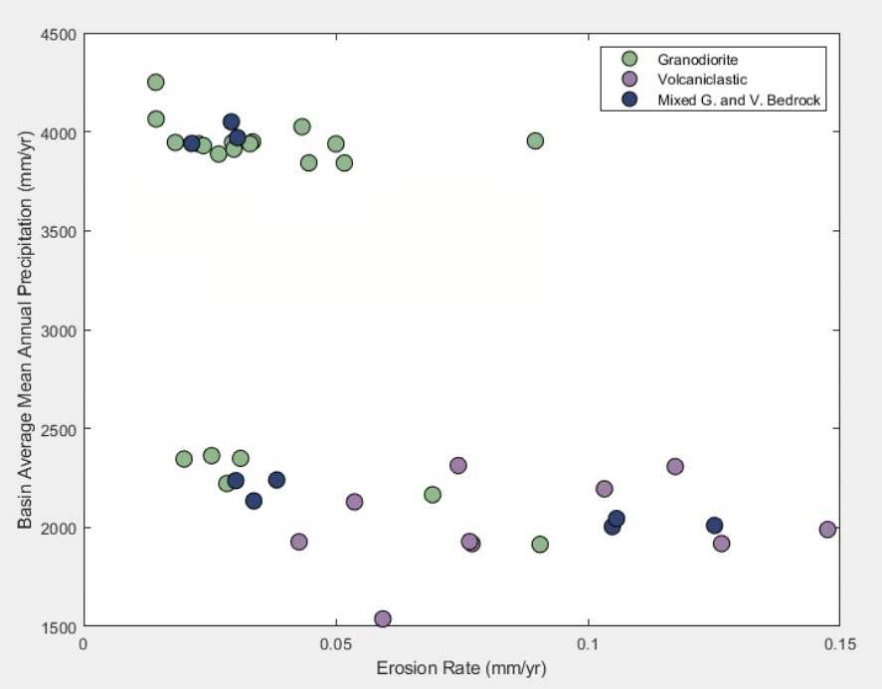

Figure 4.5. A comparison of changes in erosion rate with precipitation, colored by bedrock. This indicates a lack of correlation between precipitation and erosion rates across analyzed bedrock units.

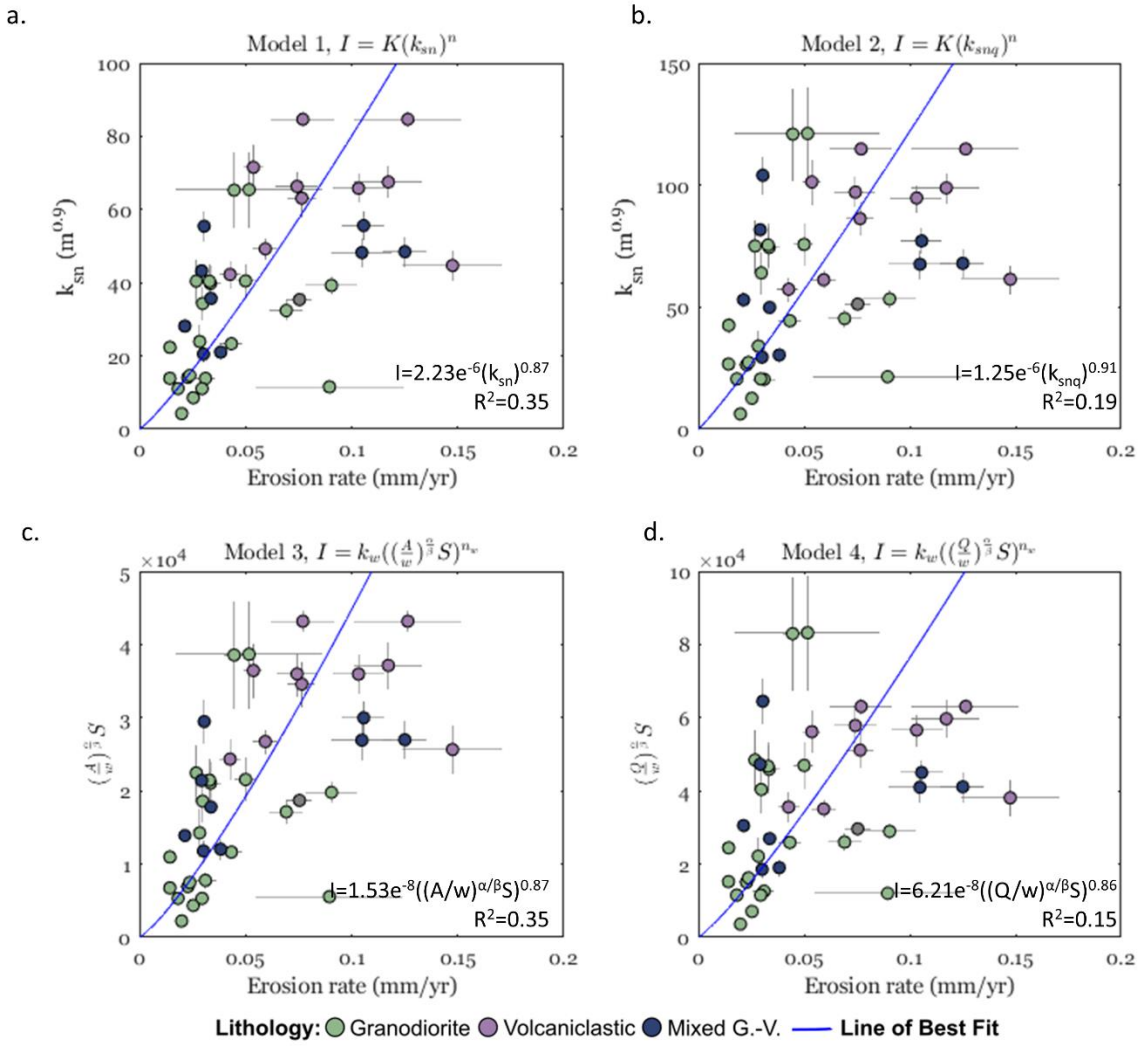

Figure 4.6. (a-d) To model erosion rates across Puerto Rico, we first calibrated the model parameters by regressing the erosion rate by the channel steepness index (k_{sn}).

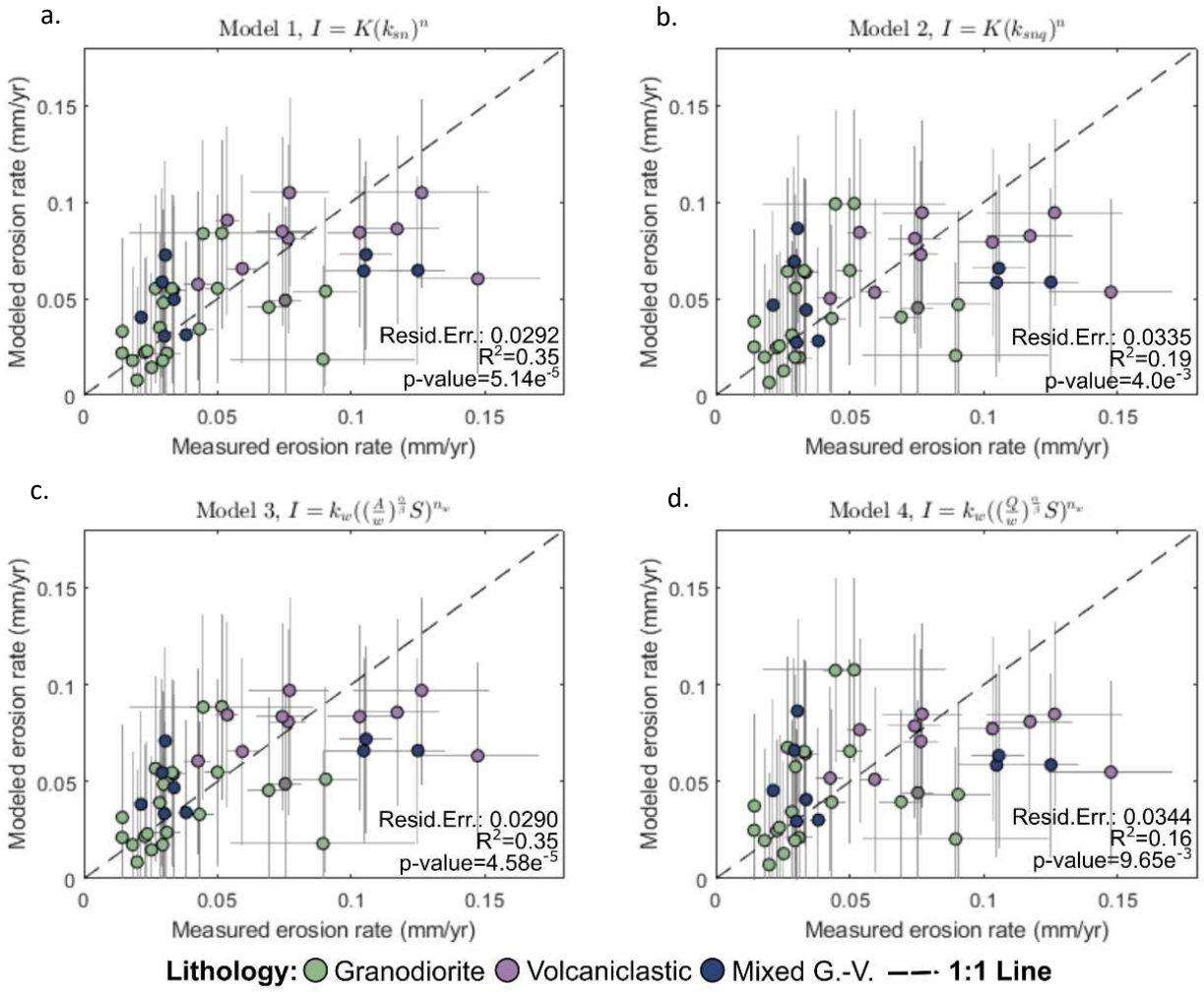

Figure 4.7. (a-d) A comparison of modeled erosion rates to erosion rates derived from cosmogenic Be^{10} and Cl^{36} concentration measurements. Models 1 and 4 are associated with the lowest residual errors, indicating the best model performances for estimating erosion rate

Table 4.1. A compilation of in-situ cosmogenic nuclide results of samples analyzed for ^{10}Be and ^{36}Cl.

ID	UTM (X)	UTM (Y)	^{10}Be (10^4 atoms/g)	Denudation rate (mm/year)
PR-05	740803.2483	2019545.386	22170 ± 3065	0.14752 ± 0.02322
PR-14	758383.2482	2012915.386	35580 ± 4039	0.11730 ± 0.01593
PR-16	757783.2482	2015225.386	37490 ± 3488	0.10326 ± 0.01218
PR-18	753133.2482	2014325.386	34590 ± 3963	0.09050 ± 0.01230
PR-19	749923.2482	2017205.386	32590 ± 3824	0.10483 ± 0.01452
PR-23	751393.2482	2017565.386	42740 ± 7369	0.07701 ± 0.01487
PR-25	825883.2477	1999385.386	89230 ± 5949	0.02841 ± 0.00280
PR-27	822043.2477	2001875.386	123700 ± 7080	0.01992 ± 0.00187
PR-29	824233.2477	2004185.386	99470 ± 5548	0.02537 ± 0.00232
PR-30	819133.2477	2006855.386	40100 ± 3620	0.06919 ± 0.00793
PR-37	720373.2483	2019665.386	72320 ± 6604	0.04272 ± 0.00503
PR-39	839953.2475	2020505.386	71770 ± 5474	0.04465 ± 0.00471
KSH-01	753493.2482	2004485.386	42342 ± 2255	0.07653 ± 0.00671
KSH-02	753013.2482	2008175.386	67819 ± 2814	0.05371 ± 0.00445
KSH-03	751663.2482	2009435.386	51923 ± 1805	0.07541 ± 0.00597
KSH-04	749353.2482	2016485.386	27521 ± 1316	0.12509 ± 0.01048
KSH-05	739813.2483	2019695.386	28657 ± 1853	0.10567 ± 0.00994
KSH-06	736933.2483	2020175.386	91736 ± 2045	0.03375 ± 0.00252
KSH-07	730063.2483	2025065.386	73934 ± 3270	0.03829 ± 0.00319
KSH-08	729943.2483	2025125.386	92019 ± 3550	0.03018 ± 0.00245
Brown-GUA	840043.2475	2023385.386	138000 ± 14000	0.02281 ± 0.00295
Brown-CAY	822073.2477	2009645.386	80300 ± 11400	0.03113 ± 0.00515
Riebe-RI-8	838843.2475	2022935.386	66000 ± 4000	0.05003 ± 0.00469
Riebe-RI-6	839923.2475	2023715.386	108000 ± 6000	0.02954 ± 0.00272
Brocard-ES-UK	837793.2475	2026025.386	225100 ± 2900	0.01432 ± 0.00110
Brocard-IC-UK	839923.2475	2023685.386	170500 ± 5500	0.01821 ± 0.00148
Brocard-SAB-UK	838453.2475	2023595.386	221000 ± 14000	0.01438 ± 0.00145
Brocard-CUY-UK	837793.2475	2022605.386	115200 ± 7800	0.02929 ± 0.00296
Brocard-PRI-UK	841183.2475	2021675.386	152000 ± 10000	0.02143 ± 0.00216
Brocard-SAB-TDK1	838783.2475	2023025.386	97200 ± 12500	0.03349 ± 0.00510
Brocard-SAB-TDK2	838573.2475	2023205.386	77300 ± 7700	0.04332 ± 0.00542
Brocard-SAB-TDK3	838813.2475	2022965.386	98300 ± 8300	0.03300 ± 0.00373
Brocard-IC-TDK1	840163.2475	2022965.386	132700 ± 3800	0.02375 ± 0.00187
Brocard-IC-TDK2	840043.2475	2022275.386	107200 ± 3600	0.02980 ± 0.00238

Brocard-IC-TDK3	840103.2475	2021825.386	118000 ± 3000	0.02678 ± 0.00206
Brocard-CUY-TDK	838633.2475	2022215.386	108800 ± 5200	0.03052 ± 0.00267
ID	**UTM (X)**	**UTM (Y)**	**^{36}Cl (10^5 atoms/g)**	**Denudation rate (mm/yr)**
PR-21	758504.5697	2012471.043	30642 + 3935	0.07428 + 0.01094 - 0.008454
PR-23	751393.2482	2017565.386	8824 ± 1697	0.12648 + 0.03012 - 0.020403
PR-31	779683.5867	2001621.545	27507 ± 2562	0.05933 + 0.00609 - 0.005056
PR-39	839953.2475	2020505.386	17469 ± 8718	0.05169 + 0.05149 - 0.017208
PR-42	839899.8385	2023780.274	10181 ± 3484	0.08955 + 0.04659 - 0.022833

CHAPTER 5: CONCLUSION

5.1 Key Findings

Throughout this dissertation, I explore different ways to improve our knowledge of landscape evolution. Bedrock channel width plays a first-order role in many landscape evolution models, yet a scarcity of bedrock channel width data often causes researchers to use a drainage area:width or discharge: width scaling relationship to estimate bedrock width. To improve the calibration of this parameter, I developed a method in Chapter 2 to remotely extract channel width through the paired use of a Digital Elevation Model in Topotoolbox with the HEC-RAS river analysis software. I verified this method using both USGS field measurements as well as field measurements that I collected in the field.

In Chapter 3, I implemented the methods of Chapter 2 to explore what factors control bedrock channel width. My analyses of ~4,000 river reaches in Puerto Rico reveal a first-order lithologic control at small (< 6-10 km^2) catchment areas, but show that a direct control by bedrock is less obvious at larger drainage areas. Although grain size analyses hit at a potential indirect control of rock type through lithological differences in sediment grain size, more sample locations are required to draw further conclusions.

In Chapter 4, I analyzed in-situ cosmogenic nuclide concentrations to find spatial differences in erosion rates across Puerto Rico. These differences appear to be mostly related to differences in channel steepness, and are not as clearly influenced by rock type or precipitation. To definitively tease these variables apart, however, I cite the need to collect samples of different bedrock types but at similar channel steepness values. Lastly, I applied the measured erosion rate results to evaluate bedrock incision models of various complexity. My results revealed that drainage area is a better predictor of incision rates than a precipitation-weighted drainage area parameter. The close performance between *Models 1 and Models 3* suggest that an increase in model complexity has minimal improvements on model

performance. The moderate R^2 value of 0.35 of the best performing model indicates that even the more complex model is missing parameters and information that better explain erosion rates in Puerto Rico.

5.2 Opportunities for Future Research

I hope that this research provides methods and ideas that will promote more research into what shapes bedrock rivers, which in turn will help advance the fields of tectonic geomorphology and landscape evolution. From this research, in Chapter 2, I developed a method of efficiently extracting channel width using DEMs produced from high-resolution (~1 m) LiDAR. With the development of the 3DEP program across the United States that will make high-resolution DEMs of the entire United States freely accessible to the public, this method can help extract bedrock channel width measurements across the entire United States. This additional data can thus help us form a better understanding of what factors control channel geometry. In Chapter 3, grain size analyses suggest a lithological difference in the coarse grain size fraction of river sediments. These differences in grain size may help explain observed differences in channel width found in the different rock types in Puerto Rico. However, further grain size and field measurements are required to fully explore this trend. Lastly, in Chapter 4, I found that erosion rates in Puerto Rico appear to be associated with river channel steepness. There does appear to be an association between erosion rate and rock type, yet the impact of rock type cannot be disentangled from channel steepness, as samples from each rock type have systematically different channel steepness as well. To distinguish between the role that channel steepness and rock type have in erosion rates, future sampling locations must cover areas of similar steepness values and different rock types.

BIBLIOGRAPHY

Adams, B.A., Whipple, K.X., Forte, A.M., Heimsath, A.M., and Hodges, K. V., 2020, Climate controls on erosion in tectonically active landscapes: Science Advances, v. 6.

Allen, G.H., Barnes, J.B., Pavelsky, T.M., and Kirby, E., 2013, Lithologic and tectonic controls on bedrock channel form at the northwest Himalayan front: Journal of Geophysical Research: Earth Surface, v. 118, p. 1806–1825, doi:10.1002/JGRF.20113.

Allen, G.H., and Pavelsky, T.M., 2018, Global extent of rivers and streams: Science, v. 361, p. 1–3.

Amos, C.B., and Burbank, D.W., 2007, Channel width response to differential uplift: Journal of Geophysical Research: Earth Surface, v. 112, p. 2010, doi:10.1029/2006JF000672.

Attal, M., Cowie, P.A., Whittaker, A.C., Hobley, D., Tucker, G.E., and Roberts, G.P., 2011, Testing fluvial erosion models using the transient response of bedrock rivers to tectonic forcing in the Apennines, Italy: Journal of Geophysical Research, v. 116, doi:10.1029/2010JF001875.

Balco, G., Briner, J., Finkel, R.C., Rayburn, J.A., Ridge, J.C., and Schaefer, J.M., 2009, Regional beryllium-10 production rate calibration for late-glacial northeastern North America: Quaternary Geochronology, v. 4.

Baynes, E.R.C., Attal, M., Niedermann, S., Kirstein, L.A., Dugmore, A.J., and Naylor, M., 2015, Erosion during extreme flood events dominates holocene canyon evolution in northeast iceland: Proceedings of the National Academy of Sciences of the United States of America, v. 112, p. 2355–2360, doi:10.1073/PNAS.1415443112/-/DCSUPPLEMENTAL.

Baynes, E.R.C., Lague, D., Steer, P., Bonnet, S., and Illien, L., 2020, Sediment flux-driven channel geometry adjustment of bedrock and mixed gravel–bedrock rivers: Earth Surface Processes and

Landforms, v. 45, p. 3714–3731, doi:10.1002/ESP.4996.

Becker, R.A., Tikoff, B., Riley, P.R., and R., I.N., 2014, Preexisting fractures and the formation of an iconic American landscape: Tuolumne Meadows, Yosemite National Park, USA: GSA Today, v. 24, p. 4–10, doi:10.1130/GSATG203A.1.

Belmont, P., Pazzaglia, F.J., and Gosse, J.C., 2007, Cosmogenic 10Be as a tracer for hillslope channel sediment dynamics in the Clearwater River, western Washington State: Earth and Planetary Science Letters, v. 264, p. 123–135.

Benda, L., and Dune, T., 1997, Stochastic forcing of sediment supply to channel networks from landsliding and debris flow: Water Resources Research, v. 33, p. 2849–2863.

Bierman, P., and Steig, E., 1996, Estimating Rates of Denudation Using Cosmogenic Isotope Abundances In Sediment: Earth Surface Processes and Landforms, v. 21, p. 125–139, doi:10.1002/(SICI)1096-9837(199602)21:2<125::AID-ESP511>3.0.CO;2-8.

von Blanckenburg, F., and Willenbring, J.K., 2014, Cosmogenic nuclides: Dates and rates of Earth-surface change: Elements, v. 10, p. 341–346.

Braucher, R., Merchel, S., Borgomano, J., and Bourle, D.L., 2011, Production of cosmogenic radionuclides at great depth: a multi element approach: Earth and Planetary Science Letters2, v. 309, p. 1–9.

Brocard, G.Y., Willenbring, J.K., Scatena, F., and Johnson, A.H., 2015, Effects of a tectonically-triggered wave of incision on Riverine Exports and Soil Mineralogy in the Luquillo Mountains of Puerto Rico: Journal of Applied Geochemistry, v. 63, p. 586–598, doi:10.1017/CBO9781107415324.004.

Brown, E.T., Stallard, R.F., Larsen, M.C., Raisbeck, G.M., and Yiou, F., 1995, Denudation rates determined from the accumulation of in situ-produced 10Be in the luquillo experimental forest, Puerto Rico: Earth and Planetary Science Letters, v. 129, p. 193–202, doi:10.1016/0012-

821X(94)00249-X.

Brunner, G.W., 2021, HEC-RAS River Analysis System, 2D Modeling User's Manual Version 6.0: USACE, 1–251 p.

Calvesbert, R.J., 1970, Climate of Puerto Rico and the U.S. Virgin Islands: Department of Commerce, Climatography of the States, v. 60, p. 29.

Chaplin, J.J., 2005, Deelopment of regional curves relating bankfull-channel geometry and discharge to drainage area for streams in Pennsylvania and selected areas of Maryland: U.S. Geological Survey Scientific Investigations Report 2005-5147, p. 34.

Corato, G., Moramarco, T., and Tucciarelli, T., 2011, Discharge estimation combining flow routing and occasional measurements of velocity: Hydrology and Earth System Sciences, v. 15, p. 2979–2994, doi:10.5194/HESS-15-2979-2011.

DeLong, S.B., Pelletier, J.D., and Arnold, L., 2007, Bedrock landscape development modeling: Calibration using field study, geochronology, and digital elevation model analysis: GSA Bulletin, v. 119, p. 157–173, doi:10.1130/B25866.1.

Desormeaux, C., Godard, V., Lague, D., Duclaux, G., Fleury, J., Benedetti, L., Bellier, O., and ASTER Team, 2022, Investigation of stochastic-threshold incision models across a climatic and morphological gradient: Earth Surface Dynamics Discussion, v. 10, p. 473–492, doi:10.5194/esurf-2021-83.

DiBiase, R.A., 2018, Short communication: Increasing vertical attenuation length of cosmogenic nuclide production on steep slopes negates topographic shielding corrections for catchment erosion rates: Earth Surface Dynamics, v. 6, p. 923–931, doi:10.5194/esurf-6-923-2018.

DiBiase, R.A., Rossi, M.W., and Neely, A.B., 2018, Fracture density and grain size controls on the relief structure of bedrock landscapes: Geology, v. 46, p. 399–402, doi:10.1130/G40006.1.

DiBiase, R.A., and Whipple, K.X., 2011, The influence of erosion thresholds and runoff variability on the relationships among topography, climate, and erosion rate: Journal of Geophysical Research: Earth Surface, v. 116, p. 4036, doi:10.1029/2011JF002095.

Duvall, A., Kirby, E., Burbank, D., Duvall, C.:, Kirby, E., and Burbank, D., 2004, Tectonic and lithologic controls on bedrock channel profiles and processes in coastal California: Journal of Geophysical Research: Earth Surface, v. 109, p. 3002, doi:10.1029/2003JF000086.

Eaton, B.C., Mackenzie, L.G., and Booker, W.H., 2020, Channel stability in steep gravel-cobble streams is controlled by the coarse tail of the bed material distribution:, doi:10.1002/esp.4994.

Ehlmann, A., 1968, Clay Mineralogy of Weather Products and of River Sediments, Puerto Rico: Journal of Sedimentary Petrology, v. 38, p. 885–894.

Eidmann, J., and Gallen, S., 2020, Assessing the role of drainage basin characteristics and hydrology on discharge records in Puerto Rico: Geological Society of America Abstracts with Programs, v. 52, doi:10.1130/abs/2020AM-358503.

Ewel, J.J., and Whitmore, J.L., 1973, The ecological life zones of Puerto Rico and the U.S. Virgin Islands: U.S. Department of Agriculture, Forest Service, p. 1–74, https://www.srs.fs.usda.gov/pubs/rp/rp_itf018.pdf.

Finnegan, N.J., Roe, G., Montgomery, D.R., and Hallet, B., 2005, Controls on the channel width of rivers: Implications for modeling fluvial incision of bedrock: Geology, v. 33, p. 229–232, doi:10.1130/G21171.1.

Finnegan, N.J., Sklar, L.S., and Fuller, T.K., 2007, Interplay of sediment supply, river incision, and channel morphology revealed by the transient evolution of an experimental bedrock channel: Journal of Geophysical Research: Earth Surface, v. 112, p. 3–11, doi:10.1029/2006JF000569.

Fisher, G.B., Amos, C.B., Bookhagen, B., Burbank, D.W., and Godard, V., 2012, Channel widths,

landslides, faults, and beyond: The new world order of high-spatial resolution Google Earth imagery in the study of earth surface processes: Special Paper of the Geological Society of America, v. 492, p. 1–22, doi:10.1130/2012.2492(01).

Fisher, G.B., Bookhagen, B., and Amos, C.B., 2013, Channel planform geometry and slopes from freely available high-spatial resolution imagery and DEM fusion: Implications for channel width scalings, erosion proxies, and fluvial signatures in tectonically active landscapes: Geomorphology, v. 194, p. 46–56, doi:10.1016/J.GEOMORPH.2013.04.011.

Flint, J.J., 1974, Stream gradient as a function of order, magnitude, and discharge: Water Resources Research, v. 10, p. 969–973, doi:10.1029/WR010i005p00969.

Gallen, S.F., and Fernandez-Blanco, D., 2021, New Data-driven Bayesian Inversion of Fluvial Topography Clarifies the Tectonic History of the Corinth Rift and Reveals a Channel Steepness Threshold: Journal of Geophysical Research: Earth Surface, v. 126, doi:10.1029/2020JF005651.

Goudie, A.S., 2006, The Schmidt Hammer in geomorphology: Earth Science Review, v. 30, p. 703–718, doi:10.1177/0309133306071954.

Grande, A., Schmidt, A.H., Bierman, P.R., Corbett, L.B., Lopez-Lloreda, C., Willenbring, J., McDowell, W.H., and Caffee, M.W., 2021, Landslides, hurricane,a nd sediment sourcing impact basin-scale erosion estimates in Luquillo, Puerto Rico: Earth and Planetary Science Letters, v. 562, p. 116821.

Granger, D.E., Lifton, N.A., and Willenbring, J.K., 2014, A cosmic trip: 25 years of cosmogenic nuclides in geology: Geological Society of America Bulletin, doi:10.1130/B30774.1.

Holdridge, L.R., 1967, Life zone ecology, *in* Tropical Science Center, San Jose, Costa Rica, p. 206.

Howard, A.D., Dietrich, W.E., and Seidl, M.A., 1994, Modeling fluvial erosion on regional to continental scales: Journal of Geophysical Research, v. 99, p. 13,971-13,986, doi:10/bd8k3j.

Howard, A.D., and Kerby, G., 1983, Channel changes in badlands: Geological Society of America

Bulletin, v. 94, p. 739–752, doi:10.1130/0016-7606(1983)94<739:CCIB>2.0.CO;2.

Kirby, E., and Whipple, K.X., 2012, Expression of active tectonics in erosional landscapes: Journal of Structural Geology, v. 44, p. 54–75.

Knighton, D., 1998, Fluvial Forms and Processes: A New Perspective: , p. 383.

Kohl, C.P., and Nishiizumi, K., 1992, Chemical isolation of quartz for measurement of in-situ-produced cosmogenic nuclides: Geochimica et Cosmochimica Acta, v. 56, p. 3583–3587.

Kondolf, G.M., Piégay, H., and Landon, N., 2002, Channel response to increased and decreased bedload supply from land use change: contrasts between two catchments: Geomorphology, v. 45, p. 35–51, doi:10.1016/S0169-555X(01)00188-X.

Lague, D., 2014, The stream power river incision model: Evidence, theory and beyond: Earth Surface Processes and Landforms, v. 39, p. 38–61, doi:10.1002/esp.3462.

Lague, D., Hovius, N., and Davy, P., 2005, Discharge, discharge variability, and the bedrock channel profile: Journal of Geophysical Research, v. 110, doi:10.1029/2004JF000259.

Lamb, M.P., and Dietrich, W.E., 2009, The persistence of waterfalls in fractured rock: Geological Society of America Bulletin, v. 121, p. 1123–1134.

Larsen, M.C., and Parks, J.E., 1997, How wide is a road? The association of roads and mass-wasting in a forested montane environment: Earth Surface Processes and Landforms, v. 22, p. 835–848, doi:10.1002/(SICI)1096-9837(199709)22:9<835::AID-ESP782>3.0.CO;2-C.

Larsen, M.C., and Santiago-Roman, A., 2001, Mass Wasting and Sediment Storage in a Small Montane Watershed: An Extreme Case of Anthropogenic Disturbance in the Humid Tropics: Geomorphic Processes and Riverine Habitat, v. 4, p. 119–138.

Lavé, J., and Avouac, J.P., 2001, Fluvial incision and tectonic uplift across the Himalayas of central

Nepal: Journal of Geophysical Research: Solid Earth, v. 106, p. 26561–26591, doi:10.1029/2001JB000359.

Leopold, L., and Maddock, T., 1953, The hydraulic geometry of stream channels and some physiographic implications: U.S. Geologic Survey Professional Paper, v. 252, p. 57.

Lin, P., Pan, M., Allen, G.H., Frasson, R.P., Zeng, Z., Yamazaki, D., and Wood, E.F., 2020, Global Estimates of Reach-Level Bankfull River Width Leveraging Big Data Geospatial Analysis: Geophysical Research Letters, v. 47, p. e2019GL086405, doi:10.1029/2019GL086405.

Lopes, L.C.F.L., Bacellar, L.A.P., and Castro, P.T.A., 2016, Assessment of the debris-flow susceptibility in tropical mountains using clast distribution patterns: Geomorphology, v. 275, p. 16–25, doi:10.1016/j.geomorph.2016.09.026.

McKean, J., Isaak, D., and Wright, W., 2011, Improving Stream Studies With a Small-Footprint Green Lidar: Eos, v. 90, p. 341–342.

Merritt, W.S., Letcher, R.A., and Jakeman, A.J., 2003, A review of erosion and sediment transport models: Environmental Modelling and Software, v. 18, p. 761–799.

Molnar, P., Anderson, R.S., and Anderson, S.P., 2007, Tectonics, fracturing of rock, and erosion: Journal of Geophysical Research, v. 112, doi:10.1029/2005JF000433.

Montgomery, D.R., and Gran, K.B., 2001, Downstream variations in the width of bedrock channels: Water Resources Research, v. 37, p. 1841–1846, doi:10.1029/2000WR900393.

Moore, A.K., and Granger, D.E., 2019, Watershed-averaged denudation rates from cosmogenic 36Cl in detrital magnetite: Earth and Planetary Science Letters, v. 527, p. 1–10, doi:10.1016/j.epsl.2019.115761.

Moussa, M.T., Seiglie, G.A., Meyerhoff, A.A., and Taner, I., 1987, The Quebradillas Limestone (Miocene-Pliocene), northern Puerto Rico, and tectonics of the northeastern Caribbean margin:

Geological Society of America Bulletin, v. 99, p. 427–439.

Murphy, S.F., Stallard, R.F., Scholl, M.A., González, G., and Torres-Sánchez, A.J., 2017, Reassessing rainfall in the Luquillo Mountains, Puerto Rico: local and global ecohydrological implications: PLOS ONE, v. 12, p. 1–26, doi:10.1371/journal.pone.0180987.

Nativ, R., Turowski, J.M., Goren, L., Laronne, J.B., Bruce, J., and Shyu, H., 2022, Influence of Boulders on Channel Width and Slope: Theory and Field Application: Journal of Geophysical Research: Earth Surface, doi:10.1029/2021JF006537.

Neal, J.C., Odoni, N.A., Trigg, M.A., Freer, J.E., Garcia-Pintado, J., Mason, D.C., Wood, M., and Bates, P.D., 2015, Efficient incorporation of channel cross-section geometry uncertainty into regional and global scale flood inundation models: Journal of Hydrology, v. 529, p. 169–183.

Neely, A.B., and DiBiase, R.A., 2020, Drainage Area, Bedrock Fracture Spacing, and Weathering Controls on Landscape-Scale Patterns in Surface Sediment Grain Size: Journal of Geophysical Research: Earth Surface, v. 125, doi:10.1029/2020JF005560.

Nelson, P.A., Brew, A.K., and Morgan, J.A., 2015, Morphodynamic response of a variable-width channel to changes in sediment supply: Water Resources Research, v. 51, p. 5717–5734, doi:10.1002/2014WR016806.

Niedzielski, T., Migon, P., and Palacek, A., 2009, A minimum sample size required from Schmidt hammer measurements: Earth Surface Processes and Landforms, v. 34, p. 1713–1725.

Nishiizumi, K., Imamura, M., and Caffee, M.W., 2007, Absolute calibration of 10Be AMS standards: Nuclear Instruments and Methods in Physics Research Section B: Beam Interactions with Materials and Atoms, v. 258, p. 403–413, doi:10.1016/j.nimb.2007.01.297.

NOAA, 2011, Mean Annual Rainfall 1981-2010, Puerto Rico:

OCM Partners, 2022, 2018 USGS Lidar DEM: Post Hurricane Maria - Puerto Rico:,

https://www.fisheries.noaa.gov/inport/item/60105.

Ouimet, W.B., Whipple, K.X., and Granger, D.E., 2009, Beyond threshold hillslopes: Channel adjustment to base-level fall in tectonically active mountain ranges: Geology, v. 37, p. 579–582, doi:10.1130/g30014a.1.

Pederson, J.L., and Tressler, C., 2012, Colorado River long-profile metrics, knickzones and their meaning: Earth and Planetary Science Letters, v. 345, p. 171–179.

Perron, J.T., and Royden, L., 2012, An integral approach to bedrock river profile analysis: Earth Surface Processes and Landforms, v. 38, p. 570–576, doi:10.1002/ESP.3302.

Perumal, M., Moramarco, T., Sahoo, B., and Barbetta, S., 2007, A methodology for discharge estimation and rating curve development at ungauged river sites: Water Resources Research, v. 43, p. 2412, doi:10.1029/2005WR004609.

Pfeiffer, A.M., Finnegan, N.J., and Willenbring, J.K., 2017, Sediment supply controls equilibrium channel geometry in gravel rivers: Proceedings of the National Academy of Science, v. 114.

Phillips, C.B., and Jerolmack, D.J., 2016, Self-organization of river channels as a critical filter on climate signals: Science, v. 352, p. 694–697, doi:10.1126/SCIENCE.AAD3348/SUPPL_FILE/AAD3348-PHILLIPS-SM.PDF.

Pike, A.S., 2008, Longitudinal patterns in stream channel geomorphology and aquatic habitat in the Luquillo Mountains of Puerto Rico.:

Pike, A.S., Scatena, F.N., and Wohl, E.E., 2010, Lithological and fluvial controls on the geomorphology of tropical montane stream channels in Puerto Rico: Earth Surface Processes and Landforms, v. 35, p. 1402–1417, doi:10.1002/esp.1978.

PRISM Climate Group, 2022, PRISM Climate Data: Oregon State University, prism.oregonstate.edu.

Prosser, I.P., Rustomji, P., Young, B., Moran, C., and Hughes, A., 2001, Constructing river basin sediment budgets for the National Land and Water Resources Audit: CSIRO Land and Water Technical Report, v. 15.

Riebe, C.S., Kirchner, J.W., and Finkel, R.C., 2003, Long-term rates of chemical weathering and physical erosion from cosmogenic nuclides and geochemical mass balance: Geochimica et Cosmochimica Acta, v. 67, p. 4411–4427.

Rossi, M.W., Whipple, K.X., and Vivoni, E.R., 2016, Precipitation and evapotranspiration controls on daily runoff variability in the contiguous United States and Puerto Rico: Journal of Geophysical Research: Earth Surface, v. 121, p. 128–145, doi:10.1002/2015JF003446.Received.

Safran, E.B., Bierman, P.R., Aalto, R., Dunne, T., Whipple, K.X., and Caffee, M., 2005, Erosion rates driven by channel network incision in the Bolivian Andes: Earth Surface Processes and Landforms, v. 30, p. 1007–1024, doi:10.1002/esp.1259.

Schaefer, J.M., Codilean, A.T., Willenbring, J.K., Lu, Z.T., Keisling, B., Fuloep, R.H., and Val, P., 2022, Cosmogenic nuclide techniques: Nature Reviews Methods Primers, v. 2, p. 1–22.

Schellekens, J.H., 1998, Geochemical evolution and tectonic history of Puerto Rico: Geological Society of America Special Paper 322,.

Schwanghart, W., and Scherler, D., 2014, Short Communication: Topo-Toolbox 2--MATLAB-based software for topographic analysis and modeling in Earth surface sciences: Earth Surface Dynamics, v. 2, p. 1–7, doi:10.5194/esurf-2-1-2014.

Scott, D.N., and Wohl, E.E., 2019, Bedrock fracture influences on geomorphic process and form across process domains and scales: Earth Surface Processes and Landforms, v. 44, p. 27–45, doi:10.1002/ESP.4473.

Sharma, P., Kubik, P.W., Fehn, U., Gove, H.E., Nishiizumi, K., and Elmore, D., 1990, Development of

36Cl standards for AMS: Nuclear Instruments and Methods in Physics Research Section B: Beam Interactions with Materials and Atoms, v. 52, p. 410–415, doi:10.1016/1068-583X(90)90447-3.

Simon, A., Larsen, M.C., and Hupp, C.R., 1990, The role of soil processes in determining mechanisms of slope failure and hillslope development in a humid-tropical forest eastern Puerto Rico: Geomorphology, v. 3, p. 263–286, doi:10.1016/0169-555X(90)90007-D.

Sklar, L.S., and Dietrich, W.E., 2004, A mechanistic model for river incision into bedrock by saltating bed load: Water Resources Research, v. 40.

Sklar, L.S., Riebe, C.S., Marshall, J.A., Genetti, J., Leclere, S., Lukens, C.L., and Merces, V., 2017, The problem of predicting the size distribution of sediment supplied by hillslopes to rivers: Geomorphology, v. 277, p. 31–49, doi:10.1016/j.geomorph.2016.05.005.

Spotila, J.A., Moskey, K.A., and Prince, P.S., 2015, Geologic controls on bedrock channel width in large, slowly-eroding catchments: Case study of the New River in eastern North America: Geomorphology, v. 230, p. 51–63, doi:10.1016/j.geomorph.2014.11.004.

Stoker, J., 2022, Assessing 3D Elevation Program Data- DYK?

Stone, J.O., 2000, Air pressure and cosmogenic isotope production: Journal of Geophysical Research, v. 105, p. 23753–23759.

Tazioli, A., 2011, Experimental methods for river discharge measurements: comparison among tracers and current meter: Hydrological Sciences Journal, v. 56, p. 1314–1324, doi:10.1080/02626667.2011.607822.

The Southeast Regional Climate Center, 2019, Historical Climate Summaries for Puerto Rico and the U.S. Virgin Islands:, https://sercc.com/climateinfo/historical/historical_pr.html (accessed April 2022).

Tomkin, J.D., Brandon, M.T., Pazzaglia, F.J., Barbour, J.R., and Willett, S.D., 2003, Quantitative testing

of bedrock incision models for the Clearwater River, NW Washington state: Journal of Geophysical Research, v. 108, p. 2308, doi:10.1029/2001JB000862.

Turowski, J.M., 2018, Alluvial cover controlling the width, slope and sinuosity of bedrock channels: Earth Surface Dynamics, v. 6, p. 29–48, doi:10.5194/ESURF-6-29-2018.

Turowski, J.M., 2021, Upscaling sediment-flux-dependent fluvial bedrock incision to long timescales: Journal of Geophysical Research: Earth Surface, v. 126, doi:e2020JF005880.

Turowski, J.M., and Hodge, R., 2017, A probabilistic framework for the cover effect in bedrock erosion: Earth Surface Dynamics, v. 5, p. 311–330, doi:10.5194/ESURF-5-311-2017.

Turowski, J.M., Hovius, N., Wilson, A., and Horng, M.J., 2008, Hydraulic geometry, river sediment and the definition of bedrock channels: Geomorphology, v. 99, p. 26–38, doi:10.1016/j.geomorph.2007.10.001.

Turowski, J.M., Lague, D., and Hovius, N., 2009, Response of bedrock channel width to tectonic forcing: Insights from a numerical model, theoretical considerations, and comparison with field data: Journal of Geophysical Research: Earth Surface2, v. 114, doi:10.1029/2008JF001133.

Turowski, J.M., Wyss, C.R., and Beer, A.R., 2015, Grain size effects on energy delivery to the streambed and links to bedrock erosion: Geophysical Research Letters, v. 42, p. 1775–1780, doi:10.1002/2015GL063159.

U.S. Geological Survey, 1998, Geology, Geochemistry, Geophysics, Mineral Ocurrences and Mineral Resource Assessment for the Commonwealth of Puerto Rico:, doi:10.3133/ofr9838.

U.S. Geological Survey, 1960, USGS 1:20000-scale Quadrangle for Adjuntas, P.R.:

U.S. Geological Survey, 2016, USGS National Watershed Boundary Dataset (WBD) Downloadable Data Collection - National Geospatial Data Asset (NGDA) Watershed Boundary Dataset (WBD):, http://datagateway.nrcs.usda.gov (accessed January 2022).

USACE, 2016, HEC-RAS river analysis system, Hydraulic reference manual v 5.0:

Volckmann, R.P., 1984, Geologic map of the San German quadrangle, southwest Puerto Rico, *in* U.S. Geological Survey Miscellaneous Investigations Series Map I-1558,.

Walsh, L.S., Martin, A.J., Ojha, T.P., and Fedenczuk, T., 2012, Correlations of fluvial knickzones with landslide dams, lithologic contacts, and faults in the southwestern Annapurna Range, central Nepalese Himalaya: Journal of Geophysical Research: Earth Surface, v. 117, p. 1012, doi:10.1029/2011JF001984.

Whipple, K.X., 2004, Bedrock rivers and the geomorphology of active orogens: Annual Review of Earth and Planetary Sciences, v. 32, p. 151–185, doi:10.1146/annurev.earth.32.101802.120356.

Whipple, K.X., DiBiase, R.A., and Crosby, B.T., 2013, Bedrock Rivers, *in* Treatise on Geomorphology, Elsevier, p. 550–573, doi:10.1016/B978-0-12-374739-6.00254-2.

Whipple, K.X., DiBiase, R.A., Crosby, B.T., and Johnson, J.P.L., 2022, Bedrock Rivers, *in* Treatise on Geomorphology, Elsevier, p. 865–903, doi:10.1016/B978-0-12-818234-5.00101-2.

Whipple, K.X., Hancock, G.S., and Anderson, R.S., 2000, River incision into bedrock: Mechanics and relative efficacy of plucking, abrasion, and cavitation: Geological Society of America Bulletin, v. 112, p. 490–503, doi:10.1130/0016-7606(2000)112<490:RIIBMA>2.0.CO;2.

Whipple, K.X., and Tucker, G.E., 1999, Dynamics of the stream-power river incision model: Implications for height limits of mountain ranges, landscape response timescales, and research needs: Journal of Geophysical Research: Solid Earth, v. 104, p. 17661–17674, doi:10.1029/1999jb900120.

Whittaker, A.C., Cowie, P.A., Attal, M., Tucker, G.E., and Roberts, G.P., 2007, Bedrock channel adjustment to tectonic forcing: Implications for predicting river incision rates: Geology, v. 35, p. 103–106, doi:10.1130/G23106A.1.

Willett, S.D., 1999, Orogeny and orography: The effects of erosion on the structure of mountain belts:

Journal of Geophysical Research: Solid Earth, v. 104, p. 28957–28981, doi:10.1029/1999JB900248.

Wobus, C., Whipple, K.X., Kirby, E., Snyder, N., Johnson, J., Spyropolou, K., Crosby, B., and Sheehan, D., 2006, Tectonics from topography: procedures, promise, and pitfalls, *in* Willett, S., Hovius, N., Brandon, M., and Fisher, D. eds., Tectonics, Climate, and Landscape Evolution, Boulder, Geological Society of America Special Paper, v. 398, p. 55–74.

Wohl, E.E., and David, G.C.L., 2008, Consistency of scaling relations among bedrock and alluvial channels: Journal of Geophysical Research, v. 113, doi:10.1029/2008JF000989.

Wohl, E.E., and Ikeda, H., 1998, Patterns of Bedrock Channel Erosion on the Boso Peninsula, Japan: The Journal of Geology, v. 106, p. 331–346, doi:10.1086/516026.

Wohl, E., Kuzma, J.N., and Brown, N.E., 2004, Reach-scale channel geometry of a mountain river: Earth Surface Processes and Landforms, v. 29, p. 969–981, doi:10.1002/esp.1078.

Wohl, E., and Merritt, D., 2005, Prediction of mountain stream morphology: Water Resources Research, v. 41, p. 1–10, doi:10.1029/2004WR003779.

Yamazaki, D., Ikeshima, D., Sosa, J., Bates, P.D., Allen, G.H., and Pavelsky, T.M., 2019, MERIT Hydro: A High-Resolution Global Hydrography Map Based on Latest Topography Dataset: Water Resources Research, v. 55, p. 5053–5073, doi:10.1029/2019WR024873.

Yang, R., Willett, S.D., and Goren, L., 2015, In situ low-relief landscape formation as a result of river network disruption: Nature, v. 520, p. 526–529.

Yanites, B.J., 2018, The Dynamics of Channel Slope, Width, and Sediment in Actively Eroding Bedrock River Systems: Journal of Geophysical Research: Earth Surface, v. 123, p. 1504–1527, doi:10.1029/2017JF004405.

Yanites, B.J., and Tucker, G.E., 2010, Controls and limits on bedrock channel geometry: Journal of Geophysical Research: Earth Surface, v. 115, p. 4019, doi:10.1029/2009JF001601.

Zondervan, J.R., Whittaker, A.C., Bell, R.E., Watkins, S.E., Brooke, S.A.S., and Hann, M.G., 2020, New constraints on bedrock erodibility and landscape response times upstream of an active fault: Geomorphology, v. 351, p. 106937, doi:10.1016/J.GEOMORPH.2019.106937.

APPENDICES

APPENDIX A: SUPPLEMENTARY FIGURES, TABLES, AND USER MANUAL TO CHAPTER 2

User Manual: The user manual, and all relevant files associated with it, can be found at the following link: https://drive.google.com/drive/folders/1Z5W-n2irvWqYGoc_cH8ZXB2_DMHegzFl?usp=sharing

Currently, all files are located in a private Google Drive link. The files will be moved to a publicly-available repository once the manuscript has undergone peer review and has been approved for publication.

Please refer to the *User_Manual_Document.docx* to walk through each step of the method. The manual is designed to support the user while they run through the Matlab and HEC-RAS programs. All necessary files to run through the sample are included in the User Manual folder. In addition, the user needs to have Matlab, the Matlab spatial analyst package, and HEC-RAS installed.

Figures:

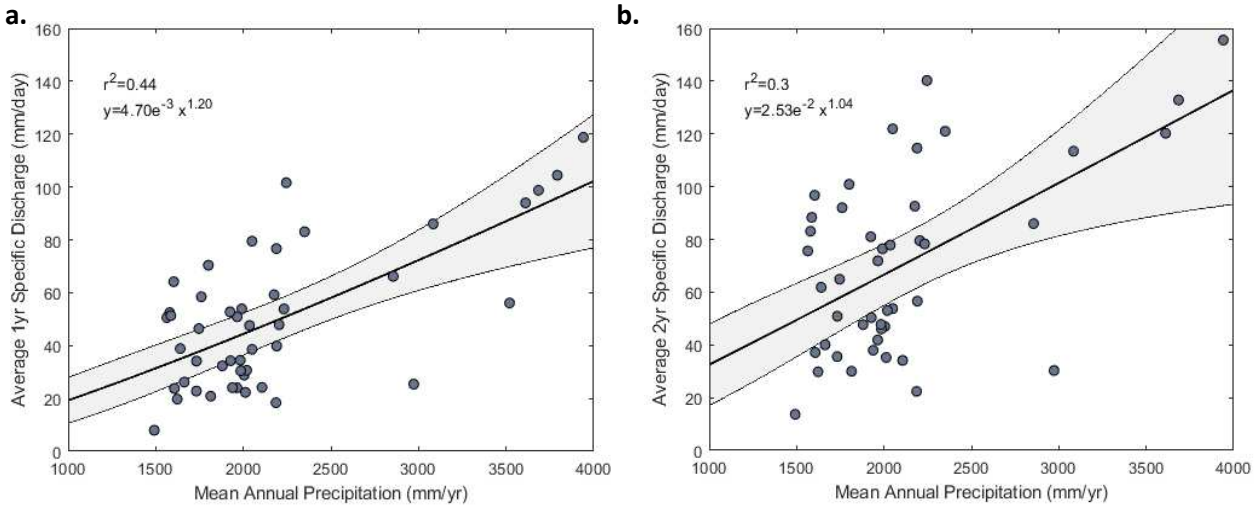

Figure A1. There exists a positive relationship between Mean Annual Precipitation and estimated specific discharge. Here, we present the (a) Mean Annual Precipitation in relation to estimated 1-year RI and (b) 2-year RI discharge values. The relatively low r^2 values of both graphs indicate that the variability of the data is poorly explained by the regression. As a result, we use the Mean Annual Precipitation: Mean Annual Discharge relationship (r^2=0.82) to estimate specific discharge at given locations.

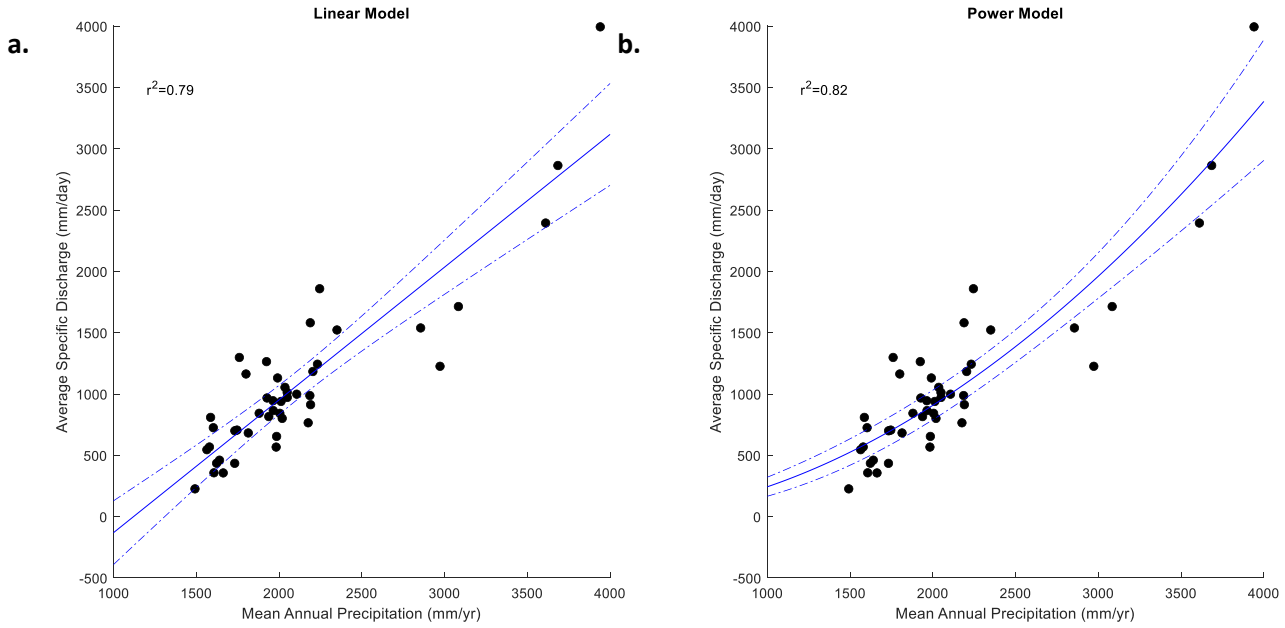

Figure A2. The Mean Annual Specific Discharge is compared to the Mean Annual Precipitation. Above, we compare (a) the fit of a linear regression versus (b) a power regression. For this analysis, we chose to use the power regression, as this model had a better fit (r2=0.82), and estimated specific discharge values at the low end of the Mean Annual Precipitation range were not predicted to be negative.

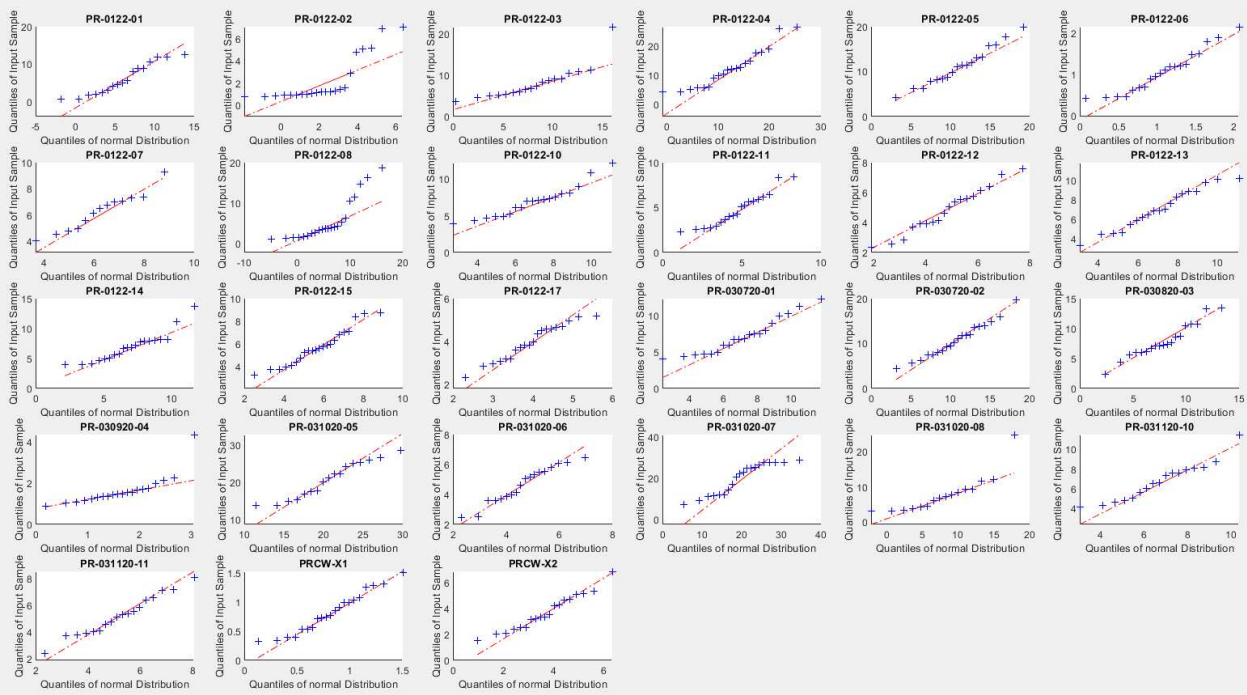

Figure A3. Q-Q plots of the modeled channel width at the various field sampling locations (blue dots in Figure 2.1c). These plots indicate that the data at most field locations follow a normal distribution.

Tables:

Table A1. A summary of the USGS gauging stations that were analyzed. The table includes the USGS gauging station ID, its location, the length of the gauging data record, as well as the calculated drainage area, mean annual discharge, and the estimated Mean Annual Precipitation.

Station ID	Longitude	Latitude	Years of Record	Drainage Area (km^2)	Mean Annual Discharge (m^3/s)	Mean Annual Precipitation (mm/year)
50020500	-66.7363	18.1797	10	48.2	1.5	2050
50021700	-66.7219	18.2422	17	93.2	3.3	1991
50024950	-66.7037	18.3001	18	185.7	5.6	1964
50025155	-66.5628	18.2108	27	23.0	0.9	2204
50025850	-66.6456	18.2139	7	17.9	0.6	2036
50026025	-66.6367	18.2294	20	98.4	2.6	2005
50027000	-66.6206	18.3241	16	81.6	2.6	1912
50028000	-66.7826	18.2987	57	46.6	1.5	2107
50034000	-66.4544	18.2340	41	43.3	1.1	2019
50035000	-66.4596	18.3224	64	347.1	7.2	1985
50043800	-66.2242	18.2202	28	303.0	5.2	1564
50044810	-66.2282	18.2994	16	20.9	0.6	1880
50047535	-66.1216	18.1672	23	1.1	0.0	1603
50047850	-66.1391	18.3323	35	108.3	1.2	1663
50050900	-65.9882	18.1180	26	15.5	0.9	2245
50051310	-65.9563	18.1519	39	26.2	1.3	2350
50051800	-65.9611	18.1837	26	106.4	3.1	2191
50053025	-66.0396	18.1602	27	18.5	0.7	1865
50055000	-66.0092	18.2407	58	232.6	6.4	1965
50055225	-66.0272	18.2467	26	429.9	1.0	1584
50055380	-66.0439	18.2563	14	12.3	0.3	1586
50055750	-65.8849	18.2322	27	57.8	1.2	2561
50056400	-65.9258	18.2141	45	42.5	1.4	2049
50057000	-65.9677	18.2565	57	155.9	3.8	2176
50059210	-65.9901	18.3485	5	33.4	0.6	1983
50061800	-65.8885	18.3165	49	26.4	0.8	3520
50063800	-65.8136	18.3579	50	22.3	1.7	3611
50064200	-65.8416	18.3434	40	18.9	1.2	3792
50065500	-65.7504	18.3268	39	17.8	1.6	3685
50067000	-65.7306	18.3290	37	10.3	0.6	3084
50070900	-65.7007	18.2808	13	28.5	1.1	2973
50071000	-65.6934	18.2970	55	38.6	1.9	2856
50075000	-65.7854	18.2752	45	3.3	0.4	3941
50081000	-65.8690	18.1721	33	17.2	0.7	2232
50090500	-65.9396	18.0252	37	13.9	0.6	1924
50092000	-66.0321	18.0322	51	47.4	1.7	1800

50093000	-66.0093	18.0358	15	10.6	0.4	1760
50093120	-66.0232	18.0144	11	66.5	1.5	1746
50106100	-66.3544	18.0815	29	112.7	0.8	1492
50110900	-66.4574	18.1245	27	36.8	0.5	1732
50112500	-66.5627	18.0845	51	25.1	0.5	1814
50113800	-66.6045	18.1148	27	30.8	0.9	1927
50114900	-66.6425	18.0979	19	18.8	0.5	1938
50124200	-66.7978	18.0423	32	49.0	0.7	1623
50126150	-66.8415	18.0472	22	83.1	0.7	1667
50136400	-67.0854	18.1581	31	47.4	1.5	2190
50138000	-67.1484	18.1407	44	310.8	5.6	1605
50144000	-67.0506	18.2822	53	347.1	10.3	2012
50147800	-67.0922	18.3597	49	184.4	8.4	2190

APPENDIX B: SUPPLEMENTARY FIGURES, TABLES, AND USER MANUAL TO CHAPTER 3

Supplemental Data: The raw data used for this analysis will be temporarily available via Google Drive:

https://docs.google.com/spreadsheets/d/1tfqILHEVVhTUWPR39XZvRNUR9z-afIPa/edit?usp=sharing&ouid=114783226087131503142&rtpof=true&sd=true

Data will be moved to a data repository upon publication.

Figures:

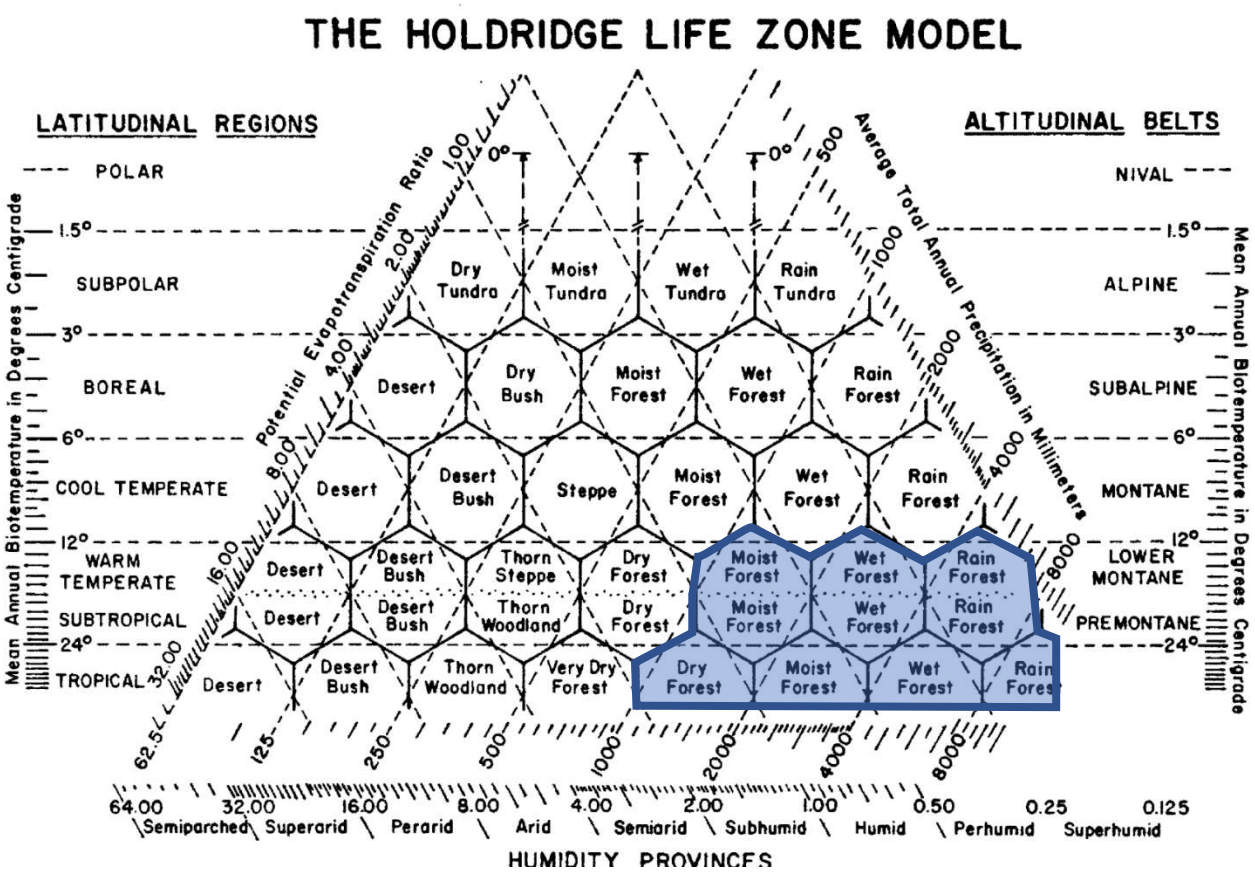

Figure B1. A diagram (from Ewel and Whitmore, 1973) of the of the Holdridge Ecological Life Zone (e.g. Ecozone) classification (Holdridge, 1967), according to changes in humidity, altitude, precipitation, and the potential evapotranspiration ratio. The Ecozones found in Puerto Rico (highlighted in blue) are generally located at low to lower montane elevations, medium to high precipitation and subhumid to superhumid conditions.

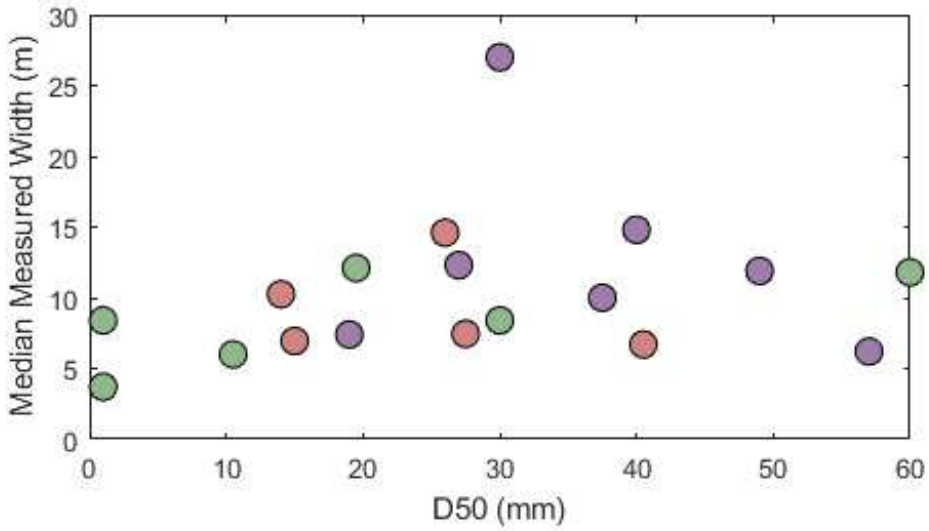

Figure B2. A plot of the measured median grain size diameter (D50) in relation to the median measured channel width. Colors indicate a lack of a discernable trend between the median grain size diameter and the lithologic unit that is being eroded.

Tables:

Table B.1. A table of the field sample locations, the bedrock found at each location, as well as the measurement types that were performed at each location.

Location ID	Lat	Long	Measurement Type			Rock Type
PR-0122-01	18.10375	-65.8825	--	Grain Size	Width	Granodiorite
PR-0122-02	18.09285	-65.8965	Schmidt Hammer	Grain Size	Width	Granodiorite
PR-0122-03	18.08908	-65.902	Schmidt Hammer	Grain Size	Width	Granodiorite
PR-0122-04	18.09042	-65.9119	Schmidt Hammer	Grain Size	Width	Granodiorite
PR-0122-07	18.25329	-66.7317	Schmidt Hammer	Grain Size	Width	Granodiorite
PR-0122-08	18.25763	-66.7587	--	Grain Size	Width	Granodiorite
PR-030720-01	18.21661	-66.6427	Schmidt Hammer	Grain Size	--	Granodiorite
PR-030720-02	18.19737	-66.65	Schmidt Hammer	Grain Size	--	Granodiorite
PR-031020-05A	18.21529	-66.6045	--	Grain Size	--	Granodiorite
PR-0310200-5B	18.21529	-66.6045	--	Grain Size	--	Granodiorite
PR-031020-06	18.20886	-66.6143	--	Grain Size	--	Granodiorite
PR-033120-07	18.22443	-66.6422	Schmidt Hammer	Grain Size	--	Granodiorite
PR-0122-14	18.11628	-66.9358	Schmidt Hammer	Grain Size	Width	Serpentinite
PR-0122-15	18.1045	-66.9781	Schmidt Hammer	Grain Size	Width	Serpentinite
PR-0122-16	18.10341	-66.9704	Schmidt Hammer	Grain Size	Width	Serpentinite
PR-0122-17	18.11019	-66.9863	Schmidt Hammer	Grain Size	Width	Serpentinite
PR-0122-18	18.1365	-67.0076	Schmidt Hammer	Grain Size	Width	Serpentinite
PR-0122-05	18.11374	-66.6042	Schmidt Hammer	Grain Size	Width	Volcaniclastic
PR-0122-06	18.1853	-66.7357	Schmidt Hammer	Grain Size	Width	Volcaniclastic
PR-0122-09	18.10198	-66.5698	Schmidt Hammer	Grain Size	Width	Volcaniclastic
PR-0122-10	18.11827	-66.5716	Schmidt Hammer	Grain Size	Width	Volcaniclastic
PR-0122-11	18.13455	-66.5779	Schmidt Hammer	Grain Size	Width	Volcaniclastic
PR-0122-12	18.13633	-66.5822	--	Grain Size	Width	Volcaniclastic
PR-0122-13	18.09925	-66.5433	--	Grain Size	Width	Volcaniclastic
PR-030820-03	18.20218	-66.5573	Schmidt Hammer	Grain Size	--	Volcaniclastic
PR-030920-04	18.23262	-66.6217	Schmidt Hammer	Grain Size	--	Volcaniclastic
PR-031020-08	18.20146	-66.5802	Schmidt Hammer	Grain Size	--	Volcaniclastic
PR-031020-09	18.21082	-66.5628	Schmidt Hammer	Grain Size	--	Volcaniclastic
PR-031120-10	18.18937	-66.5569	Schmidt Hammer	Grain Size	--	Volcaniclastic
PR-031220-11	18.20124	-66.6236	--	Grain Size	--	Volcaniclastic

Table B2. A comparison of the average and median annual precipitation across the different Ecozones identified in Puerto Rico.

Ecozone	Precipitation Average (mm/yr)	Precipitation Median (mm/yr)
Dry Forest	1,664	1,655
Moist Forest	1,981	1,909
Subtropical Wet Forest	2,156	2,074
Lower Montane Wet Forest	3,136	2,392
Rain Forest	3,902	3,926

APPENDIX C: AN EVALUATION OF UNCERTAINTIES

Intrinsic to any field observation and modeling are uncertainties in the analyses. Below, I cover some uncertainties and possible sources of error that are inherent to this research.

Chapters 2 and 3: Collecting Field Data and Modeling Channel Width

- Accuracy of field measurements of channel width due to the use of a laser range finder, rather than a measuring tape.
- Difference of field measurements of channel width based on personnel, and the 'biotic bankfull' indices that they use to determine channel width.
- Limitations to DEM accuracy and the resulting modeled channel width due to the limit of resolution in the LiDAR, as well as the uncertainties of LiDAR measurements.
- Error associated with estimating discharge based on precipitation. Error may stem from inaccuracies in precipitation estimates (based on PRISM model inaccuracies or limitations of precipitation resolution), or can also stem from an imperfect fit between precipitation and discharge.
- In this analysis, a Manning's n value of 0.05 was assumed for all models. However, results may have differed through the assignment of a different Manning's n value. In addition, determining Manning's n is an inherently ambiguous process, and relies on the analyst to determine its value based on fitting the channel characteristics to a given picture. The Manning's n value may therefore be different across different locations in Puerto Rico, and may also be different based on the analyst conducting the modeling process.
- Measured channel width error by USGS personnel for the gauging station data. Channel width measurements by USGS personnel were also spread out in both space and time. Measurements can therefore vary based on personnel and the equipment used to make the measurements. In

addition, some measurements further away from the gauging station may not be the best representation of channel width at the actual gauging station.

- As discussed in the chapter, there may be greater uncertainty when modeling larger streams, as the LiDAR does not penetrate through water. As a result, the routed flow may be inaccurate—especially at larger rivers where the 'bottom of the stream' in the HEC-RAS model is actually the top of the water surface at the time of LiDAR collection.
- Channel width was only obtained in HEC-RAS at the delineated cross section locations. Width measurements at the cross sections were characterized through an average or median value. This resulting value, however, may not be the best representation of channel width at the location of interest.

Chapter 4:

- With cosmogenic nuclides, it is assumed that the sand in the river is well-mixed, and represents the average of the denudation rate of the area upstream. However, sediment can be variable based on rock density and grain size. With this in mind, the sediment we collected may be biased towards the erosion rate of a particular area of the upstream watershed or rock type.
- For samples analyzed for beryllium, the uncertainties of cosmogenic nuclide concentrations may be modulated based on the quantity of quartz and beryllium in the sample. If there is more material/quartz sand, we have a larger sample to work with. In addition, the higher the beryllium concentration, the lower the sensitivity and error of the measurements and results.
- Inherent instrument measuring error of the accelerated mass spectrometer that measures the concentration of cosmogenic nuclides. In addition, to derive denudation rates from this concentration, we assume a density of the rock/sediment. This density, however, was never measured for my particular samples and may have been inaccurate.
- Care was used to prepare the samples in the laboratory for cosmogenic nuclide analysis. However, during this process, solution was often either decanted or transferred. With this in

mind, analytical results can vary in concentration and/or accuracy if sample is accidentally lost during these processes.

- In this section we compare modeled incision rates to the measured denudation rates. These two measurements are inherently different, and do not necessarily equal one another. As a result, it may be inaccurate to assume that incision rates and denudation rates are equivalent.
- As discussed in Chapter 4, there are likely many other factors that affect incision rates. As a result, modeled results may be improved through including more variables that influence incision rates.